

Abstract

DALMAU, RAFAEL FEDERICO. Aluminum Nitride Bulk Crystal Growth in a Resistively Heated Reactor. (Under the direction of Prof. Zlatko Sitar).

A resistively heated reactor capable of temperatures in excess of 2300°C was used to grow aluminum nitride (AlN) bulk single crystals from an AlN powder source by physical vapor transport (PVT) in nitrogen atmosphere. AlN crystals were grown at elevated temperatures by two different methods. Self-seeded crystals were obtained by spontaneous nucleation on the crucible walls, while seeded growth was performed on singular and vicinal (0001) surfaces of silicon carbide (SiC) seeds.

During self-seeded growth experiments a variety of crucible materials, such as boron nitride, tungsten, tantalum, rhenium, tantalum nitride, and tantalum carbide, were evaluated. These studies showed that the morphology of crystals grown by spontaneous nucleation strongly depends on the growth temperature and contamination in the reactor. Crucible selection had a profound effect on contamination in the crystal growth environment, influencing nucleation, coalescence, and crystal morphology. In terms of high-temperature stability and compatibility with the growth process, the best results for AlN crystal growth were obtained in crucibles made of sintered tantalum carbide or tantalum nitride. In addition, contamination from the commercially purchased AlN powder source was reduced by pre-sintering the powder prior to growth, which resulted in a drastic reduction of nearly all impurities. Spontaneously grown single crystals up to 15 mm in size were characterized by x-ray diffraction, x-ray topography, glow discharge mass spectrometry, and secondary ion mass

spectrometry. Average dislocation densities were on the order of 10^3 cm^{-3} , with extended areas virtually free of dislocations. High resolution rocking curves routinely showed peak widths as narrow as 7 arcsec, indicating a high degree of crystalline perfection. Low-temperature partially polarized optical reflectance measurements were used to calculate the crystal-field splitting parameter of AlN, $\Delta_{cr} = -230 \text{ meV}$, and a low-temperature (1.7 K) band gap energy of 6.096 eV was obtained for unstrained wurtzite AlN.

Seeded growth of AlN bulk crystals on on-axis and off-axis (0001), Si-face SiC seeds was investigated as a means to scale up maximum single crystal size and pre-define crystal orientation. A two-step deposition process was developed for the growth of thick layers. AlN layers 0.1–3 mm thick were deposited on inch-sized seeds. X-ray diffraction analysis evidenced that the AlN grew in the direction of the seed. A one-dimensional isotropic model was formulated to calculate the thermal stress distribution in AlN/SiC heterostructures. Cracks formed in the AlN layers due to the thermal expansion mismatch between AlN and SiC were observed to decrease with increasing AlN thickness, in agreement with model calculations. Crack-free AlN crystals were obtained from grown layers by evaporating the SiC seed *in situ* during high-temperature PVT growth. Based on these results, a reproducible seeded growth process was developed for production of crack-free AlN crystals having pre-determined polarity and orientation.

**Aluminum Nitride Bulk Crystal Growth in a
Resistively Heated Reactor**

by

RAFAEL FEDERICO DALMAU

A dissertation submitted to the Graduate Faculty of
North Carolina State University
in partial fulfillment of the
requirements for the Degree of
Doctor of Philosophy

MATERIALS SCIENCE AND ENGINEERING

Raleigh
2005

APPROVED BY:



Zlatko Sitar
Chair of Advisory Committee



Raoul Schlessler



Robert Nemanich



Jon-Paul Maria

For Frank, Carol, Angie, Andrea, *abuelo* Frank, Nilda, and Tania

La vida te da sorpresas...

(de una canción de Rubén Blades)

Biography

Rafael Dalmau was born in San Juan, Puerto Rico to Frank and Carolyn Dalmau. He earned the Bachelor of Science degree in physics from the University of Puerto Rico, Río Piedras, where he worked in the Thin Film Physics and X-ray Diffraction Facility under the supervision of Dr. Antonio Martínez. During this time Rafael worked on several thin film deposition processes, including growth of bismuth and antimony heterostructures by physical vapor deposition. He also collaborated in the establishment of the university's first molecular beam epitaxy system.

Further pursuing a lifelong interest in science, Rafael enrolled in the doctoral program of the Materials Science and Engineering Department at North Carolina State University in 2001, where he also worked as a member of the laboratory for research on Wide Bandgap Materials under the supervision of Dr. Zlatko Sitar. There he studied the high-temperature physical vapor transport growth of aluminum nitride bulk crystals for the fabrication of native III-nitride substrates.

Acknowledgements

A project of this nature is never exclusively the work of one person. I acknowledge the contributions and support of my mentors, colleagues, friends, and family. Any errors or omissions contained herein are solely my responsibility.

To the members of my advisory committee, my sincerest gratitude. Your guidance has been critical to my success at the university. Zlatko Sitar, thank you for taking me on as a student and allowing me to participate in such a challenging project. What I have learned under your mentorship cannot be put into words. Raoul Schlessler's assistance was instrumental in the realization of many of these experiments; thank you for many helpful discussions. I thank Jon-Paul Maria for unrestricted access to x-ray diffraction facilities. I had the privilege of participating in Robert Nemanich's classroom for two semesters and being inspired by his dedication to pedagogy. Thank you for helping me achieve a deeper understanding of solid state physics.

I thank the many collaborators from the MURI project for their contributions: Robert Davis, Donald Brenner, Yanxin Li, Balaji Raghothamachar, Michael Dudley, Yuri Makarov, Bei Wu, Hui Zhang, Jaime Freitas, Dae-Woo Kim, Subhash Mahajan, Brian Skromme, and Li Chen.

NC State University has been a challenging and very rewarding place to work and study. There are many people here who have made the last four years a memorable experience. To the members of the WideBandgaps research laboratory, Seiji, Tom, Xianglin, Alex, Elif, Erdem, Will, Dejin, Ziad, Nirmal, Jeremy, Gleb, I wish much success wherever their endeavors take them. Ramón Collazo, *gracias por la amistad y el apoyo*. Vladimir

Noveski was a great *amigo*. Zach Reitmeier, Brian Wagner, and Ji-Soo Park helped with MOCVD work. Brian Rodriguez introduced me to PFM and provided the measurements shown herein. Thanks to Gail Abell, Jan Jackson, and Linda Legnasky for helping keep us all afloat. Special thanks to Edna Deas for... so many things. Much of the experimental work would not have been possible without the input of the campus machine shops. Thank you, Larry Dufour and Hai Bui. I am also grateful to David Shafer, Catherine Morell, and Rebeca Rufty of the Graduate School.

To my family, this dissertation is dedicated to you.

This project was funded by the Office of Naval Research under the auspices of the MURI program; grant no. N00014-01-1-0716, Dr. C. Wood, project monitor. I would also like to acknowledge the financial assistance of the Department of Education under the GAANN Fellowship program.

Table of Contents

List of Tables	x
List of Figures	xi
List of Abbreviations	xvii
1 Introduction	1
<i>1.1 Dissertation overview</i>	<i>1</i>
<i>1.2 Aluminum nitride</i>	<i>2</i>
1.2.1 Overview	2
1.2.2 Historical perspective.....	3
1.2.3 Material properties	5
1.2.4 Applications of aluminum nitride and related alloys.....	14
<i>1.3 Crystal growth</i>	<i>15</i>
1.3.1 Overview	15
1.3.2 Physical vapor transport growth	16
1.3.3 Identification of issues in aluminum nitride bulk crystal growth.....	21
2 Aluminum Nitride Crystal Growth I: Spontaneous Nucleation	24
<i>2.1 Objectives</i>	<i>24</i>
<i>2.2 Reactor design and operation</i>	<i>25</i>
<i>2.3 Experiment</i>	<i>29</i>
2.3.1 Thermodynamics and kinetics of aluminum nitride crystal growth	29
2.3.2 Experimental procedure	33
2.3.3 Characterization techniques.....	34

2.4	<i>Crucibles for aluminum nitride growth</i>	35
2.4.1	Objectives	35
2.4.2	Boron nitride	36
2.4.3	Refractory metals	36
2.4.4	Refractory metal carbides and nitrides	37
2.4.5	Other materials	37
2.5	<i>Results and discussion</i>	39
2.5.1	Growth in boron nitride crucibles	40
2.5.2	Growth in refractory metal and metal carbide or nitride crucibles	47
2.5.3	Elemental analysis	49
2.5.4	Optical characterization	50
2.6	<i>Summary</i>	51
3	Aluminum Nitride Crystal Growth II: Seeded Growth	53
3.1	<i>Objectives</i>	53
3.2	<i>Identification of issues in seeded growth on silicon carbide</i>	53
3.3	<i>On-axis (0001) silicon carbide substrates</i>	55
3.3.1	Experiment	55
3.3.2	Characterization techniques	56
3.3.3	Results and discussion	56
3.4	<i>Off-axis (0001) silicon carbide substrates</i>	64
3.4.1	Experiment	64
3.4.2	Results and discussion	64

3.5	<i>Analysis of stress in aluminum nitride-silicon carbide bilayer structures</i>	68
3.5.1	Objectives	68
3.5.2	Model formulation	68
3.5.3	Results and discussion	73
3.5.4	Summary	76
3.6	<i>Extended defects in aluminum nitride grown on silicon carbide</i>	76
3.6.1	Overview	76
3.6.2	Voids	76
3.6.3	Cracks	77
3.6.4	Inversion domains	79
3.6.5	Summary	83
3.7	<i>Summary</i>	84
4	Conclusions and Possible Future Work	86
4.1	<i>Aluminum nitride crystal growth</i>	86
4.2	<i>Aluminum nitride characterization</i>	88
5	Appendix A: Review of Recent Results of AlN Bulk Crystal Growth	91
5.1	<i>Sublimation growth: technique and process parameters</i>	93
5.2	<i>Materials' requirements for crystal growth</i>	95
5.3	<i>Self-seeded crystal growth</i>	97
5.4	<i>Seeded growth of AlN crystals</i>	101
5.4.1	Growth of AlN on SiC seeds	101
5.4.2	Growth of AlN on AlN seeds	105

5.5	<i>Summary</i>	106
5.6	<i>Acknowledgements</i>	107
5.7	<i>Bibliography</i>	107
5.8	<i>Figures</i>	112
6	Appendix B: Overview of Selected Characterization Techniques	120
6.1	<i>Glow discharge mass spectrometry (GDMS)</i>	120
6.2	<i>Synchrotron white beam x-ray topography (SWBXT) and high resolution x-ray diffraction (HRXRD)</i>	125
6.2.1	SWBXT	125
6.2.2	HRXRD.....	127
6.3	<i>Piezoresponse force microscopy (PFM)</i>	130
7	References	132

List of Tables

Table 1.1. Properties of wurtzite AlN (room temperature values unless otherwise noted). ...	14
Table 1.2 Properties of SiC (room temperature values unless otherwise noted).....	21
Table 2.1. Melting points of selected refractory elements, borides, nitrides, and carbides. ...	39
Table 2.2. GDMS analysis of AlN powder sources and crystals (all values in ppm wt).....	50
Table 3.1 GDMS analysis of AlN source powder and an AlN wafer grown on a SiC seed (all values ppm wt).	63

List of Figures

- Figure 1.1. Schematic drawing of the hexagonal wurtzite conventional unit cell of AlN. 8
- Figure 1.2. Schematic drawing of the AlN primitive unit cell indicating (a) Al-polar and (b) N-polar structures. 9
- Figure 1.3. Schematic diagram of the band structure of wurtzite AlN showing selection rules for optical transitions at the Γ point. The A band exciton binding energy E_x is shown for reference. 12
- Figure 2.1. a) Schematic diagram of the resistively heated AlN growth system. b) Temperature gradients within the reactor hot zone, showing relative temperatures between the crucible bottom (hot) and top (cool). 26
- Figure 2.2. Structural characterization of a spontaneously nucleated AlN crystal. a) Optical photograph showing well-defined growth faces. Transmission x-ray topographs: b) $g = -1100$, $\lambda = 0.75\text{\AA}$, showing inclusions(I), growth sector boundaries (GSB), growth dislocations (D_1) and dislocation loops (D_2), Pendellösung fringes (PF) are observed on the upper and right wedged edges; c) $g = 000-2$, $\lambda = 0.43\text{\AA}$; and d) $g = -12-10$, $\lambda = 0.81\text{\AA}$, in which the growth dislocations are extinguished. 42
- Figure 2.3. HRXRD of the crystal in Fig. 2.2. a) Double crystal (11-20) rocking curve. b) (11-20) RSM showing a TCRC width (7 arcsec) close to the calculated perfect crystal width of 6 arcsec. 43
- Figure 2.4. a) Photograph of an AlN crystal grown by spontaneous nucleation in a BN crucible. The c -direction is in the plane of the crystal, aligned along the growth ridges.

b) Photograph of coalesced AlN crystals grown in a W crucible exhibiting well-faceted surfaces and characteristic orange color. 44

Figure 2.5. Structural characterization of an AlN *c*-plate. a) Optical photograph of an AlN crystal showing well-defined (-12-10) growth faces on the top and bottom. Transmission x-ray topographs: b) $g = 10\text{-}10$, $\lambda = 0.84\text{\AA}$; c) $g = -12\text{-}10$, $\lambda = 0.43\text{\AA}$; showing inclusions (I) and surface scratches (S). 46

Figure 2.6. HRXRD of the crystal in Fig. 2.5. a) Double crystal (0002) rocking curve showing tilt broadening due to crystal bending. b) (0002) RSM showing a narrow TCRC width (8 arcsec). 46

Figure 2.7. Structural characterization of AlN crystals grown in a TaN crucible. a) Optical photograph of AlN single crystals. b) Transmission x-ray topograph of the topmost crystal in (a) showing inclusions (I) and lack of dislocations. c) (11-20) RSM of this crystal, yielding a TCRC width of 9.2 arcsec which is close to the calculated perfect crystal rocking curve width of 6 arcsec. 48

Figure 2.8. a) Optical photograph of an AlN crystal with a flat, naturally occurring *m*-face. b) Low-temperature partially polarized optical reflectance spectra from the *m*-face with (a) the *c* axis parallel to the spectrometer slits and (b) the *c* axis perpendicular to the slits (dotted lines). Solid lines are theoretical fits to spectra. The bottom of the graph is a different finite signal level in each case, to show the features more clearly. 51

Figure 3.1. Optical photographs of holes in an AlN layer (left) and in the corresponding SiC seed (right) due to thermal decomposition along micropipes in the SiC. 57

- Figure 3.2. Schematic illustration of the two-step seeded growth process for production of crack-free AlN bulk crystals. 60
- Figure 3.3. Photographs of a crack-free, polished AlN wafer. Wafer front (left) and back (right) sides are shown; note voids on the back side due to incomplete coalescence at the former substrate interface (mm scale). 61
- Figure 3.4. Photograph of a 2.5 mm thick AlN crystal grown on on-axis 6H-SiC. During high-temperature growth the seed almost completely evaporated. No cracks were observed in the AlN. 62
- Figure 3.5. Structural characterization of an AlN wafer. a) Optical photograph of AlN wafer, 9 x 11 mm, 500 μm thick, prepared from bulk AlN grown on on-axis 6H-SiC (mm grid). Dark spots are from incomplete polishing on the wafer back side. b) Double crystal (0002) rocking curve showing a tilt width of 7.6 arcmin. c) (0002) RSM showing a TCRC width (10.6 arcsec) comparable to the perfect crystal width of 8 arcsec, indicating low impurity incorporation during seeded growth. 63
- Figure 3.6. SEM image of an 800 μm thick AlN layer, grown on 8° off-axis SiC, exhibiting step-flow growth. 65
- Figure 3.7. Structural characterization of AlN grown on 8° off-axis 4H-SiC. a) Optical photograph showing steps on the surface and parallel cracks running along the [1-210] direction. b) Transmission x-ray topograph ($g=1-210$) exhibiting distortion caused by residual strains. c) (0002) RSM showing the tilt (1620 arcsec) and lattice plane spacing difference (1.63%) between the AlN and SiC layers. The TCRC width of AlN is 190 arcsec and the tilt width is ~ 500 arcsec. 67

- Figure 3.8. Schematic diagram of the $N=2$ model structure, consisting of an AlN ($i = 1$) layer grown on a SiC ($i = 2$) substrate. The structure is concave on the AlN film side at room temperature. The beam width W , radius of curvature R , layer thickness t_i , and positive z -direction are indicated. 71
- Figure 3.9. The dependence of the AlN uniaxial tensile stress at the interface of the AlN-SiC layers on a) AlN thickness for a growth temperature of 1875°C , and SiC substrate thickness of $420\mu\text{m}$; and b) on SiC thickness for a growth temperature of 1875°C , and AlN layer thickness of 1 mm. Respective thicknesses corresponding to an assumed cracking strength of 266 MPa are indicated. 75
- Figure 3.10. Etch features observed on AlN {0001} polar surfaces. a) Optical microscopy images of opposite c -faces of a polished AlN crystal grown on on-axis SiC and etched in H_3PO_4 solution. An ID propagates through the entire crystal. b) SEM image of a N-polar ID on an Al-polar surface revealed by etching in KOH solution at 60°C for 10 min. Etched hexagonal hillocks are confined in the Al-polar smooth surface. 80
- Figure 3.11. PFM analysis of AlN (0001) surface. a) Optical microscopy image of a N-polar ID on an Al-polar AlN surface after polishing. b) PFM topography image indicating surface relief (vertical scale: 800 nm). c) PFM error signal (vertical scale: 60 nm). Surface scratches are visible in the polished Al-polar surface (~ 2 nm RMS roughness). d) PFM phase image indicating opposite contrast between N-polar (brighter) and Al-polar regions..... 83
- Figure 5.1. Schematic of the AlN crystal growth process; AlN powder source sublimates and recondenses on a colder seed crystal..... 112

- Figure 5.2. Growth rate as a function of the substrate temperature – comparison of computational results with the published data: ● P=500 Torr, $\delta=4$ mm, $\Delta T=70^\circ\text{C}$, (Balkas *et al.* 1997); ▼ P=1 atm, $\delta=4$ mm, $\Delta T=3.5^\circ\text{C}$ (after Segal *et al.* 2000). 113
- Figure 5.3. a) Picture of a 13.5 mm diameter wafer showing three main single crystal grains (1,2, and 3) and a polycrystalline region (4). b) 10 mm single crystal substrate containing cracked and deformed material around the periphery (after Rojo *et al.* 2001 (c)). 114
- Figure 5.4. (a) Optical photograph of a polished AlN wafer; (b) transmission topograph ($g = -1010$, $\lambda = 0.78 \text{ \AA}$) showing the different defects observed (D_g –growth dislocation, D_s –slip dislocation, S–slip band, C–crack, A–surface artifact/scratch, I–inclusion); (c) optical micrograph showing the same type of defects as topograph; (d) high-resolution triple crystal x-ray diffraction rocking curve, FWHM = 9.7 arcsec (after Raghothamachar *et al.* 2003). 115
- Figure 5.5. AlN single crystal grown by sublimation: grid spacing = 1mm, $T=2260^\circ\text{C}$, $p=400$ Torr, growth duration = 24 hrs, average growth rate in c-direction $>500 \mu\text{m/hr}$ (after Schlessler *et al.* 2002 (b)). 116
- Figure 5.6. (a) Optical photograph of an AlN crystal showing well-defined growth faces. Transmission x-ray topographs: (b) $g = -1100$, $\lambda = 0.75 \text{ \AA}$, showing inclusions (I), growth sector boundaries (GSB), growth dislocations (D_1), and dislocation loops (D_2). Pendellösung fringes (PF) are observed on the upper and right wedged edges; (c) $g = 000-2$, $\lambda = 0.43 \text{ \AA}$; and (d) $g = -12-10$, $\lambda = 0.81 \text{ \AA}$, in which the growth dislocations are extinguished (after Raghothamachar *et al.* 2002). 117

Figure 5.7. Photograph of pure AlN grown for 100 hours. One grid represents 1 mm (after Shi <i>et al.</i> 2001 (b)).....	118
Figure 5.8. Seeded growth by sublimation of AlN. Sequence shows seed (left), and intermediate growth steps after 3, 7, and 34 hrs (after Schlessner <i>et al.</i> 2002 (a)).....	119

List of Abbreviations

BZ	Brillouin zone
DCRC	double crystal rocking curve
EELS	electron energy loss spectroscopy
FWHM	full width at half-maximum
GDMS	glow discharge mass spectrometry
HP	hot pressed
HRXRD	high resolution x-ray diffraction
ICP-OES	inductively coupled plasma optical emission spectroscopy
ID	inversion domain
KOH	potassium hydroxide
MFC	mass flow controller
MOCVD	metal organic chemical vapor deposition
PF	Pendellösung fringes
PFM	piezoresponse force microscopy
PL	photoluminescence
PVT	physical vapor transport
RSF	relative sensitivity factor
RSM	reciprocal space map
SAW	surface acoustic wave
SEM	scanning electron microscope, scanning electron microscopy
SIMS	secondary ion mass spectrometry
SPM	scanning probe microscopy
SSMS	spark source mass spectrometry
SWBXT	synchrotron white beam x-ray topography
TCRC	triple crystal rocking curve

1 Introduction

1.1 Dissertation overview

Wide band gap nitride semiconductors, AlN, GaN, InN, have been identified as promising materials for a broad range of applications in electronics and optoelectronics.¹ Currently, epitaxial heterostructures involving these semiconductors are being grown by different techniques on various substrates.^{2,3,4} Blue light emitting diodes (LEDs) grown on sapphire and silicon carbide (SiC) substrates are commercially available. Blue solid state lasers have been demonstrated⁵ and ultraviolet lasers have been proposed. The two most commonly used substrates, sapphire and SiC, are not closely lattice-matched to the III-nitride overgrown device layers, leading to a high defect density in overgrown active layers, limiting device performance and lifetime. Additional limitations of the currently available substrates include cracking of the device layers due to the large thermal mismatch, and poor thermal conductivity. Thus, the performance of III-nitride semiconductor devices will be greatly improved by the availability of native, thermally and lattice matched substrates. High-quality, single crystalline aluminum nitride (AlN) or gallium nitride (GaN) substrates with low dislocation densities are expected to decrease defect density in the overgrown device structures by several orders of magnitude and, thereby, greatly improve the performance and lifetime of III-nitride devices.

In this dissertation, the high-temperature growth of AlN bulk crystals by physical vapor transport (PVT) was studied using a resistively heated reactor. The present chapter will provide the reader with a historical perspective of AlN crystal growth, introduce the material properties of AlN, and discuss applications of AlN and the III-nitrides. Also, a discussion of

crystal growth from the vapor will be presented. The second chapter contains a description of the experimental crystal growth equipment, and a discussion of the results obtained from bulk crystal growth by spontaneous nucleation. Also, an assessment of the suitability of different crucible materials for AlN crystal growth is made. In the third chapter, results from seeded growth of AlN on SiC substrates are presented and discussed, and a model for calculating stress distributions in AlN/SiC heterostructures is analyzed. The fourth chapter includes a summary and conclusions of the experimental work, and mentions potential topics for future research. A review of recent results of AlN crystal growth and an overview of selected characterization techniques are included in the appendices.

1.2 Aluminum nitride

1.2.1 Overview

AlN has a number of excellent properties that make it a highly desirable substrate candidate for III-nitride epitaxy. Its crystalline structure, hexagonal wurtzite (2H), is the same as that of hexagonal GaN, with a lattice mismatch in the c -plane of approximately 2.5%. Since AlN makes a continuous range of solid solutions with GaN, it plays an important role in GaN-based devices and is highly suited as a substrate for AlGaN devices with high Al concentrations or structures with graded layers. Its high thermal conductivity makes it desirable for high-temperature electronic and high-power microwave devices where heat dissipation is critical. The direct, large optical band gap makes it suitable for ultraviolet applications down to wavelengths as short as 200 nm. Its high resistivity is beneficial for high-frequency applications. It is also distinguished by high hardness, and chemical and thermal stability.

Past efforts to grow AlN bulk crystals have explored sublimation,^{6, 7, 8} vaporization,^{9, 10} and solution routes,^{11, 12} with sublimation yielding the most voluminous AlN crystals to date. Crystal growth by other methods, such as hydride vapor phase epitaxy^{13, 14} and ammonothermal growth,¹⁵ has been reported, but only crystals of either inferior quality or size have been produced thus far. In contrast, the efforts of several investigators (e.g. Slack and McNelly,¹⁶ Rojo *et al.*,⁶ Bickermann *et al.*¹⁷) clearly demonstrate that AlN bulk crystals of very high quality and of sizes appropriate for use as III-nitride substrates can be produced by sublimation growth. In this section, a brief historical perspective of AlN crystal growth will be presented along with a review of selected material properties. For a review of recent results of AlN bulk crystal growth, the reader is referred to Appendix A. Finally, the applications of AlN and related alloys will be discussed.

1.2.2 Historical perspective

The first AlN was produced in 1862¹⁸ by the reaction between molten aluminum (Al) and nitrogen. Ahrons¹⁹ later used a direct current arc between two Al electrodes in a nitrogen atmosphere. These processes produced Al-rich material because the initial AlN formed a protective skin over the Al that prevented further reaction, limiting their usefulness. The reaction of AlF₃ with NH₃ gas at 1000°C was used^{20, 21} more recently to produce stoichiometric AlN powder. Modern, commercial production of AlN powder typically involves direct nitridation of Al or carbothermal reduction of alumina followed by nitridation.

Fichter²² reported production of AlN crystals in an electrically heated furnace consisting of graphite (C) or tungsten (W) tubes, which was employed to heat AlN powder in

one atmosphere of nitrogen. Recondensed material consisted of metallic Al and AlN crystals. Crystals grown in C tubes contained C inclusions. Early reports of AlN bulk single crystal growth began to appear with increasing frequency after 1960. Most methods consisted of vapor transport in a nitrogen atmosphere, either by sublimation of AlN powder,^{9, 23, 24, 25, 26, 27} or by vaporization of Al metal.^{9, 28, 29, 30} Growth temperatures were varied from 1450°C to 2200°C. In some studies the crystal morphology varied with the growth temperature^{9, 25, 28, 30} and the degree of supersaturation in the vapor.²⁹ Taylor and Lenie⁹ reported that whiskers were grown in the temperature range 1450°–1750°C, prismatic needles occurred at 1800°–1900°C, and thin platelets were formed above 1900°C, based on direct temperature measurements by optical pyrometer. Drum and Mitchell²⁴ observed a mixture of basal platelets and whiskers with source temperatures from 1950°–2150°C, while only whiskers grew at source temperatures below 1900°C. Both Witzke²⁸ and Pastrnak and Roskovcova²⁹ discussed the orientations of as-grown faces of AlN crystals with different morphologies.

Crystal size varied over a wide range. Hexagonal prismatic needles grown by Taylor and Lenie⁹ were 0.5 mm in diameter and up to 30 mm long. Whiskers 18–20 mm long were grown with average growth rates of 1.5 mm/hr by Davies and Evans.²⁵ Flat plates oriented with the large faces parallel to the *c*-axis and normal to [1-210] were 0.1 mm thick and up to 3 mm long.²⁶ Similar platelets were reported by Collins *et al.*³¹

Differences in the coloration of these early crystals were also reported. Crystals were colorless^{27, 28, 30} or varied in color from white,⁹ to various shades of blue,^{9, 21, 28} to pale yellow,²⁶ and amber³¹ or brown²⁸. Taylor and Lenie⁹ investigated an earlier claim that blue coloration was due to the presence of aluminum oxycarbide (Al₂OC), which is isomorphous

with AlN. It was believed that formation of a solid solution between AlN and Al₂O₃ occurred from a reaction between Al and the carbon monoxide (CO) expected to be present in furnaces lined with graphite. Crystals were grown in controlled atmospheres of pure nitrogen, nitrogen with 0.5–2% carbon monoxide, and nitrogen with 1% methane. Blue crystals were grown only in the presence of CO, and a deeper shade of blue was observed with increasing amount of CO in nitrogen. Chemical analysis confirmed the presence of carbon and oxygen in the crystals.

Finally, a note on terminology. Upon heating to high temperature, solid AlN dissociates into Al and N₂ in the gas phase. Historically this process has been termed sublimation of AlN, even though it should be more accurately considered a decomposition reaction. While use of the term “sublimation” responds to the fact that a vapor is being formed directly from the solid, technically this term should refer to the creation of vapor species of the same substance as the solid. Clearly, with AlN decomposition this is not the case. However, use of the term “sublimation” in AlN crystal growth literature is prevalent. Faktor *et al.*³² used the phrase “dissociative sublimation” to describe the same type of reaction in crystal growth of the binary II-VI compounds. In keeping with accepted usage, the term sublimation will be retained with the understanding that a decomposition reaction is being described.

1.2.3 Material properties

Growth of high-purity AlN is a challenging task. As a result of the high affinity of Al for oxygen (the standard Gibbs free energy of formation at 298.15 K of Al₂O₃ is highly negative, -1.582×10^6 J/mol³³), oxygen is a common contaminant in AlN, and influences,

among other things, the lattice parameters, thermal conductivity, luminescence, and defect structure of AlN. Early material property measurements on oxygen contaminated AlN have been revised as higher purity single crystal material has become available. A brief review of the basic properties of AlN is presented below. Tabulated values can be found at the end of this section. For more information, the reader is referred to relevant review articles.^{2, 4, 34, 35}

1.2.3.1 Structural and elastic properties

The equilibrium crystal structure (α -phase) of the III-nitrides, AlN, GaN, and InN, is the wurtzite (2H) structure. A metastable β -phase with the cubic zincblende structure also exists. These two polytypes differ in the stacking sequence of the nitrogen and III-metal atoms: the stacking sequence of the (111) close-packed zincblende planes is ABCABC...; while the stacking sequence of the (0001) close-packed wurtzite planes is ABAB..., comprising bilayer sheets of nitrogen and III-metal atoms. The basic crystal structure consists of two interpenetrating sublattices that contain the nitrogen and III-metal atoms in tetrahedral coordination. The space group of the wurtzite nitrides is $P6_3mc$, the same as that of the hexagonal (4H and 6H) polytypes of SiC. Generally, the structure of binary, tetrahedrally-bonded semiconductors can be described in terms of assemblies of tetrahedra containing the element X (e.g. Si or Al) at the corners and the element Y (e.g. C or N) at the centroid of each tetrahedron.³⁶ The Y atom forms covalent-ionic bonds to each of the X atoms, with the degree of ionicity determined by the size and valence differences of the constituent atoms. The binary, tetrahedrally-bonded semiconductors can be built from assemblies consisting of variants of these tetrahedra, subject to the topological restrictions discussed by Pirouz.³⁶ This yields an infinite number of different possible structures, or polytypes. The polytypes are

conventionally denoted by their Ramsdell notation nL , where n is the periodicity of tetrahedra along the c -axis and L indicates the Bravais lattice. Hexagonal polytypes are obtained when n is an even integer, giving the 2H, 4H, and 6H polytypes that are relevant to this discussion.

The (hexagonal) conventional unit cell of AlN is shown schematically in Fig. 1.1. The structure can be described in terms of the edge length a_0 of the basal hexagon (a lattice parameter), the height c_0 of the hexagonal prism (c lattice parameter), and the internal u parameter giving the X-Y bond length along the c -axis in terms of c_0 , i.e the sublattice displacement along [0001] as a fraction of c_0 . For an ideal wurtzite structure $u = 0.375$, but bonding differences in the nitrides give rise to deviations from this value. In AlN, $u = 0.385$ and the Al-N bond length along [0001] is 1.918 Å.³⁷ The commonly quoted room temperature lattice parameters² of AlN are $a_0 = 3.112$ Å and $c_0 = 4.982$ Å. Conventionally, crystallographic planes and directions are denoted using four indices based on a four-axis Miller-Bravais coordinate system, consisting of three basal plane axes (a_1, a_2, a_3) at 120° angles to each other and a third axis (c) perpendicular to the basal plane.

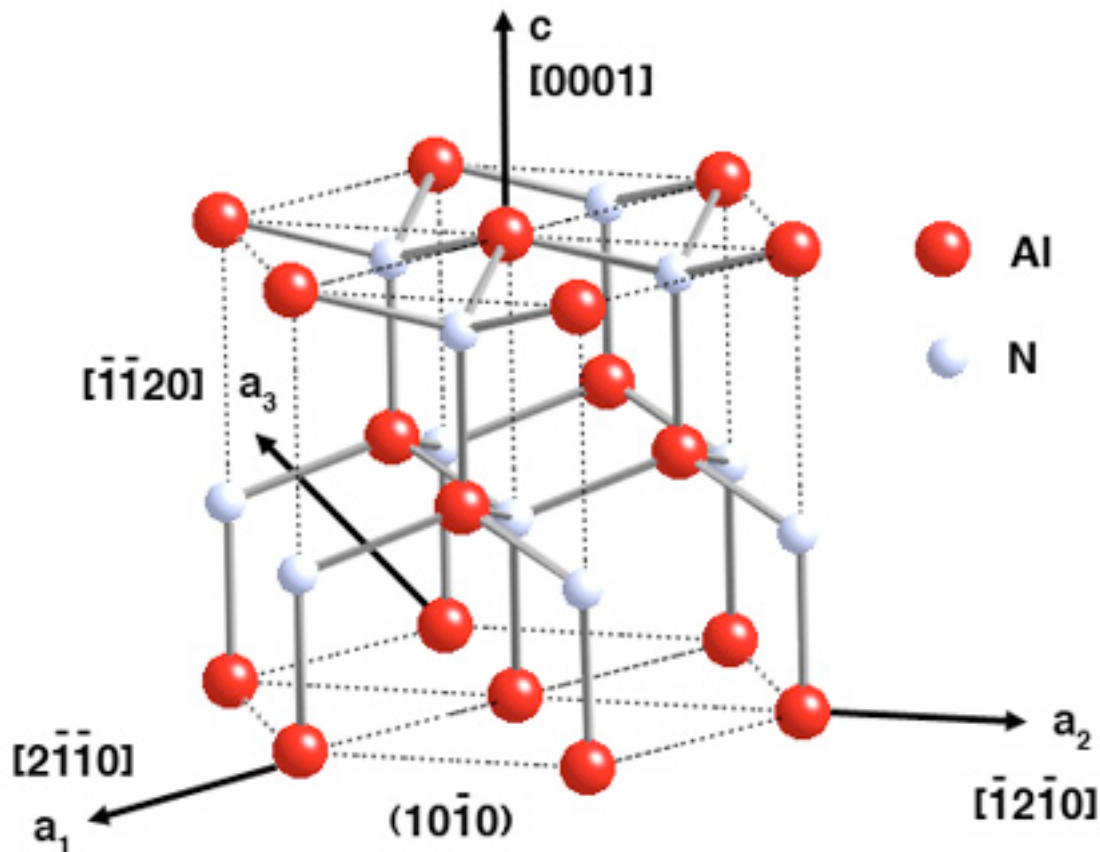


Figure 1.1. Schematic drawing of the hexagonal wurtzite conventional unit cell of AlN.

The wurtzite structure is non-centrosymmetric, and thus AlN possesses different properties along different $\langle 0001 \rangle$ polar directions. The polarity of AlN can be defined with respect to the position of the Al atom in the $\{0001\}$ bilayer.² In Al-face AlN, the Al atom occupies the top position in the bilayer, while in N-face AlN the top position is occupied by N, corresponding to filling by Al of either upward-pointing or downward-pointing tetrahedral sites (Fig. 1.2). The terms Al-face and N-face are used here to refer to the orientation of the AlN lattice, and describe lattices related to each other by an inversion operation. They do not refer to the surface termination, which is independent of the polar orientation. By convention the crystallographic $[0001]$ axis points from the N-face to the Al-face. Therefore, the Al-face

and N-face polarities are also referred to as $+c$ and $-c$ polar, respectively. Inversion domains (IDs) are extended defects that have a polarity opposite to the polarity of the surrounding crystal matrix. They have been studied in AlN sintered ceramics^{37, 38} and in thin films grown by metal organic chemical vapor deposition (MOCVD) on sapphire substrates,^{39, 40} and models of the domain wall structure have been formulated. The different response to etching of $+c$ and $-c$ polar $\{0001\}$ nitride surfaces has been observed in thin films and bulk crystals of GaN and AlN,^{41, 42, 43, 44} and can be used to identify defects such as IDs on these surfaces.

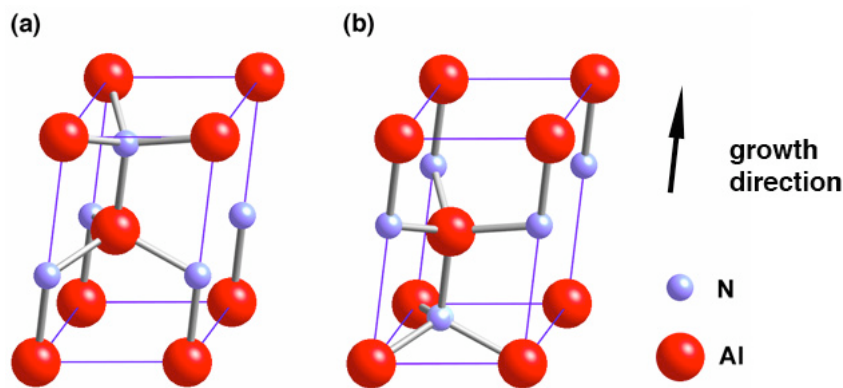


Figure 1.2. Schematic drawing of the AlN primitive unit cell indicating (a) Al-polar and (b) N-polar structures.⁴⁵

The five symmetry-allowed anisotropic elastic constants (elastic stiffness constants) for the wurtzite structure, denoted C_{11} , C_{12} , C_{13} , C_{33} , and C_{44} , have been determined for AlN from experiments and calculations. However, discrepancies exist between the reported data, making it difficult to evaluate which results are the most accurate. In some cases, the isotropic elastic constants (e.g. Young's modulus) have been measured; these measurements represent the averaged single crystal constants. The elastic moduli of polycrystalline, isotropic sintered AlN ceramics ($> 98.5\%$ dense) were determined by Gerlich *et al.*⁴⁶ from

measurements of the sound velocities. A room temperature value of ~ 308 GPa was obtained for the Young's modulus. Surface acoustic wave (SAW) velocity measurements were used by Dreger *et al.*⁴⁷ to determine the C_{ij} of AlN thin films. Wright⁴⁸, and Wagner and Bechstedt⁴⁹ calculated the elastic constants for AlN using density functional theory, and compared the results with previous measurements and theoretical calculations. Reeber and Wang⁵⁰ calculated the elastic constants in the 0–1350 K temperature range using an empirical corresponding state relationship. The values of the isotropic elastic constants used in chapter 3 of this thesis were taken from their earlier work.⁵¹

1.2.3.2 *Electronic and optical properties*

AlN has a direct band gap at the center (Γ point) of the Brillouin zone (BZ) exceeding 6 eV. In general, there are still many details concerning the band structure and optical properties of AlN that require further investigation. In the past, measurements of the band gap have been performed by optical absorption^{26, 52, 53, 54} and ellipsometry⁵⁵. Variations in the measured values were likely due to differences in crystal quality (i.e. impurity and defect concentrations). The room temperature value commonly quoted in the literature was 6.2 eV. Band-edge luminescence has been investigated using cathodoluminescence⁵⁶ and photoluminescence⁵⁷ (PL). In addition, the influence of different impurities on the absorption and luminescence has been studied by a number of investigators.^{58, 59, 60}

Recently, measurements on high-quality bulk crystals and epilayers have provided a more complete picture of the band structure. The conduction band has a single minimum (Γ_{7c}) at the BZ Γ point. The valence band, on the other hand, is split at the Γ point by the crystal field and the spin-orbit interaction. According to calculations,⁶¹ the spin-orbit splitting

ranges from 11 to 20 meV. The crystal field splitting at the top of the valence band in AlN was predicted^{62, 63} to be negative, in contrast to the other III-nitrides, but calculated values have ranged widely. However, this information gives a qualitative picture of the valence band ordering at the Γ point, and of the associated intrinsic free-exciton transitions. In order of increasing transition energies these are Γ_{7v} (upper, A exciton), Γ_{9v} (B exciton), and Γ_{7v} (lower, C exciton), shown schematically in Fig. 1.3. The square of the dipole transition matrix elements between the conduction band and the three Γ point valence states calculated by Li *et al.*⁶⁴ indicated that the A exciton transition is nearly forbidden for light polarized perpendicular (\perp) to the wurtzite c -axis, while the B and C exciton transitions are nearly forbidden for light polarized parallel (\parallel) to the c -axis. This picture has recently been confirmed by PL⁶⁴ and optical reflectivity measurements,^{65, 66} which have provided experimental values for the exciton resonances, the crystal field splitting parameter, and the fundamental band gap of AlN. The transition energies depicted in Fig. 1.3 were calculated using the values of the exciton resonances and binding energy E_x determined by Chen *et al.*⁶⁵ from reflectivity measurements on an AlN bulk crystal grown in this study. The fundamental band gap energy of unstrained AlN was determined to be 6.096 eV at 1.7 K. Note that the associated transition (A) is allowed for light polarized parallel to the c -axis. This may explain why earlier absorption measurements consistently resulted in larger values for the band gap; these measurements were typically performed with light polarized perpendicular to the c -axis, and likely probed the B or C transitions.

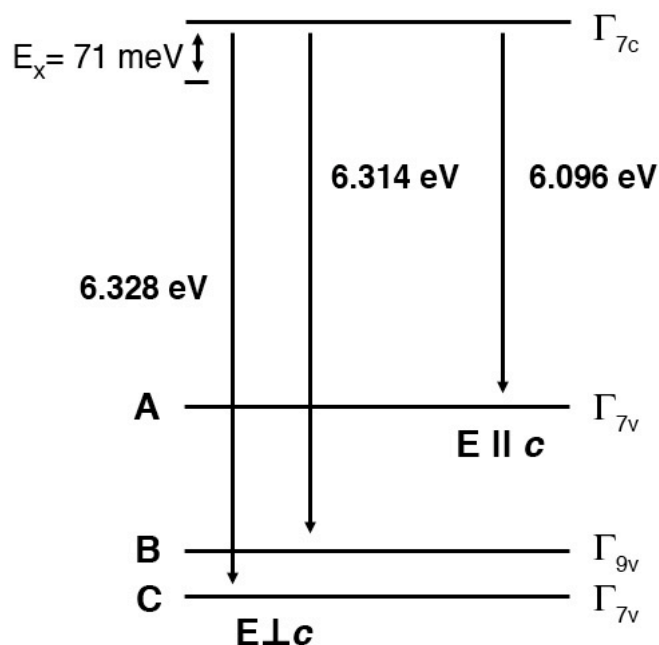
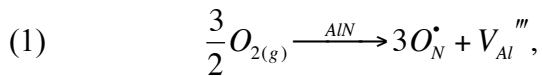


Figure 1.3. Schematic diagram of the band structure of wurtzite AlN showing selection rules for optical transitions at the Γ point. The A band exciton binding energy E_x is shown for reference.

1.2.3.3 Thermal properties

In hexagonal materials, the thermal expansion coefficients in the basal plane and along the c -axis are different and reflect the anisotropy of the structure. The thermal expansion of AlN has been determined experimentally^{9, 67, 68} from low to intermediate temperatures (77-1623 K) and has been predicted over a broader temperature range (25–2000 K) semi-empirically.⁶⁹ Slack and Bartram used x-ray lattice parameter measurements of AlN powder obtained by reacting high-purity aluminum trifluoride powder with ammonia (<1 wt% oxygen impurities) to determine the thermal expansion between 77 and 1269 K. Reeber and Wang⁶⁹ used a semi-empirical multi-frequency Einstein model to predict the thermal expansion of several materials, including AlN and 6H-SiC, at high temperatures.

The high thermal conductivity (κ) of AlN is a desirable property. Slack^{54, 70, 71, 72, 73} has been associated with a number of useful studies evaluating κ . The earliest of these⁷⁰ included results measured on single crystal and polycrystalline samples obtained from different growers. These results ($\kappa = 0.145\text{--}2.0 \text{ Wcm}^{-1}\text{K}^{-1}$ at 300 K) were compared with published values in the literature. The large variation in values was attributed to differences in the purity and density of the AlN. The most common impurities were oxygen and carbon. For samples where the dominant impurity was oxygen, the lattice parameter was found to decrease with increasing oxygen content. It is believed that oxygen enters the lattice and substitutes for nitrogen according to the following reaction:



such that for every three oxygen atoms incorporated on nitrogen sites there exists one aluminum vacancy (V). The resulting Al vacancies account for the shrinking of the lattice. It also appears that phonon scattering in oxygen-containing samples is caused by the mass defect of the Al vacancies. The thermal conductivity at 300 K of several samples was analyzed as a function of oxygen concentration, resulting in a trend that extrapolated to $\kappa = 3.20 \text{ Wcm}^{-1}\text{K}^{-1}$ for pure (oxygen-free) AlN. Single crystals grown by sublimation-recondensation in sealed tungsten crucibles were subsequently used to measure κ from 94.4 K to 1843 K.⁷¹ The room temperature (300 K) value⁵⁴ for a crystal with 400 ppm by weight oxygen content was $2.5 \text{ Wcm}^{-1}\text{K}^{-1}$, compared to $2.2 \text{ Wcm}^{-1}\text{K}^{-1}$ for polycrystalline ceramic material of similar oxygen content produced in the same study. More recently,⁷² the temperature dependence of κ was measured down to 0.4 K, giving a maximum of $23 \text{ Wcm}^{-1}\text{K}^{-1}$ at 52 K. The highest room temperature κ value⁷² reported by Slack for single

crystals was $2.85 \text{ Wcm}^{-1}\text{K}^{-1}$. Room temperature κ values exceeding those predicted by Slack for pure AlN were measured by scanning thermal microscopy on AlN grown by Rojo *et al.*⁷⁴ This $\kappa = 3.4 \pm 0.2 \text{ Wcm}^{-1}\text{K}^{-1}$ is the largest reported to date for AlN.

Table 1.1. Properties of wurtzite AlN (room temperature values unless otherwise noted).

Property	Value	Reference
Lattice constant (Å)	$a_0 = 3.112, c_0 = 4.982$	2
Density (g cm^{-3})	$\rho = 3.28$	35
Thermal conductivity ($\text{W cm}^{-1}\text{K}^{-1}$)	$\kappa = 3.4$	74
Thermal expansion coefficient (linear, 298-1300K, $\times 10^{-6} \text{ K}^{-1}$)	$\alpha_a = 5.72$ $\alpha_c = 4.75$	51
Young's modulus (GPa)	$E = 329.7$	51
Poisson's ratio	$\nu = 0.239$	51
Fracture strength (MPa)	$\sigma_c = 266$	9
Band gap (1.7K, eV)	$E_g = 6.096$	65

1.2.4 Applications of aluminum nitride and related alloys

Since AlN is both a good electrical insulator and thermal conductor, with a coefficient of thermal expansion closely matched to that of Si,⁷⁵ it is a very good candidate for replacement of toxic BeO, used as a heat sink in the electronics industry. Considerable research has been done on the production of sintered compacts of AlN, and commercially viable products have appeared over the last ten years. Through the use of sintering aids and

hot pressing techniques, AlN powder is fashioned into technical ceramic shapes, used primarily in heat sinking applications.

The most important applications of AlN, however, are related to the properties of the III-nitrides in general. These materials are good candidates for optoelectronic applications because they form a continuous alloy system whose direct optical band gaps in the wurtzite phase range from 0.7 eV for InN to 6.1 eV for AlN, potentially allowing band gap engineering in a wide wavelength range from infrared (~1770 nm) to deep ultraviolet (~200 nm). Their high thermal and chemical stability, breakdown electric fields, and maximum electron velocities are advantageous for application areas such as high-power, high-frequency, and high-temperature devices where classical semiconductors, such as silicon, and the conventional III-Vs (e.g. GaAs, AlAs, AlP) have fundamental limitations. In addition, the piezoelectric properties of AlN make it highly suitable for SAW devices. Presently, thin film structures of these materials are grown heteroepitaxially on sapphire and SiC substrates because of the lack of large nitride single crystals suitable for use as native substrates. The large amount of defects introduced in the grown layers as a result of lattice-mismatched growth limits device performance and lifetime. Thus, bulk crystal growth of AlN for the production of single crystal substrates is an important component in realizing the full potential of III-nitride devices.

1.3 Crystal growth

1.3.1 Overview

The vast majority of commercially-grown semiconductor bulk crystals are grown from the melt using one of several methods, such as the Czochralski, Bridgman, and vertical

gradient freeze methods. However, bulk crystal growth from the vapor is an alternative when melt growth is not possible, such as when the melting point is too high, the melt decomposes or the melt reacts with the crucible. Because of the high melting temperature and large dissociation pressure at the melting point of the III-nitrides,⁷⁶ bulk crystal growth from the melt is precluded. Two distinct vapor crystal growth techniques can be classified: physical vapor transport (PVT) and chemical vapor transport (CVT). In the context of this dissertation, we will discuss PVT, which is distinguished by a relative lack of chemical reactions in the gas phase.

1.3.2 Physical vapor transport growth

In a typical PVT process, source material held at a temperature below the melting point is sublimed within a closed or semi-open crucible, and the vapors are subsequently transported through a temperature gradient to a region held at a lower temperature than the source, where they recrystallize. The region where recrystallization takes place can consist of the crucible walls, in which case we speak of self-seeded growth, or it may consist of an intentionally selected seed crystal, in which case we have seeded growth.

The driving force for crystal growth from the vapor is the difference in chemical potential between the vapor and solid phases $\Delta\mu = \mu_v - \mu_c$, where μ_v and μ_c are the chemical potentials of the vapor and crystal, respectively. The decrease in the free energy of the vapor-solid system associated with the crystallization process promotes crystal growth.

Crystallization occurs when the vapor pressure p of the gaseous species at the vapor-crystal interface is higher than the corresponding equilibrium or saturated vapor pressure p_{eq} of the

solid phase, which is a function of temperature. Thus the vapor is supersaturated with respect to the crystal, with a degree of supersaturation σ defined in terms of the vapor pressures

$$(2) \quad \sigma = \frac{P - P_{eq}}{P_{eq}}.$$

Treating the vapor as an ideal gas, the chemical potential difference $\Delta\mu$, expressed in terms of the supersaturation σ , is given by

$$(3) \quad \Delta\mu = k_B T \ln\left(\frac{P}{P_{eq}}\right) = k_B T \ln(1 + \sigma) \approx k_B T \sigma,$$

where k_B is Boltzmann's constant and T is the temperature of the crystal. Therefore, the driving force for crystallization is roughly proportional to the supersaturation. The net vapor flux ϕ to the crystal surface is given from kinetic gas theory by the Hertz-Knudsen-Langmuir equation

$$(4) \quad \phi = \frac{\alpha(p - p_{eq})}{\sqrt{2\pi m k_B T}},$$

where α is the sticking coefficient, defined as the probability that an impinging vapor particle is adsorbed onto the surface, and m is the mass of the vapor species. This formulation allows one to estimate a maximum growth rate v_g^{max} for the PVT process from the equilibrium vapor pressures over the source (p_s) and seed (p_{eq}) by setting the sticking coefficient $\alpha = 1$ and ignoring the effects of gas phase diffusion between source and seed:

$$(5) \quad v_g^{max} = \frac{\Omega(p_s - p_{eq})}{\sqrt{2\pi m k_B T}} = C\sigma \quad ; \quad C = \frac{\Omega p_{eq}}{\sqrt{2\pi m k_B T}},$$

where Ω is the atomic volume. It is seen that the growth rate is proportional to the supersaturation. The estimation of growth rates in the case where mass transfer from source

to seed is limited by gas-phase diffusion has been considered by a number of investigators,^{77,}
⁷⁸ but is beyond the scope of this discussion.

In addition to vapor phase transport, processes at the crystal surface have been analyzed in the context of vapor phase growth. The maximum growth rate shown in equation (5) assumes there are sufficient sites available on the crystal surface for incorporation of adsorbed atoms (adatoms). This will tend to be the case if the crystal surface is rough, or if there are a large number of kink sites on the surface. Kink sites are special surface positions whose chemical potential is equal to that of the bulk crystal. Thus, they are favorable incorporation sites for adatoms and help determine the equilibrium with the vapor phase. Crystal surface roughness can arise as a result of a roughening transition, such as occurs when a flat surface is raised above a critical roughening temperature, or it can be related to geometrical roughness, such as is seen in certain high-index crystal planes. Crystal surfaces or faces can be classified into one of three types: (i) flat (F) faces, which are parallel to at least two dense (close-packed) atomic rows and tend to correspond to low-index planes below the roughening temperature; (ii) stepped (S) faces, which are parallel to one dense atomic row; and (iii) kinked (K) faces, which are not parallel to any dense atomic rows. The rough (S , K) faces grow by a different mechanism to the flat (F) faces.

The crystal growth theory developed by Burton, Cabrera, and Frank^{79, 80, 81} (BCF) over half a century ago explains the equilibrium structure of crystal surfaces, the movement of steps on crystal surfaces, and the rates of growth of crystal surfaces. At the time, it was understood that during crystal growth rough faces disappeared, leaving behind F faces, and growth continued by two-dimensional (2D) nucleation on the F faces. The probability of

forming 2D nuclei on a flat surface depended on the supersaturation such that below a critical supersaturation ($\sigma \sim 0.5$), it was almost negligible and no crystal growth would be observed. However, the supersaturations observed in real crystal growth ($\sigma \sim 0.01$) were significantly below the critical value. The BCF theory proposed that the existence of steps on the surface, which themselves contain a large number kinks, made 2D nucleation unnecessary. The steps required for growth could be supplied by dislocations with a screw component intersecting the growth surface. Frank⁸⁰ showed how the step due a dislocation wound itself into a spiral, effectively becoming an infinite source of steps.

According to BCF theory, during growth a flux of atoms from the vapor phase impinges on the surface. Atoms become adsorbed and these adatoms can execute jumps to adjacent surface sites or back to the vapor phase. They diffuse across the surface a characteristic distance x_s given by the Einstein formula:

$$(6) \quad x_s = \sqrt{D_s \tau_s},$$

where D_s is the surface diffusion coefficient and τ_s is the mean residence time, defined as the average amount of time an adatom would spend on an infinite flat surface before desorbing back to the gas phase. These quantities are given by

$$(7) \quad D_s = a^2 \nu' \exp(-E_{diff} / k_B T), \quad \tau_s = \nu^{-1} \exp(-E_{des} / k_B T),$$

where a is the lattice constant, ν and ν' are frequency factors on the order of the atomic frequency of vibration ($\sim 10^{13} \text{ s}^{-1}$), and E_{diff} and E_{des} are the activation energies for surface diffusion and desorption, respectively. BCF theory assumes that adatoms are efficiently incorporated at steps and therefore the surface concentration of adatoms near steps is maintained at its equilibrium value n_e . Far from steps, the adatom concentration n is in

equilibrium with the supersaturated vapor phase, such that $n = (1 + \sigma) n_e$. Using these quantities and the associated surface diffusion equations, the rate of (lateral) advance of a single step on the surface is given by

$$(8) \quad v_{\infty} = \frac{2\sigma\theta_e D_s}{x_s},$$

where θ_e is the equilibrium surface coverage given by n_e/n_t and n_t is the total concentration of surface sites.⁸² This solution implies that only a strip of width $2x_s$ around steps is active for the collection of adatoms.

A similar solution can be obtained for the rate of advance of a parallel train of steps

$$(9) \quad v = v_{\infty} \tanh(l/2 x_s),$$

where l is the average spacing between steps. The vertical growth rate v_g of the crystal is then given by $v_g = (h/l) v$, where h is the step height and v is given by equation (9). An example of a laterally growing parallel train of steps is experimentally realized in the growth of semiconductors on vicinal surfaces, which can be thought of as a series of terraces of low index notation separated by regularly spaced steps. In this case, crystal growth is commonly observed to proceed by the step flow mode, where steps advance laterally over the lower terraces. In the steady state described by the BCF theory, all steps move at the same velocity and the step velocity (and thus the vertical growth rate) is proportional to the supersaturation, as indicated in equations (8) and (9).

The PVT process has been used to grow a number of technologically important semiconducting compounds, including halides, II-VI compounds, IV-VI compounds, and SiC. SiC as an electronic material and as a substrate for III-nitride epitaxy has gained much attention over the last decade. The first breakthrough in SiC crystal growth came in 1955

when Lely⁸³ proposed a new method for growth of high-quality crystals based on self-seeded PVT growth. The material properties were studied over the next decades and interest grew in electronic applications for SiC. The next major breakthrough occurred in 1978 with the development of the seeded sublimation growth technique,⁸⁴ also known as the modified Lely technique. This development led to the fabrication of bulk crystals of SiC suitable for use as substrates for epitaxy. The material properties of SiC polytypes used as seeds in this study are shown below in Table 1.2.

Table 1.2 Properties of SiC (room temperature values unless otherwise noted).

Property	Polytype	Value	Reference
Lattice constant (Å)	4H	$a_0 = 3.073, c_0 = 10.053$	35
	6H	$a_0 = 3.0806, c_0 = 15.1173$	
Thermal expansion coefficient (linear, 298-1300K, x 10^{-6} K^{-1})	6H	$\alpha_a = 4.34$	51
		$\alpha_c = 3.74$	
Young's modulus (GPa)	6H	$E = 444$	51
Poisson's ratio	6H	$\nu = 0.164$	51
Band gap (< 5K, eV)	4H	$E_g = 3.26$	35
	6H	$E_g = 3.02$	

1.3.3 Identification of issues in aluminum nitride bulk crystal growth

In spite of the progress achieved in bulk AlN growth several key aspects still require attention. By necessity, sublimation growth is performed at very high process temperatures (typically > 2000 °C), making furnace design and materials selection critical to the success of

the overall process, both for achieving durability of growth hardware and keeping crystal impurity levels low. Crucible materials that are inert at high temperatures in the presence of Al vapor, that can withstand repeated temperature cycling, and that can be manufactured into various shapes at reasonable cost must be explored.

The AlN growth process must produce single crystal material in sizes large enough for use as substrates. Presently, single crystal boules 15 mm in diameter are being produced, but maximum crystal size must be scaled up. Also, a source of high-purity AlN is required. Commercially available AlN powder contains approximately 1 wt% oxygen impurities. Knowledge of the influence different contaminants have on the growth process and fundamental properties of AlN is still limited. In addition, seeded growth of AlN for control of crystal orientation is only recently being developed. Moreover, cracking of AlN crystals, either in self-seeded growth or in seeded growth on SiC, can be problematic. Deformed material around the boule periphery in contact with the crucible has been susceptible to post-growth cracking. While seeded growth on SiC holds the benefits of controllable crystal orientation and large seeds, reduction of cracks in the grown material is required for developing a reproducible seeded growth process.

These issues can be summarized as follows, and constitute the main thrust of research described in the following chapters. We need to:

- investigate a stable, high-temperature crucible material.
- scale up maximum crystal size.
- obtain a high-purity AlN source.
- learn how contaminants influence the growth process and properties.

- develop a reproducible seeded growth process.
- reduce post-growth cracking.

2 Aluminum Nitride Crystal Growth I: Spontaneous Nucleation

2.1 Objectives

AlN bulk crystal growth has been studied by a number of methods, including sublimation,^{6, 7, 8} vaporization,^{9, 10} hydride vapor phase epitaxy,^{13, 14} ammonothermal growth,¹⁵ and solution growth.^{11, 12} Sublimation of AlN powder at high temperature has shown the most promising results to date. This method has yielded crystals of very high quality and of sufficient size for device fabrication.^{85, 86} However, several issues still remain, as discussed previously. Lifetime and stability of growth crucibles and reactor parts remain a challenge that needs to be addressed. Further research is also needed to improve the understanding of the detrimental effects of various impurities in AlN, so that technologically relevant properties of AlN may be fully exploited by reducing the concentration of adverse growth contaminants.

In this chapter, sublimation growth of AlN bulk crystals in a resistively heated reactor by spontaneous nucleation on the crucible surfaces is investigated. A discussion of the reactor design and operation will first be presented. This will be followed by a brief review of thermodynamic and kinetic analyses of the AlN growth process. The experimental procedure will be described, after which the properties of several possible crucible materials for AlN growth will be discussed. Finally, the experimental results of crystal growth and characterization will be presented. The influence of process parameters (temperature and temperature gradient) and of different crucible materials on the observed crystal morphologies will be discussed. Also, the suitability of different crucibles will be assessed.

2.2 Reactor design and operation

AlN crystal growth experiments were performed in a resistively heated reactor equipped with a cylindrical graphite heater capable of reaching temperatures in excess of 2300°C. A schematic diagram of the reactor is shown in Fig. 2.1 (a). The heater surrounded a vertical reaction tube made of binderless, hot-pressed (HP) BN. The growth assembly, consisting of a crucible, supported by a pedestal mounted on a vertical support rod, was inserted in the reaction tube at the appropriate height in the reactor hot zone. The reactor hot zone featured an approximately flat temperature profile within the heater zone and steep temperature gradients at the heater boundaries. PVT growth was accomplished by vertically positioning the crucible relative to the graphite heater, thereby creating a temperature gradient between the bottom (hot) and top (cool) zones of the crucible that provided the driving force for sublimation/recondensation of AlN, as shown schematically in Fig. 2.1 (b). The temperature gradient was typically varied within a range of 0.5–5°C/mm for different crucible positions relative to the heater.

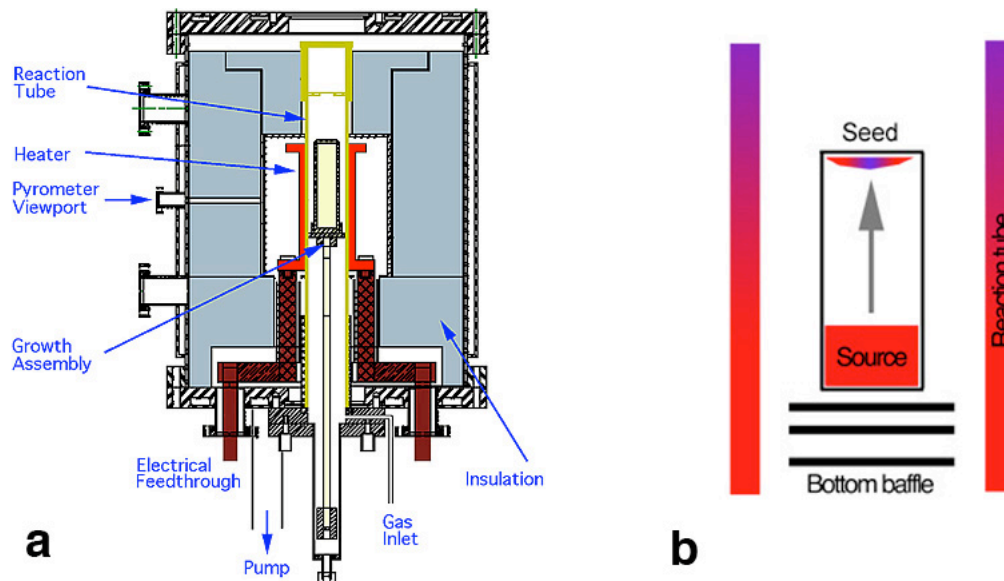


Figure 2.1. a) Schematic diagram of the resistively heated AlN growth system. b) Temperature gradients within the reactor hot zone, showing relative temperatures between the crucible bottom (hot) and top (cool).

The heater was surrounded by a heat shield made of HP BN and by graphite felt insulation. The stainless steel, double-walled chamber was water-cooled and had flanges for installation of a pressure transducer and viewports. Chamber pressure was measured by a Baratron gauge and kept constant using a pressure controller and butterfly valve that throttled the pumping speed of a mechanical pump. Crystal growth was typically performed at pressures ranging from 400–600 Torr. A hole was bored through the graphite insulation and BN heat shield for a direct line of sight between a side viewport and the heater surface. The heater surface temperature was monitored by a single-color pyrometer which had been calibrated against *in situ* thermocouple measurements in order to correct for the emissivity of graphite and for reflectance losses at the viewport surfaces. An additional viewport on the top

flange of the chamber allowed the temperature of the crucible top to be monitored with a second, hand-held pyrometer.

Two 16-inch, water-cooled flanges were located at the top and bottom of the chamber assembly; their location allowed maintenance to be performed on either the upper or lower portions of the chamber. The bottom flange contained the power feedthroughs, pumping port, and a flange for accessing the reaction tube. Crucibles were loaded and unloaded by opening this six-inch access flange. In addition, the 6-inch flange had a long extension welded to the bottom with an Ultratorr fitting on the lower end. A stainless steel rod that passed through the Ultratorr fitting and coupled internally to the vertical support rod of the crucible allowed the height of the crucible to be adjusted during loading, and to be shifted during growth as necessary by means of an external motor drive. The measured leak rate of the evacuated chamber at room temperature was typically on the order of 10^{-4} sccm, as measured by both the pressure rise method and commercial He leak detector (Pfeiffer).

Power was supplied to the heater by two 14 kW power supplies connected in parallel. A power output of approximately 10 kW (typically 20V, 500A DC) was required at an operating temperature of 2000°C. The power output was computer controlled by way of LabView software, which was also used to monitor, record, and/or control process parameters such as heater temperature, chamber cooling water temperature, chamber pressure, pump inlet pressure, and gas flow. Software-independent, safety hardware interlocks were designed into the process monitoring and control system in order to interrupt the supply of power to the heater in the event that any of the relevant process parameters (cooling water flow and temperature, chamber pressure, and heater temperature) deviated

from specified limits. Since a continuous flow of cooling water was critical to the safe operation of the reactor, a redundant water supply was incorporated into the design. In the event of loss of the primary cooling water flow, the heater power supply was shut down and a secondary flow source ensured safe temperature ramp-down.

Process gas flow was controlled by an MKS multi-channel flow control unit and mass flow controllers (MFCs). The flow rate of MFCs ranged from 0–1000 sccm. Nitrogen gas (UHP grade) was flown through the reaction tube in an upward direction. Experiments were typically performed under quasi-stagnant ($\sim 0.1 \text{ cm s}^{-1}$) gas flow.

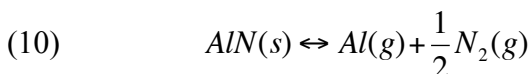
In the PVT process, the temperature distribution in the growth cell controls the crystal growth rate, the shape of the growth front, the powder source stability, and the thermoelastic stress. Since an understanding of the thermal field in the reactor was important for design of experiments and interpretation of experimental results, temperatures along the vertical axis of the reaction tube were measured experimentally under different process conditions and modeled numerically.⁸⁷ This twofold approach was employed because of the inherent difficulty in experimentally monitoring the thermal field in the reactor at elevated temperatures. When using capped crucibles, only the crucible top temperature was accessible to measurement by pyrometer. On the other hand, pyrometer measurements of the temperature at the bottom and top of open, empty crucibles could not accurately account for the thermal field present under experimental conditions, i.e. capped crucibles filled with AlN powder source. Thus the axial temperature distribution in the reactor was first measured with type C thermocouples which could be moved along the vertical centerline of the reaction tube; these measurements were performed with the growth assembly removed from the

chamber. The data was used to derive the thermal conductivity of the graphite felt insulation, an unknown model parameter. Once the felt conductivity was determined, the heat transfer in the entire system was simulated in order to assess the changes in the temperature distribution caused by insertion of the closed, filled crucible. The model showed that temperature gradients computed for the system with a filled crucible differed significantly from those computed without the crucible assembly, confirming that temperature measurements performed in an empty system did not accurately reflect experimental conditions. The greatest disturbance in the thermal field was near the bottom of the crucible where the powder source was located, resulting in a non-uniform temperature distribution in the source. In agreement with model calculations, non-uniform evaporation of the source charge was observed experimentally.

2.3 Experiment

2.3.1 *Thermodynamics and kinetics of aluminum nitride crystal growth*

In any analysis of the AlN growth process by PVT, several steps must be considered: (i) sublimation of source material, (ii) mass transport of gas phase species, (iii) adsorption of gas phase species on the growth surface, (iv) nucleation, including surface diffusion and incorporation, and (v) desorption. At the source surface, the decomposition of AlN is commonly assumed to proceed by the forward reaction:⁸⁸



Deposition at a lower temperature is then described by the reverse reaction. At equilibrium, the gas phase composition for this reaction can be calculated from the corresponding equilibrium constant and the tabulated thermochemical data:⁸⁹

$$(11) \quad K_p = P_{Al} (P_{N_2})^{1/2} = \exp\left(-\frac{\Delta G}{RT}\right) = \exp\left(\frac{\Delta S}{R} - \frac{\Delta H}{RT}\right)$$

where P_i ($i = \text{Al}, \text{N}_2$) refers to the partial pressure of the i^{th} gas species over AlN(s). For the stoichiometric vapor,

$$(12) \quad P_{Al} = 2P_{N_2}.$$

Equation (11) can then be expressed in terms of the P_i :

$$(13) \quad K_p = 2^{-1/2} (P_{Al})^{3/2} = 2 (P_{N_2})^{3/2}.$$

The vapor pressures of Al(g) and N₂(g) for the stoichiometric vapor in equilibrium with AlN(s) have been calculated over a range of temperatures by Slack and McNelly¹⁶ and Dryburgh.⁹⁰ In addition, Slack and McNelly provided a general discussion of equilibria in the system Al(l), Al(g), N₂(g), and AlN(s), with the following observations: for typical AlN growth pressures and temperatures (e.g. P = 100-800 Torr, T > 1800°C), AlN(s) is the only condensed phase present; above 2493°C AlN(s) in equilibrium with its stoichiometric vapor decomposes into Al(l) and N₂(g); and the temperature at which the total pressure inside a sealed container holding AlN reaches 1 atm is 2433°C.

PVT growth of AlN can thus be understood in terms of the solid/vapor equilibria established at the (hotter) source and (cooler) seed, which can be a crucible surface or growing crystal. The temperature gradient established between source and seed provides the driving force for transport of reactive species. Since AlN growth is typically performed under

conditions where the partial pressure of $N_2(g)$ is many times larger than that of $Al(g)$ (i.e. in nitrogen atmosphere), then in the absence of any other kinetic limitations, supply of $Al(g)$ to the seed will be the rate limiting step. Given this, the growth rate is proportional to the flux of $Al(g)$ transported in the gas phase, which in turn is proportional to the difference in the equilibrium partial pressures of $Al(g)$ above the source and seed surfaces.

An approach similar to that described in the preceding paragraph has been used by several investigators to derive expressions for the growth rate of AlN by sublimation. The maximum growth rate in a sealed ampoule was calculated⁹⁰ from kinetic theory formulations which included an experimentally measured⁹¹ N_2 condensation (sticking) coefficient in the Hertz-Knudsen-Langmuir equation. Growth rates in the range of 187–9360 $\mu\text{m/hr}$ were obtained. A two-dimensional model of mass transport in the gas phase was analyzed by Liu and Edgar,⁹² who determined that the activation energy for AlN growth at pressures over 200 Torr was 681 kJ/mol, which is close to the heat of sublimation of AlN. A one-dimensional mass transfer model was developed by Noveski *et al.*⁷⁸ for the high-temperature growth, which showed that the growth rate is diffusion limited at total N_2 pressures in the range of 400–800 Torr. In other efforts,^{93, 94} two mechanisms of vapor transport were identified: at high pressure (760 Torr), vapor transport was controlled by diffusion in the gas phase, while at low pressure (10^{-4}) Torr, it was dominated by drift of the reactive species, Al and N_2 .

Several authors have also studied the influence of surface kinetics on AlN growth. In particular, it appears that the low sticking coefficient of N_2 on AlN manifests a kinetic limitation to the AlN growth rate at low N_2 pressures. This has been explained⁹⁵ by assuming the existence of a physisorption precursor at the nitride surface, as developed from studies of

MBE growth. Due to the high dissociation energy⁹⁶ of the N₂ molecule, 9.76 eV/molecule, atomic nitrogen is not predicted as a gas phase species. Thus N₂ adsorption is a necessary step in the growth process. However, molecular nitrogen interacts poorly with nitride surfaces. Under the assumption that the evaporation and sticking coefficients are equal, which is valid for a surface in equilibrium with its vapor,⁹⁷ the sticking coefficient of nitrogen has been measured by Langmuir free evaporation⁸⁸ studies and effusion.⁹¹ Averyanova *et al.*⁹⁵ have used these measured values to formulate a temperature-dependent expression for the evaporation coefficient of N₂:

$$(14) \quad \alpha_e = 7.14 \times 10^8 \exp\left(-\frac{61272}{T[K]}\right)$$

Thus the N₂ adsorption rate is increased in AlN growth through higher (i) temperature, by increasing the sticking coefficient and (ii) nitrogen partial pressure, by increasing the N₂ impingement rate.

The above analysis assumes that the only gas phase species of any significance are Al and N₂. An early mass spectrometric study⁹⁸ reported only the presence of these two species. Recently, though, several studies^{99, 100} have detected Al_nN (n= 2, 3, 4) species. A first principles gas phase composition calculation¹⁰¹ has indicated that these Al_nN species, though present in much smaller mole fractions than Al and N₂, are supersaturated with respect to the AlN crystal and may contribute to the growth. However, little is known about the kinetics of these species. What effect they have on AlN bulk crystal growth has yet to be determined experimentally.

2.3.2 *Experimental procedure*

Prior to loading in the reactor, the weights of the crucible, crucible cap, and source charge were measured and recorded. These measurements were compared to the values obtained after growth to determine the amount of source material evaporated, crystal deposition, and source mass loss out of the crucible, and to quantify the variation in these amounts as a function of process parameters. Several grams of source material were filled into the crucible, which was loaded into the reaction tube at the appropriate height. The source was used either as-received or after previously sintering it at elevated temperature in nitrogen atmosphere, as explained below (section 2.5.3). The as-received source was commercially purchased AlN powder with approximately 0.5 wt% impurities; primarily oxygen, 0.1 wt%, and carbon, 0.3 wt%, as determined by glow discharge mass spectrometry (GDMS).

After loading, the reactor was pumped down to the base pressure of the mechanical pump (~2 mTorr) to remove residual oxygen and water vapor, then filled with UHP N₂ gas to the desired growth pressure. Once operating pressure was reached, the N₂ gas flow was adjusted to a quasi-stagnant flow rate of 100 sccm, and the heater power was gradually ramped up using software control. Depending on the ramp rate and desired final temperature, growth temperature was reached within 3–6 hrs. During growth all process parameters were periodically monitored to ensure stable operation, and pyrometer measurements of the crucible top temperature were performed as deemed necessary. Once the growth run was finished, heater power was ramped down, the chamber was cooled to room temperature, the crucible was removed from the reaction tube, and the crucible contents were examined. The

location and appearance of crystals spontaneously nucleated on the crucible walls and cap were recorded prior to removal.

2.3.3 *Characterization techniques*

Grown crystals were examined by optical microscopy using a Bausch and Lomb stereo microscope with 10–70x magnification, and an Olympus BH-2 compound microscope with 50–1000x magnification, brightfield/darkfield illumination, and polarized light and differential interference contrast imaging capabilities. Synchrotron white beam x-ray topography (SWBXT) was performed at the Stony Brook Synchrotron Topography Station, Beamline X-19C, at the National Synchrotron Light Source, Brookhaven National Laboratory. X-ray topographs revealed the distribution of structural defects such as dislocations, inclusions, low-angle grain boundaries, and growth sector boundaries. Topographs were recorded on 8 inch x 10 inch Kodak Industrex SR-45-1 high-resolution x-ray film. Crystalline quality of the grown crystals was also assessed by high-resolution x-ray diffraction (HRXRD) performed at SUNY, Stony Brook using a Bede D1 high-resolution diffractometer system with Cu $K_{\alpha 1}$ radiation. Chemical composition of the crystals was analyzed by GDMS (VG 9000) and secondary ion mass spectrometry (SIMS, PHI Quadrupole). An overview of SWBXT, HRXRD, and GDMS can be found in Appendix B. Low-temperature (1.7 K) optical reflectance measurements were performed at Arizona State University on a bulk AlN single crystal with a naturally occurring *m*-face. Incident light was provided by a high radiance 30 W deuterium lamp that was dispersed by an ISA HR-320 monochromator with a 2400 grooves/mm grating. The angle of incidence was $\sim 45^\circ$.

Reflected light was collected by a Hamamatsu R-1754 photomultiplier tube. All spectra were normalized to the reflectance of a double side polished sapphire substrate.

2.4 Crucibles for aluminum nitride growth

2.4.1 Objectives

The very high process temperatures (typically $> 2100^{\circ}\text{C}$) required to achieve significant growth rates ($> 100 \mu\text{m/hr}$) in AlN bulk crystal growth by sublimation of an AlN powder source impose restrictions on the choice of reactor hot-zone materials. Furnace design and materials selection are critical for achieving durability of growth hardware and keeping crystal impurities low. In particular, crucible materials must withstand repeated temperature cycling and highly reactive Al vapor. The suitability of different crucible materials is based on several criteria. Certainly, any given material is not expected to satisfy all criteria perfectly, but ideally crucibles should be (i) refractory and compatible with elevated growth temperatures, (ii) inert to chemically aggressive Al vapor, (iii) a negligible source of contamination to the growth process, (iv) re-usable for multiple growth runs, (v) relatively inexpensive, and (vi) manufacturable in various shapes and dimensions.¹⁰²

As different research teams developed AlN bulk crystal growth processes based on the sublimation technique, a number of refractory crucible materials have been tested with varying success. Some of these results are reviewed in Appendix A. Notably, Slack and McNelly,¹⁶ Shi *et al.*,¹⁰³ and Epelbaum *et al.*¹⁰⁴ have reported using W crucibles and/or furnace fixtures. Crucibles made of graphite,¹⁰⁵ SiC-coated graphite,¹⁰⁶ and HP BN⁷ have also been tested. In the present study a survey of the influence of reaction crucibles on AlN crystal growth and morphology will be presented.¹⁰⁷ The materials tested will also be

evaluated with respect to the criteria stated above. Crucibles were typically 6–8 cm high and had an inner diameter of 2.5 cm.

2.4.2 Boron nitride

Hexagonal BN powders are produced in a wide variety of grades for applications ranging from cosmetics to lubrication in extreme temperature, pressure, and chemical environments. The powder is hot pressed to form a dense, easily machinable engineering material. HP BN possesses high thermal stability, excellent resistance to thermal shock, and low thermal expansion, making it a natural choice for refractory shapes and coatings. Binderless HP BN is the highest purity commercially available grade (>99% pure). Based on this combination of properties, binderless HP BN was chosen as a crucible material for initial experiments in this study. Crucibles were machined on a lathe out of HP rods. They were cleaned in organic solvents prior to use in the reactor.

2.4.3 Refractory metals

Crucibles made of W and Ta metal (99.95% metals basis) were obtained from commercial vendors. These elements were selected for their high melting points (Table 2.1) and low vapor pressures¹⁰⁸ at typical AlN growth temperatures. Both materials possess high tensile strength and hardness, making them difficult to machine. Welding requires specialized equipment. Only Ta foils are ductile enough at room temperature to be easily rolled into cylindrical shapes. Ta has excellent corrosion resistance to many acids, organic chemicals, and liquid metals. Both metals are oxidized at elevated temperatures.

2.4.4 Refractory metal carbides and nitrides

Refractory carbides and nitrides generally share many similarities due to their structural and bonding characteristics. They are characterized by high hardness, melting point, and chemical stability. The host lattice of the early transition metals is large enough to accommodate the carbon (nitrogen) atoms in interstitial positions. The difference in electronegativity and atomic size between constituent atoms of the interstitial carbides (nitrides) is typically high, and the bonding, while mostly metallic, has covalent and ionic components.¹⁰⁹ As a result, these materials exhibit a combination of metallic characteristics (high thermal and electrical conductivity) and ceramic characteristics (high hardness and strength). They also possess higher melting points (Table 2.1) and bond strengths than those of the host metal. The most common compounds found are the monocarbides and mononitrides (i.e. chemical formulae MC and MN, where M refers to the metal atom), but it should be noted that these are primarily non-stoichiometric phases due to the formation of carbon vacancies, and both nitrogen and metal atom vacancies, in the carbides and nitrides, respectively. TaC possesses the highest melting point of any of these compounds, 3950°C, and was chosen as a potential crucible material for further study. TaN also features a high melting point, 3093°C, and is expected to be compatible with nitrogen atmosphere at elevated temperatures. Crucibles made of high-temperature sintered TaC and TaN powders, and TaC-coated graphite were evaluated.

2.4.5 Other materials

Crucibles made of Re (99.95% metals basis) and Y₂O₃-stabilized cubic ZrO₂ were also tested in this study and found incompatible with the presence of Al at elevated

temperatures, resulting in uncontrolled reactions between the crucible and Al vapor, and subsequent structural failure of the crucible.

AlN powder can be formed into a dense material by using sintering aids and hot pressing.¹¹⁰ It has become important as a substrate material for electronic thermal management, in particular as a replacement for toxic BeO. In order to obtain a sintered body with the desired properties, such as high thermal conductivity, control of the sintering behavior is critical. Yttria (Y_2O_3) is the best aid for AlN sintering; reactions between the AlN surface oxide and the oxide additive form a liquid that promotes particle rearrangement and densification.¹¹¹ Sintered AlN crucibles were obtained from a commercial vendor. These crucibles gradually evaporated during high-temperature growth, limiting their usefulness in multiple experiments. Even though large AlN single crystals were obtained in these crucibles, they should be avoided due to contamination of the growth environment with oxygen.

Table 2.1. Melting points of selected refractory elements, borides, nitrides, and carbides.¹⁰²

Elements	Ta	2996°C
	Os	3045°C
	Re	3180°C
	W	3410°C
	C	3550°C
Borides	TiB ₂	2980°C
	NbB ₂	3000°C
	ZrB ₂	3040°C
	TaB ₂	3200°C
Nitrides	TiN	2950°C
	ZrN	2980°C
	BN	3000°C
	TaN	3093°C
	HfN	3387°C
Carbides	WC	2870°C
	ZrC	3420°C
	NbC	3600°C
	TaC	3950°C

2.5 Results and discussion

Earlier experiments^{10, 112} performed in the resistively heated reactor based on vaporization of metallic Al in nitrogen atmosphere showed that N₂ gas flow rate and pressure (within the 300–700 Torr range) had only a minor influence on crystal morphology. Rather, temperature and temperature gradient were the crucial growth parameters in vaporization experiments. For an optimum temperature gradient of approximately 5°C/mm, the crystal shape and fastest growth direction was found to strongly depend on the growth temperature:

at relatively low temperatures (1800–1900°C) long hexagonal needles were grown, temperatures around 1900–2100°C yielded twinned platelets, while *c*-platelets were formed at temperatures above 2100°C. During these experiments a slowdown in the growth rate of crystals was observed after 2 hrs growth, which was attributed to a decreasing Al flux from the Al source due to the progressive formation of an Al-rich, polycrystalline AlN coating over the molten Al. In the following, the N₂ flow rate was kept in the range of 100–150 sccm and the reactor pressure was 400 Torr. Crystals were grown by heating AlN source powder, since this yielded a stable Al flux over several days of growth. Experiments were carried out at elevated temperatures (2100–2300°C) in order to obtain vapor pressures of Al over AlN comparable with those above metallic Al in the vaporization experiments.

2.5.1 Growth in boron nitride crucibles

Spontaneously nucleated AlN crystals grown in BN crucibles were transparent and virtually colorless. At lower temperatures (<2100°C) thin, hexagonal needles were grown along the *c*-direction at growth rates in excess of 1 mm/hr. Thin platelets were obtained at growth temperatures in excess of 2100°C. SWBXT and HRXRD were used to assess the orientation and crystalline perfection of some of these crystals.¹¹³ Fig. 2.2 (a) is an optical photograph of an as-grown crystal showing well-defined growth facets. Transmission x-ray topographs are shown in Figs. 2.2 (b) to (d). Pendellösung fringes (PF) are observed at the top and right edges of the crystal where there is a gradual change in crystal thickness and are indicative of the high degree of crystalline perfection achieved. Growth dislocations (D₁) originating at the bottom edge are of screw type with Burger's vectors along the [01-10] direction, as indicated by the observed contrast extinction in the (0002) and (2-1-10)

reflections. Another group of dislocations (D_2) is observed along the lower edge, where the crystal was detached from the crucible. These dislocations curve into loops and are likely caused by plastic deformation. Overall, the dislocation density is around 10^3 cm^{-2} , and rises to approximately 10^4 cm^{-2} in the regions of growth and deformation-induced dislocations. Large regions of the crystal are dislocation-free. A HRXRD plot of the (11-20) double crystal rocking curve (DCRC) and reciprocal space map (RSM) taken from this crystal are shown in Figs. 2.3 (a) and (b). The measured triple crystal rocking curve (TCRC) width of 7 arcsec is very close to the calculated perfect crystal rocking curve width for the (11-20) reflection of about 6 arcsec. These results reflect the high crystalline perfection observed in the topographs.

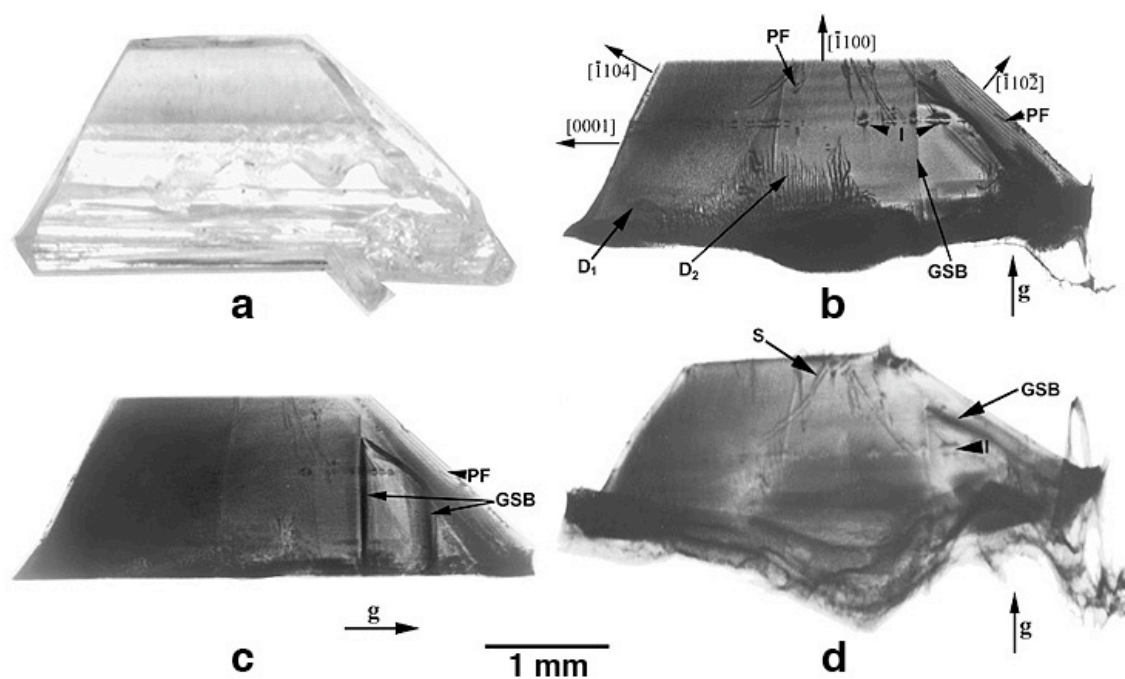


Figure 2.2. Structural characterization of a spontaneously nucleated AlN crystal. a) Optical photograph showing well-defined growth faces.¹¹³ Transmission x-ray topographs: b) $g = -1100$, $\lambda = 0.75 \text{ \AA}$, showing inclusions (I), growth sector boundaries (GSB), growth dislocations (D_1) and dislocation loops (D_2), Pendellösung fringes (PF) are observed on the upper and right wedged edges; c) $g = 000-2$, $\lambda = 0.43 \text{ \AA}$; and d) $g = -12-10$, $\lambda = 0.81 \text{ \AA}$, in which the growth dislocations are extinguished.

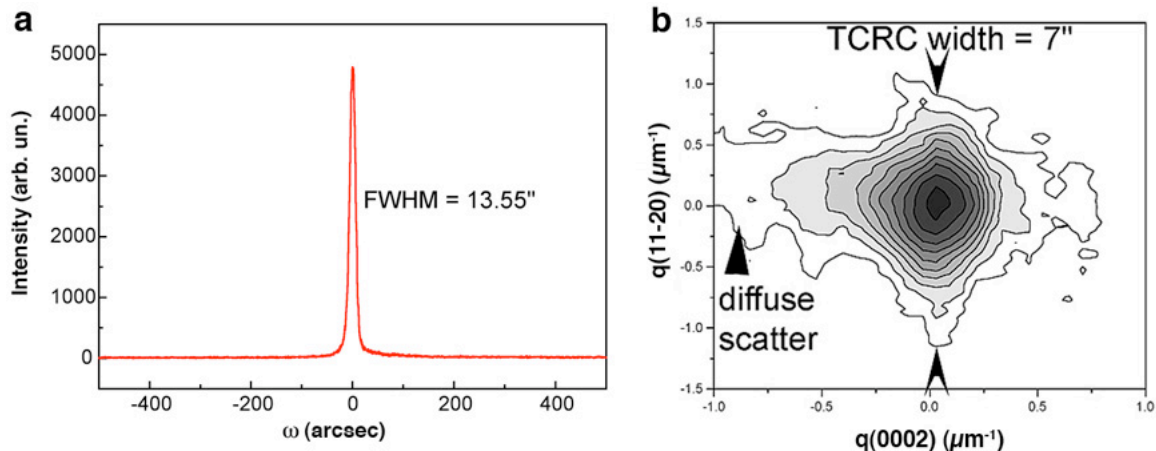


Figure 2.3. HRXRD of the crystal in Fig. 2.2. a) Double crystal (11-20) rocking curve. b) (11-20) RSM showing a TCRC width (7 arcsec) close to the calculated perfect crystal width of 6 arcsec.

Two distinct platelet morphologies were observed as a function of the temperature gradient between the source and crystal growth region. Platelets with the crystallographic c -direction in the plane of the crystal were grown in small temperature gradients ($< 2^\circ\text{C}/\text{mm}$). They were characterized by growth ridges, bounded by alternating $\{10-10\}$ and $\{11-20\}$ families of planes, running along the c -direction, as shown in Fig. 2.4 (a). This feature has been observed by other investigators⁷ and seems characteristic of crystals grown in BN crucibles. These characteristic surface ridges were not observed in crystals grown in other crucible materials. Elemental analysis (see below, Table 2.2) of these crystals indicated that 100 ppm wt of boron was incorporated. Boron incorporation was reduced approximately three-fold and isotropic growth rates were observed when growth was performed in crucibles other than BN. Residual boron contamination observed in crucibles other than BN was attributed to the presence of the BN reaction tube. Calculations^{108, 114} of the vapor pressure of boron over BN at 2300°C under 1 atm N_2 , and under the same conditions in the presence of

graphite, yielded values of $\sim 7 \times 10^{-5}$ atm and $\sim 1 \times 10^{-5}$ atm, respectively. These values are several orders of magnitude higher than the corresponding values of the metal atom vapor pressure over its refractory carbide or nitride for other refractory carbides and nitrides.^{108, 114} Thus boron contamination of the crystal growth environment is expected to be significant when using BN crucibles and will be greater than the corresponding metal atom contamination from other, more stable refractories such as TaN and TaC.

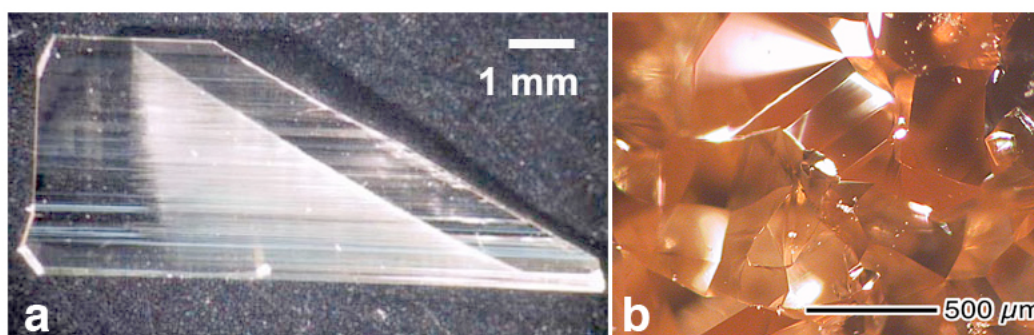


Figure 2.4. a) Photograph of an AlN crystal grown by spontaneous nucleation in a BN crucible. The c -direction is in the plane of the crystal, aligned along the growth ridges. b) Photograph of coalesced AlN crystals grown in a W crucible exhibiting well-faceted surfaces and characteristic orange color.

In larger temperature gradients ($2\text{--}5^\circ\text{C}/\text{mm}$), c -platelets were formed in BN crucibles. One such crystal is shown in Fig. 2.5 (a). It features a smooth c -plane, and is bounded above and below by well-defined growth faces parallel to the $(-12-10)$ plane. Growth was fastest along the $[10-10]$ and $[-1010]$ directions. The transmission x-ray topographs in Figs. 2.5 (b) and (c) show distortion due to bending of the lattice planes from residual stresses in the crystal. The dark band running horizontally across the middle of the crystal in Fig. 2.5 (c) is absent from Fig. 2.5 (b), indicating that the bend axis is parallel to $[-1010]$. The topographs

also indicate that this crystal is essentially dislocation-free. The tilt broadening measured in the (0002) DCRC of Fig. 2.6 (a) is thus attributed to bending. The measured (0002) TCRC, Fig. 2.6 (b), is 8 arcsec (comparable to the calculated perfect crystal rocking curve width of 7.8 arcsec), indicating very high crystalline perfection. However, the highly anisotropic growth rates, such that growth was nearly inhibited along one crystallographic direction, made coalescence and crystal-size expansion difficult to achieve in BN crucibles. Recently a model¹¹⁵ has been proposed to explain the smooth *c*-planes observed in these crystals, showing how B trace impurities selectively influence surface kinetics during AlN single crystal growth. As a result of these experimental observations and theoretical simulations, crucible materials that would not contaminate the growth environment with boron were investigated.

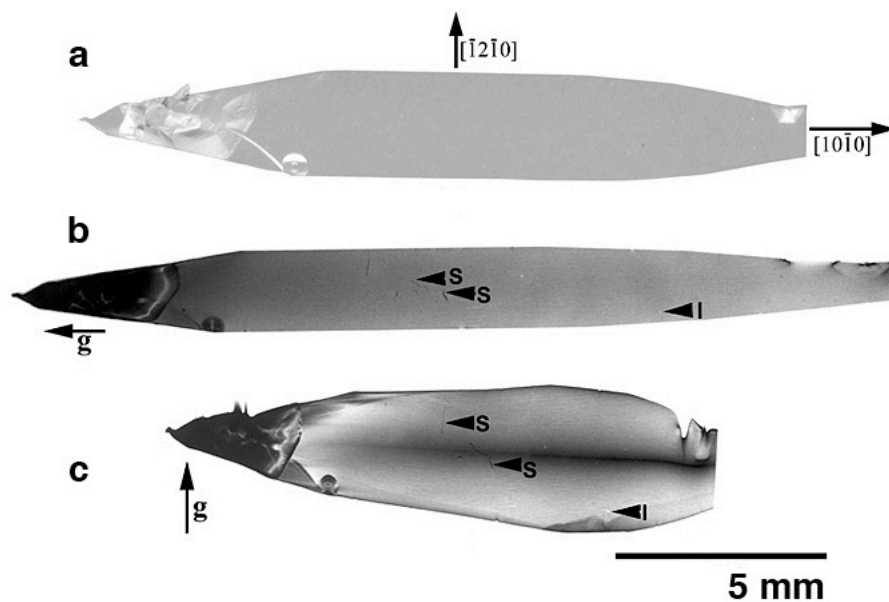


Figure 2.5. Structural characterization of an AlN *c*-plate. a) Optical photograph of an AlN crystal showing well-defined $(-12-10)$ growth faces on the top and bottom.¹¹³ Transmission x-ray topographs: b) $g = 10-10$, $\lambda = 0.84\text{\AA}$; c) $g = -12-10$, $\lambda = 0.43\text{\AA}$; showing inclusions (I) and surface scratches (S).

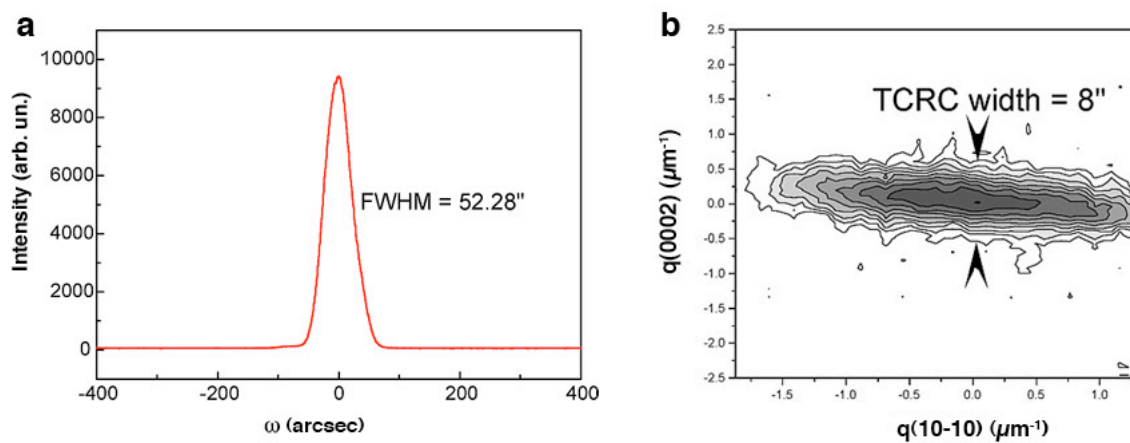


Figure 2.6. HRXRD of the crystal in Fig. 2.5. a) Double crystal (0002) rocking curve showing tilt broadening due to crystal bending. b) (0002) RSM showing a narrow TCRC width (8 arcsec).

2.5.2 *Growth in refractory metal and metal carbide or nitride crucibles*

In contrast to the results obtained in BN crucibles, crystals grown in crucibles made of W, Ta, TaN, and TaC all exhibited nearly isotropic growth rates. Crystal coalescence was therefore much easier to achieve in boron-free crucibles. Polycrystalline AlN grown in W and Ta crucibles exhibited well-faceted surfaces and a deep orange color, as shown in Fig. 2.4 (b). Refractory metal crucibles suffered cracks and were prone to complete failure after cycling several times to high temperature. It has been reported that W is prone to grain boundary attack by the Al vapor.¹⁶ Additionally, in the presence of C contamination W forms a carbide (WC) with a significantly lower melting temperature than the element (Table 2.1), and calculations¹⁰⁸ have indicated possible formation of a eutectic between solid AlN and W at 2326°C. The process contributing to the brittle fracture observed in the thin-walled (0.76 mm) Ta crucibles is potentially related to grain coarsening and nitridation. Grain growth at elevated temperature leads to grain coarsening of the polycrystalline metal and a reduction in tensile strength. In the presence of nitrogen, Ta forms Ta₂N and TaN; both transformations are accompanied by large volume changes. Since the transformation occurs faster along the grain boundaries, this results in non-uniform internal stress and grain boundary embrittlement. Therefore, in the interest of extending crucible lifetimes, crucibles made of high-temperature-sintered TaN and TaC powders were evaluated.

Dense polycrystalline AlN boules up to 10 mm thickness and 25 mm diameter were deposited in TaN and TaC crucibles at growth rates of 300 μm/hr. In the temperature range 2100–2300°C, bulk single crystals up to 10 mm in size were grown with growth rates between 100–300 μm/hr. Crystal coloration was significantly reduced when compared to

growth in pure W or Ta crucibles. Fig. 2.7 shows the results of SWBXT and HRXRD analyses of single crystals. As was the case with AlN grown in BN crucibles, crystals were nearly dislocation-free with TCRC widths close to the theoretical values for perfect crystals. In contrast to refractory metal crucibles, sintered crucibles withstood repeated high-temperature cycling, with crucible lifetimes in some cases exceeding 500 hours at growth temperature. No significant reaction with Al vapor was observed in these materials. Graphite crucibles coated with TaC were also tested; while crystal growth for short periods of time yielded similar results, failure of the coating, typically through pinhole formation at longer growth times, introduced carbon contamination in the growth environment, leading to inferior crystals.

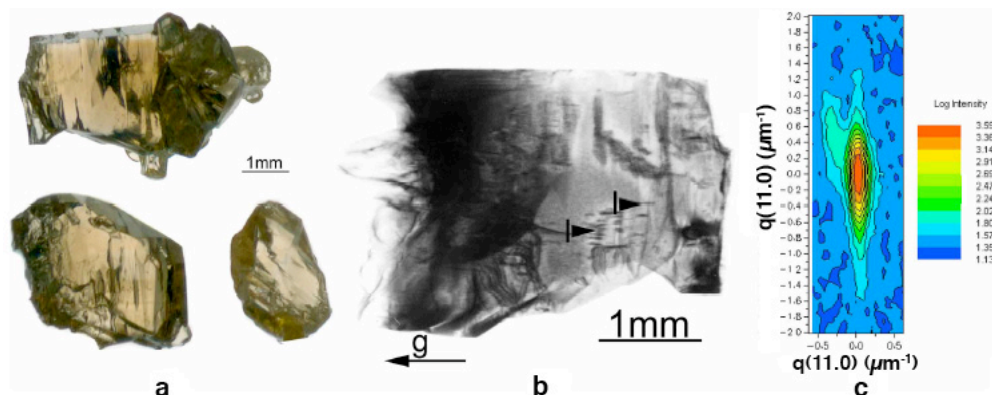


Figure 2.7. Structural characterization of AlN crystals grown in a TaN crucible. a) Optical photograph of AlN single crystals. b) Transmission x-ray topograph of the topmost crystal in (a) showing inclusions (I) and lack of dislocations. c) (11-20) RSM of this crystal, yielding a TCRC width of 9.2 arcsec which is close to the calculated perfect crystal rocking curve width of 6 arcsec.¹⁰⁷

2.5.3 *Elemental analysis*

In an effort to quantify contamination levels of crystals grown under different conditions, representative samples were analyzed by GDMS and SIMS. Table 2.2 shows the results of GDMS analysis performed on AlN source powder and on crystals grown in BN and TaN crucibles. Source powder was analyzed as-received and after sintering in nitrogen atmosphere for 14 hours at a temperature of 2200°C. Sintering of the source powder resulted in a significant reduction of nearly all impurities. PVT and recondensation during the growth further reduced the content of several impurities incorporated in the crystals. In order to compare impurity levels found in the source material with those found in the grown crystals, it should be noted that a pre-sintered source was employed during crystal growth in BN, while growth in TaN was from as-received powder. Notably, boron contamination was reduced in TaN crucibles (28 ppm) as compared to BN crucibles (100 ppm). Even so, the amount of boron probably does not reflect the total reduction possible in TaN crucibles since the reactor hot zone contains a cylindrical BN reaction tube between the crucible and graphite heater. Reduction of boron contamination in the growth environment is desirable because of its effects on crystal morphology, noted previously. Tantalum content of crystals grown in TaN crucibles was ~1ppm wt. Oxygen and carbon contamination of crystals was in the range of 500–1,200 ppm wt and 160–300 ppm wt, respectively. Results for oxygen contamination of crystals grown in BN crucibles (<500 ppm wt, i.e. < 6×10^{19} atoms/cm³) were comparable to values obtained from SIMS analysis of crystals grown under similar conditions (~ 1×10^{19} atoms/cm³).

Table 2.2. GDMS analysis of AlN powder sources and crystals (all values in ppm wt).¹⁰⁷

AlN source	B	Mg	Si	P	S	Ti	V	Cr	Mn	Fe	Zn
As-received	15	30	200	1.5	15	15	20	15	20	350	25
Sintered	2.5	< 0.1	200	< 0.1	< 0.1	1.7	1.5	< 0.1	0.13	1.7	< 0.1
Crucible											
BN	100	< 0.1	5.5	0.2	0.3	0.5	< 0.05	1.1	< 0.05	< 0.1	< 0.1
TaN	28	< 0.05	130	0.09	0.66	1.3	0.13	0.3	0.23	2.4	< 0.1

2.5.4 Optical characterization

The ability to grow large (~10 mm), high-quality AlN single crystals has allowed us to study not only the growth process, but the fundamental properties of AlN as well. Low-temperature partially polarized optical reflectance measurements were used to investigate the band-edge excitonic properties of crystals grown by PVT.⁶⁵ Fig. 2.8 (a) shows an image of an AlN crystal, grown in a TaN crucible, that exhibited a flat, naturally occurring *m*-face. The energies of the *A*, *B*, and *C* free excitons determined from fitting the reflectance spectra, Fig. 2.8 (b), were 6.025 eV, 6.243, and 6.257 eV, respectively. Using these exciton energies, the crystal-field splitting parameter of AlN was calculated, $\Delta_{cr} = -230$ meV. The exciton binding energy was estimated to be 71 meV using the effective masses computed by Kim *et al.*¹¹⁶ and a relative static dielectric constant of 8.0. This binding energy, together with the *A* exciton energy, yields a band gap energy for unstrained wurtzite AlN of about 6.096 eV at 1.7 K, close to a value of 6.12 eV estimated from PL measurements.⁶⁴

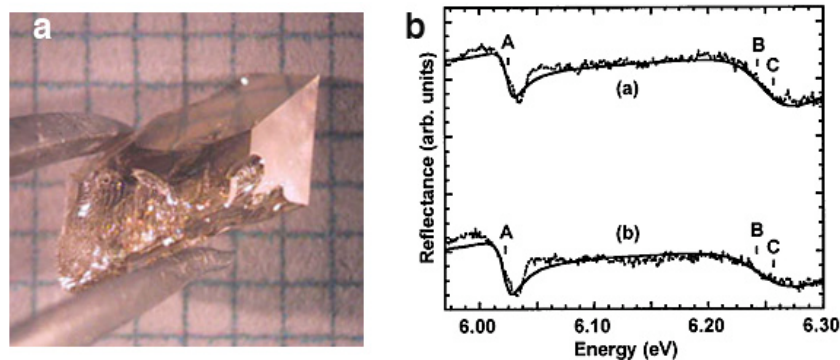


Figure 2.8. a) Optical photograph of an AlN crystal with a flat, naturally occurring *m*-face. b) Low-temperature partially polarized optical reflectance spectra from the *m*-face with (a) the *c* axis parallel to the spectrometer slits and (b) the *c* axis perpendicular to the slits (dotted lines). Solid lines are theoretical fits to spectra. The bottom of the graph is a different finite signal level in each case, to show the features more clearly.⁶⁵

2.6 Summary

PVT growth of AlN bulk crystals from an AlN powder source by spontaneous nucleation was studied using a dedicated, resistively heated reactor. AlN bulk crystals grown in BN crucibles exhibited highly anisotropic growth rates along different crystallographic directions. Crucibles made of refractory metals, and metal carbides or nitrides, yielded well-faceted crystals with isotropic growth rates. Depending on the choice of reaction crucible, crystals were optically clear or tinted orange. Deep orange coloration was routinely observed in crystals grown in refractory metal crucibles. Crystals of very high crystalline quality were obtained in all crucibles, as indicated by SWBXT and HRXRD. Thus, while crystal color, growth habit, and morphology were affected by the choice of crucible materials, the density of extended defects and their distribution in the crystals remained unaffected. Based on crucible lifetime, materials compatibility, and crystal quality the best results for AlN sublimation growth were obtained in crucibles made of TaN and TaC. Other refractory metal

(Nb, Hf) carbides and nitrides may offer similar performance. Finally, low-temperature partially polarized optical reflectance measurements were used to calculate the crystal-field splitting parameter of AlN, $\Delta_{cr} = -230$ meV, and a low-temperature band gap energy of 6.096 eV was obtained for unstrained wurtzite AlN.

3 Aluminum Nitride Crystal Growth II: Seeded Growth

3.1 Objectives

AlN bulk crystals grown by the sublimation-recondensation technique have been reported,^{117, 118} but presently, large AlN single crystals are still not available in large quantities. Seeded growth of AlN on SiC has been studied by a number of researchers^{105, 119, 120} as a way to exploit the availability of large, high-quality SiC substrates and to control the polarity and orientation of AlN crystals. In this chapter a process is described that was developed for deposition of thick AlN layers on SiC, and for reduction of cracks in the grown layers. The influence of SiC seed orientation on the polarity and morphology of the AlN layers will also be discussed. First, a brief introduction to the issues encountered in high-temperature growth of AlN on SiC substrates will be presented. This will be followed by a discussion of growth and characterization results obtained from bulk crystals grown on on-axis and off-axis (0001) substrates. A model describing the stress distributions in AlN/SiC heterostructures is developed and the implications of the model calculations for crystal growth will be discussed. Finally, an overview of extended defects observed in our samples will be given and the main results will be summarized.

3.2 Identification of issues in seeded growth on silicon carbide

The first successful seeded growth of AlN on SiC was reported by Balkas *et al.*,¹⁰⁵ who grew single-crystal platelets in SiC-coated graphite crucibles using a resistively heated graphite furnace operated at 1900–2250°C. SiC substrate degradation at the higher temperatures led to the formation of discontinuous grains of mixed AlN-SiC crystals. The

crucible coating was also unstable at high temperature. Cracking was always observed in as-grown crystals. Shi *et al.*^{103, 119} and Liu *et al.*^{121, 122} studied the nucleation and growth behavior of AlN grown by PVT on (0001) 6H-SiC substrates. Direct growth on bare Si-face SiC resulted in the formation of hexagonal subgrains in an island-like growth mode. No growth was observed on C-terminated bare substrates. On SiC substrates with an MOCVD AlN epilayer, however, AlN deposited in a two-dimensional growth mode without island formation. Stress-induced cracks were also observed in the crystals. The stress distribution in the crystals was quantified by energy shifts of the Raman $E_1(\text{TO})$ mode; AlN was under tensile stress (1 GPa) at the interface. A technique for reducing cracks in the AlN by first depositing an $(\text{AlN})_x(\text{SiC})_{1-x}$ alloy layer prior to sublimation growth of pure AlN was also reported; single-crystal platelets 4 x 6 mm and 0.5 mm thick were obtained. Epelbaum *et al.*¹²⁰ studied AlN crystal growth on SiC substrates of different orientations. Growth on Si-face *c*-oriented substrates was characterized by many hexagonal hillocks on the surface, while step-flow growth was obtained on *a*-plane substrates. As in previous work, cracks were observed in the AlN.

Based on these studies, a number of important issues that need to be addressed in establishing a reproducible seeded growth process can be identified:

- (i) materials compatibility and stability of crucibles and reactor components;
- (ii) source powder contamination, primarily from oxygen impurities;
- (iii) seed stability;
- (iv) growth mode of AlN on SiC, as influenced by substrate surface preparation and orientation;

- (v) cracking of the grown layers, understood to arise primarily from the difference in thermal expansion coefficients of the seed and crystal.

The first of these issues (i) was discussed in section 2.4 of the previous chapter. Results discussed below were obtained in sintered TaN and TaC crucibles, which had excellent high-temperature stability. No reactions were observed between the SiC seeds and crucibles made of these materials. With regard to (ii), high-purity sources of AlN are not commercially available, but as described in chapter 2, high-temperature sintering of the source powder prior to growth results in a significant reduction of impurities. Thus, this chapter will focus mainly on issues (iii), (iv), and (v).

3.3 On-axis (0001) silicon carbide substrates

3.3.1 Experiment

An AlN crystal growth process similar to the sandwich sublimation process for growth of SiC was employed in these studies. The vertical position of the crucible relative to the graphite heater was adjusted in order to control the temperature gradient between source and seed over a range of 1–3°C/mm. AlN was deposited on SiC seeds at temperatures between 1850° and 2000°C. Results reported below were obtained using both as-received and pre-sintered source powder. (0001) oriented, Si-face 6H-SiC substrates were obtained from commercial vendors. Two-inch substrates were cleaved into six pie-shaped, one-inch pieces that were used as seeds in cylindrical crucibles with a one-inch inner diameter. Bare substrates or substrates with a 200–400 nm AlN epilayer deposited by MOCVD were employed. The epilayer was intended to promote two-dimensional nucleation of AlN.¹¹⁹ Bare substrates were pre-treated¹²³ in 25% HF solution at room temperature for 3 min and rinsed

in deionized water prior to loading; substrates coated with an AlN epilayer received no additional pre-treatment.

3.3.2 Characterization techniques

Crystal morphology was studied by electron microscopy using a Hitachi S-3200 scanning electron microscope (SEM) operated at 5 kV accelerating voltage, and by optical microscopy. Crystalline quality and orientation were studied by SWBXT and HRXRD, as described in section 2.3.3. PFM measurements presented in section 3.6.4 were obtained with a TM Microscopes AutoProbe M5 equipped with conducting cantilevers (force constant 2.1 Nm^{-1}) and a dual-phase lock-in amplifier (SR 830). A 1000 \AA layer of 0.1 \Omega cm *p*-type diamond was deposited on the cantilever Si tips. An overview of PFM can be found in Appendix B.

3.3.3 Results and discussion

The morphology of AlN nucleated on bare on-axis substrates was characterized by hexagonal pyramids. During the early stages of growth, individual hexagonal nuclei were observed on the seed surface. With increasing growth time, these nuclei increased in size and coalesced, leading to the formation of hexagonal subgrains. In some cases, the layers were not fully coalesced and holes were observed in the AlN. In these uncoalesced samples, severe degradation of the SiC seeds was typically observed.

It was found that SiC seeds were highly sensitive to elevated growth temperature. Premature decomposition of the seed surface led to the formation of voids and holes in the AlN. The stability of the seeds was also dependent on the seed quality, in particular on the

micropipe density. Micropipes are micron-sized hollow cores that propagate along the *c*-axis in SiC. They have been described as hollow core superscrew dislocations.¹²⁴ In these studies, it was observed that thermal decomposition of SiC seeds proceeded most rapidly along micropipes. Two grades of SiC were employed, with micropipe densities less than 30 cm⁻² or from 50 to 100 cm⁻², in order to compare results obtained under equivalent process conditions with the two grades. Typically, micropipes in SiC were overgrown during the initial stages of AlN growth, but in some instances holes in the AlN were directly correlated with the presence of micropipes in the underlying seed (Fig. 3.1). As the growth temperature was increased, this effect became more pronounced, leading to the formation of discontinuous AlN grains as the growth temperature exceeded 1900°C. Below this temperature, seeds with lower micropipe densities were more stable, and AlN was deposited in a continuous layer.

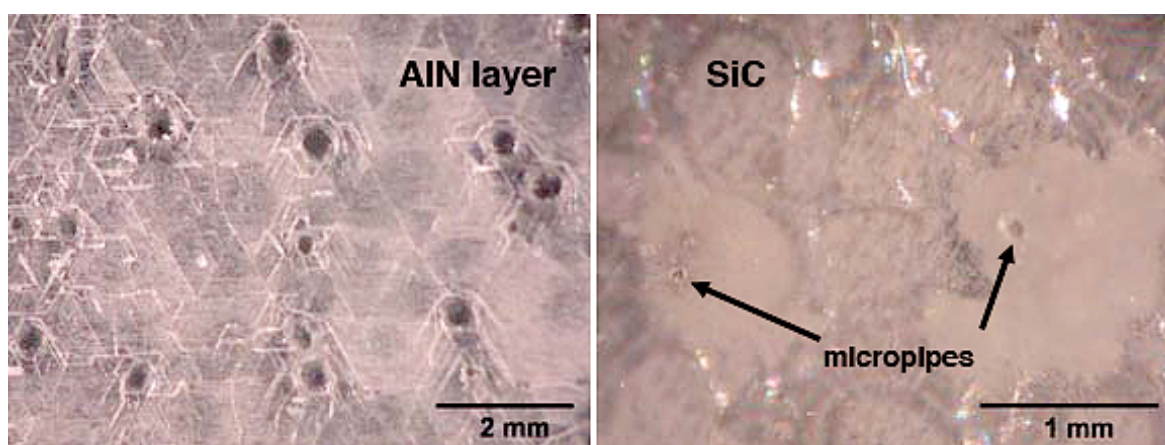


Figure 3.1. Optical photographs of holes in an AlN layer (left) and in the corresponding SiC seed (right) due to thermal decomposition along micropipes in the SiC.

Seed stability, on the one hand, limited the upper temperature at which favorable AlN growth could be performed, while the rapid decrease in AlN growth rate at lower temperatures, on the other hand, placed a lower bound on the useful growth temperature. Stable growth was achieved in the 1850–1900°C temperature range with growth rates from 10 to 30 $\mu\text{m/hr}$. However, as noted above, growth under these conditions produced crystals with rough morphologies characterized by hexagonal hillocks. High-resolution rocking curves of the (0002) reflection showed FWHM ranging from 456 to 1440 arcsec, indicating a tilt distribution in the grown layers probably caused by the formation of subgrain boundaries as the hexagonal hillocks coalesced. The growth mode of AlN deposited by sublimation on SiC has been studied by Liu *et al.*,¹²¹ who found that growth on bare on-axis or off-axis SiC seeds proceeded in an island mode promoted by screw dislocations. An AlN epilayer deposited on the seeds prior to sublimation growth was employed to change the growth mode to layer-by-layer growth. In our experiments on bare on-axis seeds, growth was also observed to proceed in a dislocation-mediated island mode. Growth on AlN-coated seeds, however, was two-dimensional, but could only be sustained for thinner layers, below approximately 300 μm . With increasing AlN thickness the surface morphology changed from smooth to rough. Hexagonal hillocks and growth spirals were observed, indicating growth was promoted by dislocations.

In addition, cracks were always observed in AlN layers less than 1 mm thick. In order to obtain large-area AlN single crystals by seeded growth, it is necessary to reduce cracking of the grown material. Cracks were likely caused by the differential thermal expansion between the seeds and grown layers, which resulted in a large tensile stress in the AlN at the

seed interface. The magnitude of this tensile stress is predicted to decrease with increasing AlN thickness (the reader is referred to section 3.5 for a discussion of stress distributions modeled in AlN/SiC heterostructures). Thus there exists a minimum thickness of AlN for which the thermal stress will not cause the grown layer to crack. As predicted, the density of cracks in crystals grown in this study decreased with increasing AlN thickness.

Seeded growth requires a delicate balance between the need to preserve the integrity of the SiC seeds and the need to deposit bulk AlN at sufficiently high growth rates to obtain thick layers within a reasonable amount of time. For this reason, a two-step growth process was developed, with the dual goals of minimizing seed decomposition during the initial stage of growth, and increasing the growth rate of AlN during the second stage. This process is shown schematically in Fig. 3.2. During the low-temperature stage, the goal is to deposit a fully coalesced AlN nucleation layer that can sustain subsequent growth. The temperature is selected such that decomposition of the seed surface is minimized. In order to increase the growth rate of AlN, the temperature is then slowly raised. Growth proceeds on the AlN nucleation layer despite the gradual decomposition of the SiC substrate. Elimination of the SiC substrate over the course of the growth is beneficial for the production of crack-free crystals, since the AlN is no longer strained during cool down by the thermal expansion mismatch with the seed.

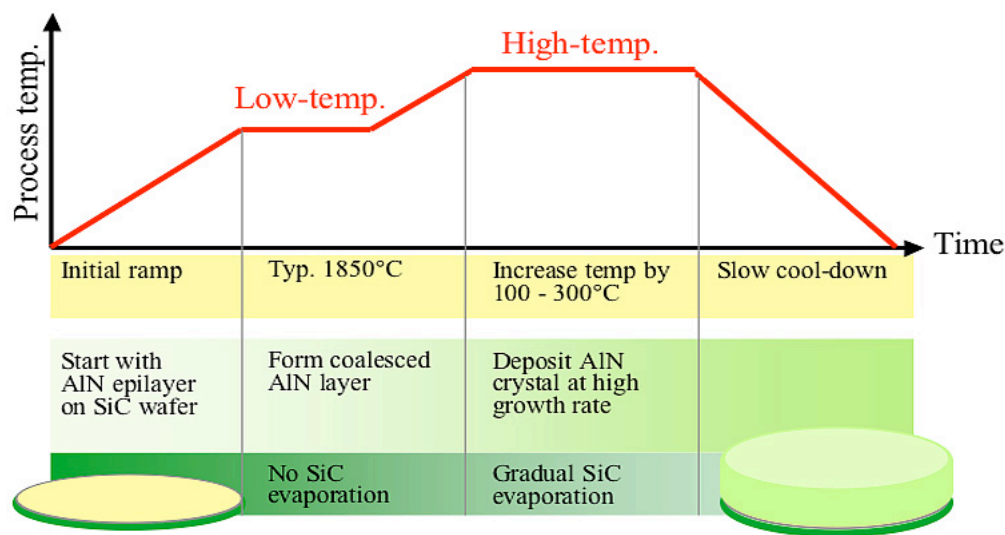


Figure 3.2. Schematic illustration of the two-step seeded growth process for production of crack-free AlN bulk crystals.

AlN layers ranging in thickness from 0.1 to 3 mm were grown via this two-step process on on-axis seeds coated with an MOCVD AlN epilayer.¹²⁵ During the first stage of growth, a coalesced layer of AlN was regularly deposited over the entire surface of the seed at a moderate temperature (typically < 1900°C), yielding growth rates between 10 and 30 $\mu\text{m/hr}$. After a sufficient amount of time to form a fully coalesced layer, the temperature was slowly raised 100–200°C, in order to deposit AlN at higher growth rates, approximately 70 $\mu\text{m/hr}$. As-grown surfaces were characterized by sharp hexagonal hillocks, similar to those observed by Epelbaum *et al.*¹²⁰ In samples where a fully coalesced layer was not deposited during the first growth stage, voids were observed in the AlN (Fig. 3.3). Cross sections taken from 2 mm thick samples indicated that voids were concentrated in the vicinity of the seed interface and that voids were typically overgrown by AlN after 1 mm of growth. Holes were observed in the AlN where overgrowth did not occur.



Figure 3.3. Photographs of a crack-free, polished AlN wafer. Wafer front (left) and back (right) sides are shown; note voids on the back side due to incomplete coalescence at the former substrate interface (mm scale).

Crack-free crystals were obtained from thicker layers (> 2 mm) by either partial or complete evaporation of the SiC seed during the high-temperature growth (Fig. 3.4). These crystals were used to prepare polished wafers (Fig. 3.5 (a)) with ~ 1 nm RMS roughness as determined by atomic force microscopy. HRXRD of wafers showed tilt widths (Fig. 3.5 (b)) on the order of 8 arcmin. The narrow TCRC widths observed in RSMs (Fig. 3.5 (c)) indicated low impurity incorporation during the seeded growth. GDMS results shown below in Table 3.1 confirmed that crystals grown by this method contained at most 300 ppm wt C and 130 ppm wt Si, values comparable to those found in the sintered AlN source powder, indicating negligible incorporation of C and Si during growth.

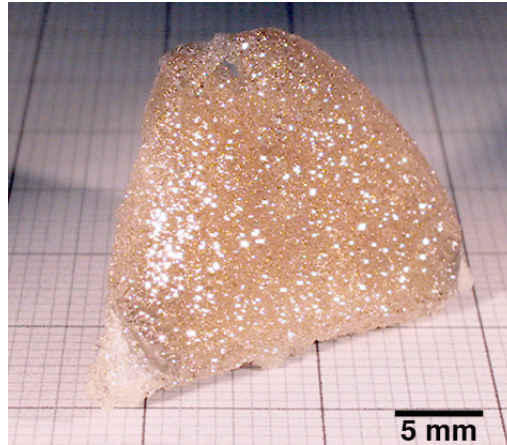


Figure 3.4. Photograph of a 2.5 mm thick AlN crystal grown on on-axis 6H-SiC. During high-temperature growth the seed almost completely evaporated. No cracks were observed in the AlN.¹²⁵

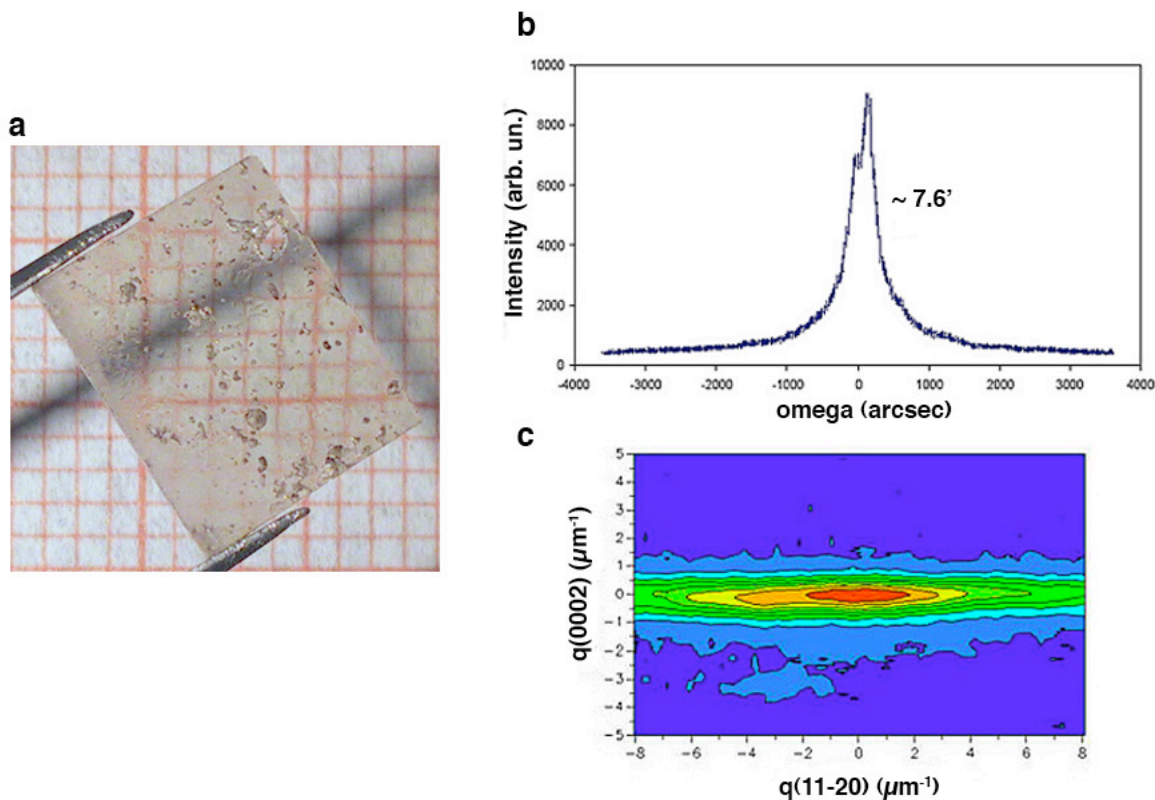


Figure 3.5. Structural characterization of an AlN wafer. a) Optical photograph of AlN wafer, 9 x 11 mm, 500 μm thick, prepared from bulk AlN grown on on-axis 6H-SiC (mm grid). Dark spots are from incomplete polishing on the wafer back side.¹²⁵ b) Double crystal (0002) rocking curve showing a tilt width of 7.6 arcmin. c) (0002) RSM showing a TCRC width (10.6 arcsec) comparable to the perfect crystal width of 8 arcsec, indicating low impurity incorporation during seeded growth.

Table 3.1 GDMS analysis of AlN source powder and an AlN wafer grown on a SiC seed (all values ppm wt).

Sample	Boron	Carbon	Oxygen	Silicon
As-received source powder	15	~ 3000	~ 1000	200
Sintered source powder	2.5	≤ 200	≤ 300	200
AlN wafer (TaN crucible, as-received source powder)	28	≤ 160	≤ 1200	130

3.4 Off-axis (0001) silicon carbide substrates

Since SiC seed stability during the early stages of growth was critical to the formation of a fully coalesced AlN layer capable of sustaining further growth, seeded growth on off-axis SiC seeds was investigated as a means to enhance the lateral growth of the initial AlN layer.

3.4.1 Experiment

In order to investigate the influence of substrate orientation on the growth and morphology of AlN, experiments were performed on 4° off-axis (0001) oriented, Si-face 6H-SiC, and 8° off-axis (0001) oriented, Si-face 4H-SiC substrates. Bare substrates were pre-treated in 25% HF solution at room temperature for 3 min and rinsed in de-ionized water prior to loading. In the results reported below, the SiC seed was not evaporated from the AlN. Crystal morphology was observed by optical microscopy and SEM. The grown layers were characterized by SWBXT and HRXRD.

3.4.2 Results and discussion

AlN grown on bare off-axis seeds exhibited two distinct morphologies: flat regions with ~100 μm-wide terraces characteristic of step-flow growth (Fig. 3.6), and rough regions containing large, millimeter-wide hexagonal hillocks. Growth steps were observed aligned perpendicular to the off-axis direction, indicating that steps flowed in the direction defined by the substrate misorientation. Step bunching was observed in all samples, becoming more pronounced with increasing layer thickness. The AlN exhibited a sharp interface with the SiC seeds and voids were not observed in the grown layers. Parallel cracks were observed

running along the offcut direction. In addition to these vertical cracks, delamination of the AlN layers was sometimes observed.

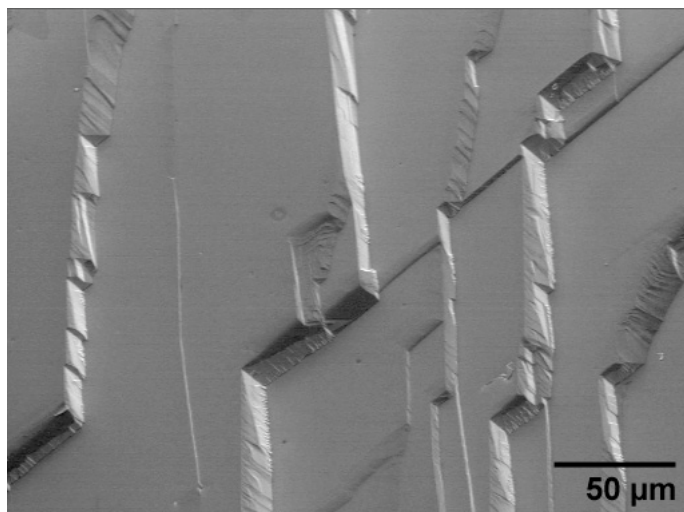


Figure 3.6. SEM image of an 800 μm thick AlN layer, grown on 8° off-axis SiC, exhibiting step-flow growth.

The observed step-flow growth mode was a consequence of the vicinal seed surface employed in these experiments. Steps enhancing adatom incorporation were provided by the offcut surface, as opposed to the growth observed on on-axis seeds, where steps were provided by spiral growth around screw dislocations. A similar difference (straight steps vs. spiral growth hillocks) in the morphology of AlN thin films grown on vicinal and nominally flat surfaces of (0001) SiC by plasma assisted molecular beam epitaxy has been reported.¹²⁶ In contrast to previous reports,¹²¹ step-flow growth of bulk AlN was achieved on bare vicinal substrates without the use of an MOCVD epilayer. However, growth instabilities were observed in some experiments where hexagonal hillocks characteristic of dislocation-mediated growth were formed in the grown layers.

HRXRD and SWBXT were used to characterize representative samples.¹²⁷

Topographs of layers with the seed attached were deformed with respect to the original crystal shape due to bending of the lattice planes under strain (Fig. 3.7 (b)). However, topographs of delaminated AlN crystals showed relatively strain free crystals with a nearly uniform density of defects. Typically, defect densities were above the threshold (10^6 cm^{-2}) for individual visualization in the topographs. TCRC widths varied widely, from 17.84 to 230 arcsec, indicating some crystals with relatively high purity were obtained, while other samples contained a substantial amount of defects. RSMs indicated that AlN layers were tilted with respect to the SiC seeds, as shown in Fig. 3.7 (c). A similar tilting has been observed in GaN epitaxial layers grown on vicinal surfaces of sapphire,¹²⁸ and was first reported by Nagai¹²⁹ in $\text{Ga}_x\text{In}_{1-x}\text{As}$ grown on GaAs. The reason for this tilting is the large film-substrate lattice mismatch along the c -direction. Lattices grown on adjacent surface terraces have a height difference $\Delta c = c_f - c_s$, where c_f and c_s refer to the film and substrate bilayer thicknesses, respectively. This gives rise to a tilt angle α of the epilayer, where $\tan \alpha = -(\Delta c/l)$ with l the average step spacing. The step spacing is related to the substrate offcut angle φ by $\tan \varphi = (c_s/l)$. The Nagai equation relates the epilayer tilting angle with the height difference and offcut angle:

$$(15) \quad \tan \alpha = -\left(\frac{\Delta c}{c_s}\right) \tan \varphi.$$

The epilayer lattice in the immediate vicinity of the substrate surface is deformed to accommodate this tilt, but further away the lattice tends to be homogeneous, which leads to a permanent tilting of the entire epilayer. Studies have shown that the Nagai tilting rule is strictly obeyed in GaN grown on vicinal 6H-SiC. However, the tilt predicted by the Nagai

equation for AlN ($c_f = 0.249$ nm) grown on 8° off-axis 4H-SiC ($c_s = 0.251$ nm) substrates, ~ 230 arcsec, is significantly larger than the tilt observed in the RSM, Fig. 3.7 (c). Further characterization of this tilt requires recording TCRCs in asymmetrical diffraction geometries, which is the subject of ongoing work.

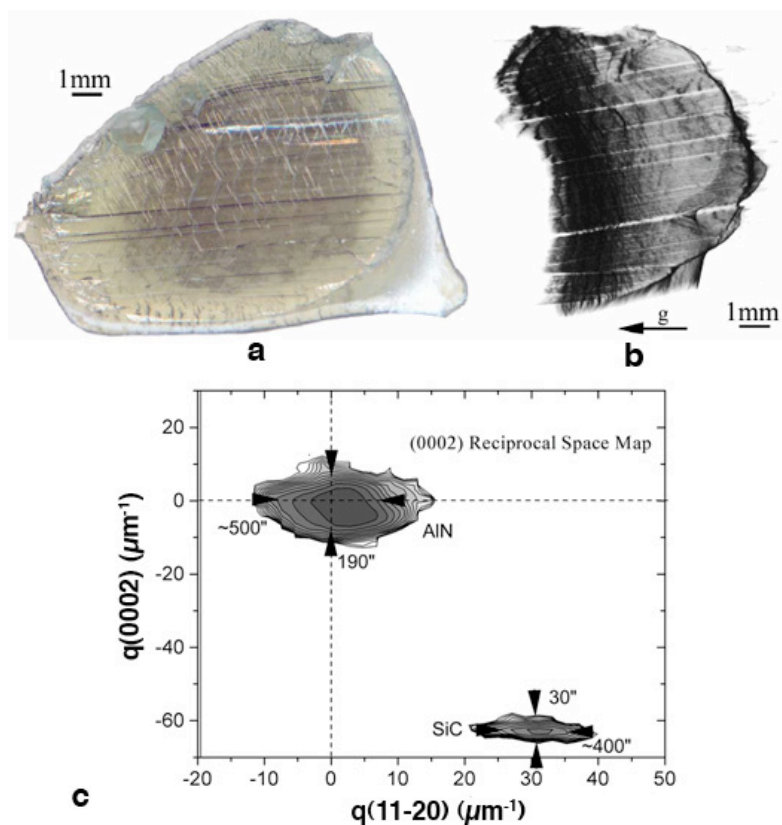


Figure 3.7. Structural characterization of AlN grown on 8° off-axis 4H-SiC. a) Optical photograph showing steps on the surface and parallel cracks running along the [1-210] direction. b) Transmission x-ray topograph ($g= 1-210$) exhibiting distortion caused by residual strains. c) (0002) RSM showing the tilt (1620 arcsec) and lattice plane spacing difference (1.63%) between the AlN and SiC layers. The TCRC width of AlN is 190 arcsec and the tilt width is ~ 500 arcsec.¹²⁷

3.5 Analysis of stress in aluminum nitride-silicon carbide bilayer structures

3.5.1 Objectives

The large thermal expansion difference between AlN and SiC causes AlN layers grown on SiC substrates to crack during cool down from growth to room temperature. A simplified one-dimensional model based on an extension of bilayer beam theory was analyzed in order to compute stress distributions in AlN/SiC heterostructures and to predict trends in the cracking behavior of AlN bulk layers. The model predictions were used to devise growth strategies to suppress cracks in the AlN layers.

3.5.2 Model formulation

In its most general formulation the model provides a description of the stress distribution in a composite plate consisting of layers with different elastic and thermal properties. Such a configuration is commonly achieved during deposition of thin film heterostructures on a substrate. Due to differences in material properties, such as lattice parameter and thermal expansion coefficient, elastic strains exist between the layers. For example, when the composite structure is subjected to changes in temperature, such as on cooling from the growth temperature, the differences in thermal expansion coefficients of the layers lead to different thermal strains within the structure. Since the layers are constrained at the various interfaces, elastic strains are generated in the layers. As a result of the elastic strains, a stress σ_i will be set up in each layer and the composite will bend in response to the stresses, assuming a radius of curvature R .¹³⁰ At equilibrium the structure must satisfy the requirements of no net end forces or bending moments applied to the layers.¹³¹

Early formulations of the problem of computing the stress in a thin film deposited on a beam were provided by Stoney¹³² and Timoshenko.¹³³ The (modified) Stoney equation is still used to calculate the stress in the film from the bending of the beam:

$$(16) \quad \sigma_f = \frac{E t_s^2}{6R t_f},$$

where E is the modulus of elasticity of the substrate, t_s and t_f are the substrate and film thicknesses (t_f assumed $\ll t_s$), and R is the radius of curvature of the substrate. Note that in this formulation the bending is uniaxial. The classic expression for R was first derived by Timoshenko, whose analytical approach has been used by a number of authors in extending the formulation to biaxial stress distributions¹³⁴ and multiple layers.¹³⁵

Consider a general composite beam structure containing N layers with elastic (Young's) moduli E_i , thicknesses t_i , length L , and width W . The length of the beam is taken to be sufficiently greater than the width so that curvature in the transverse direction is negligible¹³⁵ and the solution is one-dimensional. We solve for the stress distributions $\sigma_i(z)$ in the layers in terms of the forces F_i , moments M_i , and strains ε_{ij} which exist in the composite. By convention, tensile forces and stresses are taken to be positive. Assuming coherency is maintained between the layers, the strains must match at the various interfaces. The conditions of no net end forces or bending moments applied to the layers, together with the equations for the interfacial strains, yield the following set of coupled equations:^{130, 136}

$$(17) \quad \sum_{i=1}^N F_i = 0,$$

$$(18) \quad \sum_{i=1}^N \left[\frac{E_i t_i^3 W}{12R} + F_i \sum_{j=1}^i \left(t_j - \frac{1}{2} t_i \right) \right] = 0,$$

$$(19) \quad \sum_{i=1}^{N-1} \left[(\varepsilon_i - \varepsilon_{i+1}) = \frac{F_{i+1}}{E_{i+1} w t_{i+1}} - \frac{F_i}{E_i w t_i} - \frac{1}{2R} (t_i + t_{i+1}) \right].$$

In the case where only the strains due to thermal expansion differences are considered, the thermal strain ε_i in the layers is given by

$$(20) \quad \varepsilon_i = \left(\frac{a - a_0}{a} \right)_i = \int_T^{T_0} \alpha_i dT,$$

where the in-plane lattice parameter of layer i at growth temperature T is a and at room temperature T_0 is a_0 , and the temperature-dependent thermal expansion coefficient of the layer is α_i . The thermal strain can be approximated using an average thermal expansion coefficient $\bar{\alpha}_i$ for the temperature range $\Delta T = T_0 - T$, in which case equation (6) becomes

$$(21) \quad \varepsilon_i \approx \bar{\alpha}_i \Delta T.$$

Equations (17) – (19) give a closed-form solution for R and the F_i . The stress distribution in any layer is given by the sum of the stress $F_i/t_i w$ due to the (compressive or tensile) force and the stress $E_i(z-t_i/2)/R$ due to bending¹³⁷

$$(22) \quad \sigma_i^{1D}(z) = \frac{F_i}{t_i w} + \frac{E_i \left(z - \frac{t_i}{2} \right)}{R},$$

where the positive direction for z , the position in the i^{th} layer measured from the top of the i^{th} layer, is indicated in Fig. 3.8 for a two-layer ($N = 2$) model structure consisting of AlN ($i = 1$) grown on SiC ($i = 2$). Note that the sign of the stress may change over the thickness of a given layer.

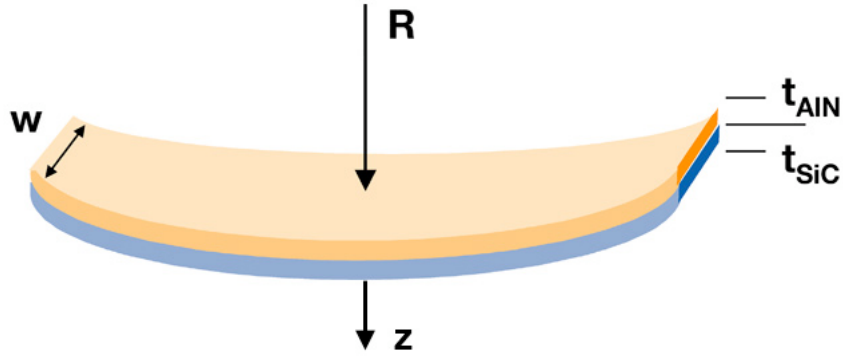


Figure 3.8. Schematic diagram of the $N=2$ model structure, consisting of an AlN ($i = 1$) layer grown on a SiC ($i = 2$) substrate. The structure is concave on the AlN film side at room temperature. The beam width W , radius of curvature R , layer thickness t_i , and positive z -direction are indicated.

Wurtzite films grown on (0001)-oriented hexagonal substrates have uniform biaxial strain in the c -plane and strain tensor components $\epsilon_{12} = \epsilon_{23} = \epsilon_{31} = 0$, $\epsilon_{11} = \epsilon_{22} \neq 0$, and $\epsilon_{33} \neq 0$, which describe a uniform compression/expansion in the c -plane and a reverse deformation along the c -axis. The principal strains are given in terms of the lattice constants along the a - and c -directions

$$(23) \quad \epsilon_{11} = \frac{(a - a_0)}{a_0}, \quad \epsilon_{33} = \frac{(c - c_0)}{c_0},$$

where a_0 and c_0 are the strain-free values. In the approximation of isotropic elastic theory, the principal strains are related to the principal stresses by Hooke's law:

$$(24) \quad \epsilon_{11} = \frac{[\sigma_{11} - \nu(\sigma_{22} + \sigma_{33})]}{E}, \quad \epsilon_{33} = \frac{[\sigma_{33} - \nu(\sigma_{11} + \sigma_{22})]}{E},$$

where ν is Poisson's ratio. For biaxial stress in the c -plane, $\sigma_{11} = \sigma_{22} \neq 0$ for the in-plane stress, and $\sigma_{33} = 0$ for the normal stress. This gives

$$(25) \quad \varepsilon_{11} = \frac{(1-\nu)\sigma_{11}}{E}, \quad \varepsilon_{33} = \frac{-2\nu\sigma_{11}}{E}, \quad \frac{\varepsilon_{33}}{\varepsilon_{11}} = \frac{-2\nu}{(1-\nu)},$$

for the relations between stress and strain. The first of these relations, between the principal stress and strain in the c -plane, allows one to define a modified elastic modulus $E' = E/(1-\nu)$ for the case of biaxial stress. Thus, if the dimensions of the beam in our model are comparable ($L \approx W$) and spherical bending is assumed, then the stress distribution calculated in a composite beam can be modified to obtain the biaxial stress (2D) in a composite plate¹³⁰ by using the one-dimensional (1D) solution, such that

$$(26) \quad \sigma_i^{2D}(z) = \frac{\sigma_i^{1D}(z)}{(1-\nu)}.$$

For the model structure (Fig. 3.8) consisting of AlN grown on SiC, $N=2$ and equations (17) – (19) reduce to

$$(27) \quad F_{AIN} + F_{SiC} = 0,$$

$$(28) \quad \frac{E_{AIN} t_{AIN}^3 w}{12R} + \frac{E_{SiC} t_{SiC}^3 w}{12R} + \frac{t_{AIN}(F_{SiC} - F_{AIN})}{4} = 0,$$

$$(29) \quad \varepsilon_{AIN} - \varepsilon_{SiC} = \frac{F_{SiC}}{E_{SiC} t_{SiC} w} - \frac{F_{AIN}}{E_{AIN} t_{SiC} w} - \frac{(t_{AIN} + t_{SiC})}{2R}.$$

This set of equations is readily solved for F_{AIN} , F_{SiC} , and R . The thermal contraction of AlN over the range from growth temperature to room temperature is greater than that of SiC, and the heterostructure bends to be concave on the AlN film side at room temperature. The AlN is under tension at the substrate interface. When the tensile stress exceeds a critical stress σ_c , cracking occurs. The AlN uniaxial interfacial stress is given by substituting $z = t_{AIN}$ into equation (22):

$$(30) \quad \sigma_{AIN}^{1D} = \frac{F_{AIN}}{t_{AIN} w} + \frac{E_{AIN} t_{AIN}}{2R}.$$

Using equation (26) and a value for Poisson's ratio of $\nu = 0.239$ for AlN,⁵¹ it is seen that the calculated value of the 2D stress is larger than the 1D stress by ~30%.

The stress at fracture σ_c , also called the modulus of rupture or fracture strength, of pure AlN single crystals has not been reported in the literature. However, measurements⁹ on hot pressed AlN polycrystalline ceramics yielded a room temperature value of ~266 MPa, which was used in this work. The values of the isotropic elastic constants and average thermal expansion coefficients of AlN and SiC were taken from Wang and Reeber.⁵¹ In addition, the temperature dependence of the elastic modulus was neglected; calculations¹³⁸ have shown only a small variation with temperature. The assumption of isotropic elasticity restricts the validity of the model, but the isotropic elastic constants have been determined with lesser uncertainty than the elastic stiffness constants, whose published values vary greatly.

3.5.3 Results and discussion

The model formulation considers only the internal extrinsic stress due to thermal expansion differences and ignores intrinsic stress (e.g. misfit stress). It is assumed that the misfit stress is relaxed during the growth of such thick layers by the formation of misfit dislocations. The results of the 1D model calculations are shown in Fig. 3.8. The AlN interfacial stress for cool down from a growth temperature of 1875°C and a SiC seed thickness of 420 μm is shown in Fig. 3.9 (a) as a function of AlN layer thickness. A layer thickness of 4.7 mm corresponds to the critical cracking stress of 266 MPa assumed in the

model. The model predicts that for these growth conditions, AlN grown on SiC should be at least 4.7 mm thick to avoid cracking due to thermal stress. These results are not qualitatively changed by investigating the temperature dependence of the stress distribution; for a higher ΔT , the distribution shifts upwards and vice-versa, but the overall shape is unchanged. Obviously, the corresponding 2D stress distribution, which has stress values that are ~30% higher, would place the AlN critical thickness at a higher value. Thus, the 1D distribution was deemed sufficient for a conservative estimate of the critical thickness. Conversely, the stress distribution corresponding to an experimentally accessible AlN layer thickness of 1 mm was calculated for the same temperature range as a function of SiC seed thickness in Fig. 3.9 (b). In this case, the SiC seed would have to be a maximum of 89 μm thick to avoid cracking the 1 mm AlN layer. This thickness is far below that of any commercially available SiC substrates.

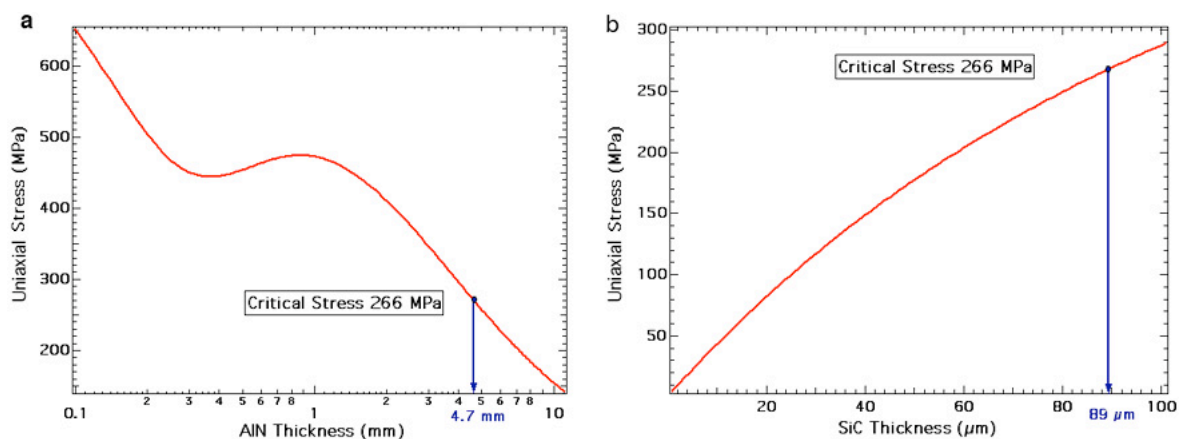


Figure 3.9. The dependence of the AIN uniaxial tensile stress at the interface of the AIN-SiC layers on a) AIN thickness for a growth temperature of 1875°C, and SiC substrate thickness of 420 μm ; and b) on SiC thickness for a growth temperature of 1875°C, and AIN layer thickness of 1 mm. Respective thicknesses corresponding to an assumed cracking strength of 266 MPa are indicated.

Clearly, if commercially available seeds are used, maintaining stable growth conditions for the lengths of time required to deposit such thick AIN layers is a challenging technical task. However, as the experimental results presented in section 3.3.3 indicate, the use of a two-step growth process allows the AIN growth temperature to be raised above the dissociation temperature of SiC. This has two beneficial effects: (i) the growth rate of AIN is increased; and (ii) the SiC seed is slowly evaporated. Thus the principal cause of cracking considered here, namely the thermal stress from the seed, can be eliminated directly. Crack-free AIN layers 2–3 mm thick were grown via the two-step process with either partial or complete evaporation of the seed.

3.5.4 Summary

A simplified one-dimensional model was used to analyze stress distributions in AlN/SiC heterostructures. By comparing the calculated tensile stress in AlN at the substrate interface with experimental values of the fracture strength of AlN ceramics, an estimate was obtained for the minimum thickness of the AlN layer required on commercial SiC substrates in order to avoid cracks generated by thermal strain. A direct implication of this estimate for crystal growth is illustrated by the experimental results presented in section 3.3.3; in order to grow crack-free AlN layers within a reasonable amount of time, this source of cracks may be eliminated directly, namely by *in situ* evaporation of the SiC substrate from the grown AlN layer prior to cool down.

3.6 Extended defects in aluminum nitride grown on silicon carbide

3.6.1 Overview

Heteroepitaxial growth of AlN on SiC seeds results in the formation of defects in the grown layers. Several extended defects, such as voids, cracks, and inversion domains, have been observed in high-temperature PVT grown samples obtained in this study. These will be discussed below.

3.6.2 Voids

Voids were observed in the AlN as a result of thermal decomposition of the SiC seeds. SiC crystal growth by sublimation of SiC powder is performed at higher temperatures and lower ambient pressures than AlN growth. This high thermal stability, along with a similar crystal structure as AlN and low lattice mismatch to it, would seem to make SiC an

excellent choice for a seed. However, the presence of highly reactive Al vapor during PVT of AlN probably contributes to the lower decomposition temperature of SiC. It has been noted¹²⁰ that there exists a large difference in the equilibrium vapor pressures of the quaternary Al-N-Si-C system and the corresponding binary Al-N and Si-C systems. Thermal degradation of seeds has been observed by a number of investigators,^{105, 119, 120} but the reported temperatures at which this effect becomes detrimental to the AlN growth process vary and are probably dependent on a number of factors. In our studies this temperature was identified as roughly 1900°C. Above this temperature, coalescence of the AlN layer during the early stages of growth was difficult to achieve, resulting in the formation of voids at the interface. When voids were not overgrown at a later stage of growth, holes were observed in the AlN layers.

3.6.3 Cracks

Generally, the mechanical properties of bulk crystalline solids can be explained using dislocation theory. For example, yield strengths are influenced by various processes governing generation and motion of dislocations. In the case of stressed films, time-dependent processes for stress/strain relaxation may involve dislocation generation, thermally activated motion of atoms and defects, and film/substrate fracture. A well-known example is the mechanical relaxation of misfit strain in epitaxial films by generation of misfit dislocations. In general, the dominant relaxation mechanism is the one with the highest strain relaxation rate. Thus, in ductile materials glide and climb of dislocations occur in different stress-temperature regimes. However, in brittle materials cracking or fracture of the film, substrate, or film-substrate interface is commonly encountered.

The Griffith theory¹³⁹ of fracture mechanics proposes that the process of crack growth releases elastic strain energy. Preexisting cracks or flaws in a material can grow under the action of an applied or internal tensile stress that is perpendicular to the crack axis. A criterion for mechanical stability of cracks is expressed in terms of the fracture toughness, which is relatively low in brittle materials and reflects a low resistance to fracture. Thouless¹⁴⁰ has pointed out a number of similarities between the processes of crack growth and dislocation propagation in thin films: (i) film strain energy is relaxed at the cost of introducing a defect; (ii) an elastic singularity (crack tip or dislocation line) is formed at the film-substrate interface; and (iii) similar energy balance methods can be used to derive an expression for the equilibrium condition governing propagation of each defect. In the case of cracking, the strain energy relaxed by crack growth is balanced by the energy associated with the formation of new crack surfaces (i.e. surface energy).

AlN grown on on-axis SiC contained cracks propagating in all $\langle 11-20 \rangle$ directions, i.e. on $\{10-10\}$ planes, which are low surface energy planes. Defects such as cracks, edge chips, scratches, and pits in the SiC seeds acted as possible crack nucleation sites. In some cases AlN crystals were also delaminated from the SiC seed. These delaminated crystals typically contained a thin SiC layer on the back side, so it appears these cracks originated in the SiC. This feature has also been observed by Epelbaum *et al.*¹²⁰ Since crack-free AlN crystals were grown when the SiC was evaporated prior to cool down, it is assumed that cracking was primarily due to thermal strain, while misfit strain was either partially or completely relaxed at the growth temperature by the formation of misfit dislocations. In contrast to cracks observed in layers grown on on-axis seeds, cracks in AlN grown on vicinal

surfaces were typically parallel, running along the off-axis direction, parallel to the (10-10) plane. X-ray topographs of these crystals appeared distorted with respect to the original sample shape and size (Fig. 3.6), indicating residual strains responsible for the bending of the lattice planes were present in the grown layers. This implies that vertical cracks did not relax the strain in the AlN layers completely. However, topographs of delaminated AlN crystals appeared relatively strain free, indicating the strain was relaxed by removing the substrate.

3.6.4 Inversion domains

Previous reports indicated that AlN grown on Si-face SiC should grow with the Al-polar face.⁴³ The polarity of AlN can be determined by wet etching since the Al-face is more stable than the N-face in either phosphoric acid or potassium hydroxide solutions.^{43, 44} Crystals grown on both on-axis and off-axis seeds were etched in aqueous solutions of phosphoric acid (8M) or potassium hydroxide (6M) at 60°C for 5–30 min in order to determine their polarity. The as-grown (0001) surfaces of crystals grown on off-axis seeds showed no etching for any of the etch times or solutions studied. Furthermore, crystals that were removed from the off-axis SiC seeds, either by delaminating them or by grinding off the seed, were evenly etched on the side facing the seeds. By contrast to these samples grown on off-axis seeds, polished wafers prepared from thick AlN layers grown on on-axis (0001) SiC seeds contained 50–200 μm -wide regions of etched hexagonal hillocks. One such region, confined within a smooth surface, is shown in Fig. 3.10 (b). No etching was observed on the as-grown (0001) surfaces of AlN deposited on off-axis seeds, which are thus identified as Al-polar surfaces. Since etching was observed on the side of the crystals facing the seed, this is identified as the N-polar face. These observations are consistent with the expected orientation

of AlN grown on Si-face SiC. The etching results observed in Fig. 3.10 (b), however, are consistent with the presence of N-polar IDs in a smooth Al-polar surface. Thus, AlN grown on on-axis SiC remained primarily Al-polar, but contained N-polar IDs up to 200 μm in width. Observation of the opposite face of these crystals (i.e. the side facing the SiC seed) revealed an etched N-polar surface, which contained corresponding, smooth Al-polar regions, thus indicating that these IDs typically propagated through the entire crystal (Fig. 3.10 (a)). However, the surface area covered by N-polar regions on the top face was smaller than the extent of Al-polar areas observed on the side facing the seed; it appears that some of the IDs may have been overgrown by Al-polar material.

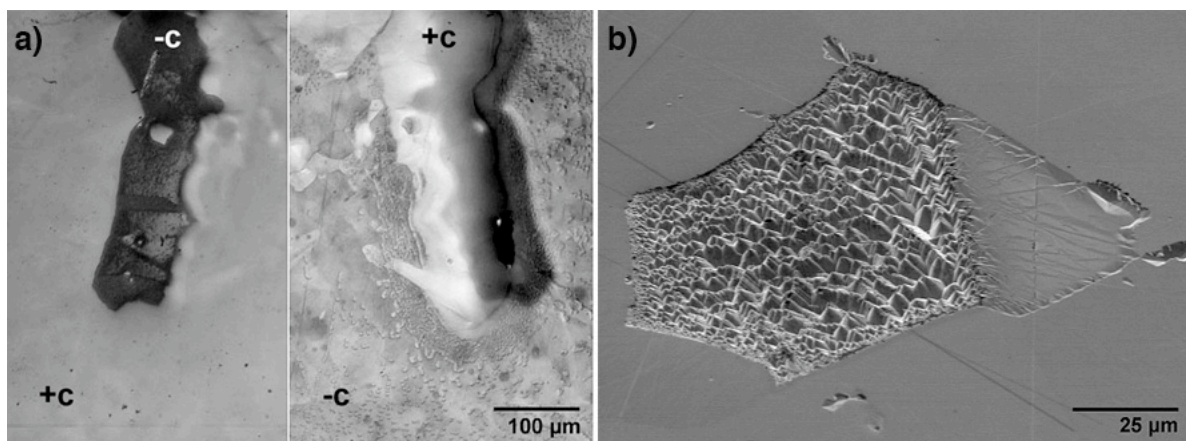


Figure 3.10. Etch features observed on AlN {0001} polar surfaces. a) Optical microscopy images of opposite c -faces of a polished AlN crystal grown on on-axis SiC and etched in H_3PO_4 solution. An ID propagates through the entire crystal. b) SEM image of a N-polar ID on an Al-polar surface revealed by etching in KOH solution at 60°C for 10 min. Etched hexagonal hillocks are confined in the Al-polar smooth surface.

The location of these IDs typically coincided with the presence of underlying voids at the interface with the SiC, which were subsequently overgrown by AlN. However, the nucleation mechanism of these IDs is still unclear. They may be formed in the MOCVD AlN layer itself and then propagate into the subsequently deposited PVT layer. This would account for their being observed only in layers grown on on-axis seeds with an AlN epilayer, but has not been confirmed. A model^{37,38} for the inversion domain boundary structure has been formulated and verified for IDs observed in sintered ceramics, where an increase in the oxygen concentration of the AlN lattice beyond a critical value (~5850 ppm wt) results in a stabilized domain boundary consisting of Al atoms octahedrally bonded to oxygen atoms. However, oxygen impurities in our AlN crystals measured by GDMS are at levels (~500-1200 ppm wt) significantly below the critical value in this model. Brown *et al.*¹⁴¹ identified the nucleation source of Al-polar IDs observed in homoepitaxial GaN grown by MOCVD on N-polar bulk GaN substrates as an amorphous layer observed at the film-substrate interface. Electron energy loss spectroscopy (EELS) identified the presence of oxygen in the amorphous layer, which was presumed to be due to gallium hydroxide formed as a reaction product of the KOH etching used to prepare the substrates prior to epitaxy. Other investigators^{142, 143} have reported the influence of surface treatment on the polarity of GaN films grown by MOCVD on sapphire substrates. If substrate surface preparation is responsible for the IDs observed in our samples, it may be due to incomplete removal of the substrate surface oxide, either by *ex situ* HF cleaning or *in situ* desorption during the ramp to growth temperature. It is also possible that when voids are formed at the AlN/SiC interface, the AlN overgrown at a later stage does not replicate the polarity of the substrate. This may explain why IDs were not

observed in AlN grown on off-axis seeds; these interfaces were typically continuous, due to enhanced lateral growth from step flow.

In order to confirm the presence of IDs inferred from the etching results, polished *c*-oriented crystals were imaged by PFM. Fig. 3.11 (a) shows an optical microscopy image of a polished feature that exhibited an etching response similar to Fig. 3.10 (b). The edge contrast is due to the difference in height between the polished surfaces of opposite polarity. It was observed that N-polar regions were polished more deeply than the surrounding Al-polar material, which is a reflection of the greater instability of the N-face. This surface relief is confirmed in the PFM topography image (Fig. 3.11 (b)). The fact that the observed features are indeed IDs is unambiguously demonstrated in the PFM phase image (Fig. 3.11 (d)). Regions of different polarity exhibit opposite contrast, and the N-polar region identified by etching is brighter, as expected.

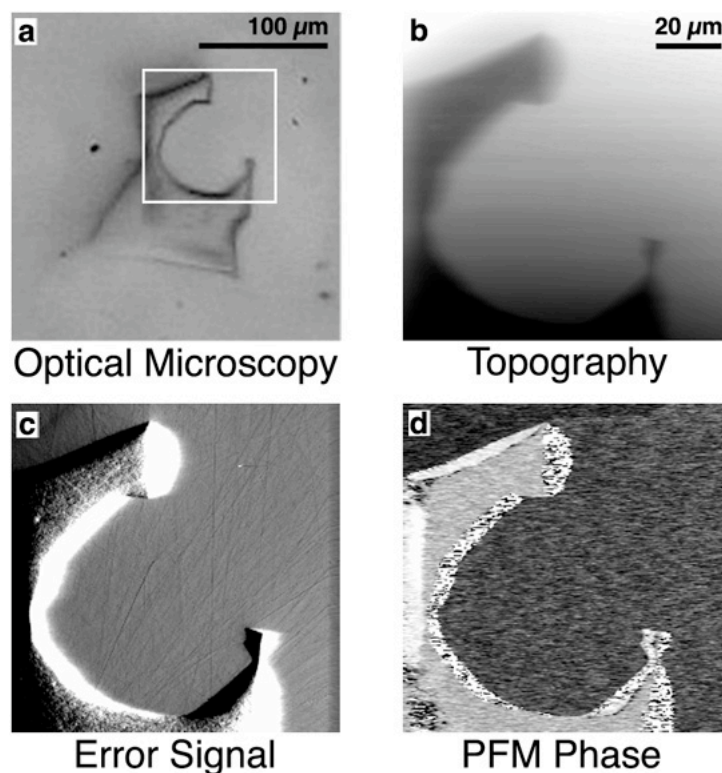


Figure 3.11. PFM analysis of AlN (0001) surface. a) Optical microscopy image of a N-polar ID on an Al-polar AlN surface after polishing. b) PFM topography image indicating surface relief (vertical scale: 800 nm). c) PFM error signal (vertical scale: 60 nm). Surface scratches are visible in the polished Al-polar surface (~2 nm RMS roughness). d) PFM phase image indicating opposite contrast between N-polar (brighter) and Al-polar regions.

3.6.5 Summary

Due to the high temperatures involved in the PVT process and the reactivity of Al vapor, stability of the SiC seeds was crucial for obtaining continuous AlN seeded layers. Cracks were observed in the AlN due to the large thermal stress generated during cool down from the growth temperature. The presence of inversion domains in bulk AlN grown on on-

axis SiC, first deduced by observation of etching effects on opposite basal planes, was confirmed by PFM. Possible sources for these IDs were discussed.

3.7 Summary

Seeded growth of AlN bulk crystals on SiC seeds by PVT from an AlN powder source was investigated. In order to establish a reproducible seeded growth process, several growth strategies were devised to overcome challenges related to the stability of the SiC seeds, the formation of cracks in the grown layers, and the formation of IDs. First, the stability of the SiC seeds was highly sensitive to temperature. Growth above 1900°C resulted in decomposition of the SiC and incomplete coalescence of the initial AlN nucleation layer. Seed decomposition was observed to proceed most rapidly along micropipes in SiC. The subsequent growth behavior depended strongly on the formation of a coalesced AlN layer. Voids and holes were observed in the AlN as a consequence of premature seed decomposition. The decomposition of the seeds was suppressed by proper selection of the growth parameters (e.g. growth temperature) and by employing high-quality seeds. Below 1900°C, coalesced AlN layers up to 1 mm thick were grown on both on-axis and off-axis seeds with a low ($< 30 \text{ cm}^{-2}$) micropipe density, and the AlN growth mode changed from dislocation-mediated spiral growth observed on on-axis seeds to step-flow growth observed on off-axis seeds. Cracks were always observed in these layers. An estimate of the minimum AlN thickness required on SiC to avoid cracking due to thermal stress was calculated from a one-dimensional stress distribution model, indicating a minimum thickness of 4.7 mm. In order to increase the growth rate of AlN deposited by PVT, a two-step growth process was developed for growth of thick AlN bulk crystals on SiC seeds, yielding AlN layers up to 3

mm thick. Crack-free AlN crystals were obtained from the grown layers by evaporating the SiC seed *in situ* during high-temperature PVT growth. In addition, IDs were observed in AlN crystals grown on on-axis seeds coated with an MOCVD AlN epilayer. Further investigation is required to determine the nucleation mechanism of the IDs. These defects were not observed in AlN grown on bare off-axis SiC, indicating that they may potentially be eliminated by selection and treatment of the growth surface. The main results of this chapter are summarized below, where specific challenges and the corresponding growth strategies to overcome the challenges are indicated:

- seed decomposition → SiC quality, growth parameters
- hillock formation → SiC seed orientation, growth parameters
- crack formation → AlN layer thickness, SiC seed evaporation
- ID formation → SiC seed orientation, surface treatment

4 Conclusions and Possible Future Work

4.1 Aluminum nitride crystal growth

AlN bulk crystal growth by PVT in nitrogen atmosphere was studied using a resistively heated reactor. AlN crystals were grown at elevated temperatures by two different methods, by spontaneous nucleation on the crucible inner surface (self-seeded growth) and by seeded growth on singular and vicinal (0001) surfaces of SiC seeds.

During self-seeded growth experiments a variety of crucible materials, such as BN, W, Ta, Re, TaN, and TaC, were evaluated. AlN bulk crystals grown in BN crucibles exhibited highly anisotropic growth rates along different crystallographic directions. Crucibles made of refractory metals, and metal carbides or nitrides, yielded well-faceted crystals with isotropic growth rates. These studies showed that the morphology of crystals grown by spontaneous nucleation strongly depends on the growth temperature and contamination in the reactor. Crucible selection had a profound effect on contamination in the crystal growth environment, influencing nucleation, coalescence, and crystal morphology. Depending on the choice of reaction crucible, crystals were optically clear or tinted orange. Deep orange coloration was routinely observed in crystals grown in refractory metal crucibles. Crystals of very high crystalline quality were obtained in all crucibles, as indicated by SWBXT and HRXRD. Thus, while crystal color, growth habit, and morphology were affected by the choice of crucible materials, the density of extended defects and their distribution in the crystals remained unaffected. Based on crucible lifetime, materials compatibility, and crystal quality the best results for AlN sublimation growth were obtained in crucibles made of sintered TaN and TaC. Further evaluation of other inert, high-

temperature materials may prove fruitful. Further research is also needed to improve the understanding of the detrimental effects of various impurities in AlN, so that technologically relevant properties of AlN may be fully exploited by reducing the concentration of adverse growth contaminants.

Seeded growth of AlN bulk crystals on SiC seeds was investigated as a means to scale up maximum single crystal size and pre-define crystal orientation. SiC seed stability during the early stages of AlN growth was highly sensitive to the growth temperature, and influenced the coalescence of the AlN initial nucleation layer. Below 1900°C, coalesced AlN layers were obtained on both on-axis and off-axis (0001) Si-face seeds, while growth above this temperature resulted in decomposition of the SiC and incomplete coalescence of the initial nucleation layer. The subsequent growth behavior depended strongly on the formation of a coalesced nucleation layer. Voids and holes were observed in the AlN as a consequence of premature seed decomposition. Therefore, a two-step deposition process was developed for the growth of thick layers. During the low-temperature stage, a fully coalesced AlN nucleation layer that could sustain subsequent growth was deposited at growth rates from 10 to 30 $\mu\text{m/hr}$. The temperature was selected such that decomposition of the seed surface was minimized. In order to increase the growth rate of AlN to approximately 70 $\mu\text{m/hr}$, the temperature was then slowly raised. Growth proceeded on the initial AlN layer despite the gradual decomposition of the SiC substrate.

AlN layers up to 3 mm thick were grown by PVT on on-axis SiC seeds using the two-step process. Cracks formed in the AlN layers due to the thermal expansion mismatch between AlN and SiC were observed to decrease with increasing AlN thickness. The thermal

stress distribution in AlN/SiC heterostructures was calculated from a one-dimensional isotropic model. A model estimate of the minimum AlN thickness required to avoid cracking on SiC due to thermal stress indicated that growth of a crack-free AlN/SiC heterostructure was impractical. Instead, crack-free AlN crystals were obtained from grown layers by evaporating the SiC seed *in situ* during high-temperature PVT growth, thereby directly eliminating the source of thermal stress. This process was successfully employed to produce crack-free AlN crystals with pre-determined orientation, which are suitable for use as seeds in subsequent AlN boule growth.

4.2 Aluminum nitride characterization

Spontaneously grown single crystals up to 15 mm in size were characterized by x-ray diffraction, x-ray topography, glow discharge mass spectrometry, and secondary ion mass spectrometry. Average dislocation densities were on the order of 10^3 cm^{-3} , with extended areas virtually free of dislocations. High resolution rocking curves routinely showed peak widths as narrow as 7 arcsec, indicating a high degree of crystalline perfection. Low-temperature partially polarized optical reflectance measurements were used to calculate the crystal-field splitting parameter of AlN, $\Delta_{cr} = -230 \text{ meV}$, and from this, a low-temperature (1.7 K) band gap energy of 6.096 eV was obtained for unstrained wurtzite AlN.

AlN grown on on-axis seeds coated with an MOCVD AlN epilayer was primarily Al-polar, but in some samples etch features consistent with the presence N-polar IDs were revealed by wet etching in hot, aqueous phosphoric acid or KOH solutions. In order to confirm the presence of IDs in these samples, basal plane regions of possible opposite polarity were imaged by PFM. The opposite contrast observed in PFM phase images of these

regions confirmed that they corresponded to regions of opposite polarity, i.e. IDs. These defects were not observed in AlN grown on off-axis SiC. Further investigation is required to determine the nucleation mechanism of the IDs, which is potentially related to surface preparation. Recently, polarity control of nitride thin films grown on sapphire substrates has been demonstrated, which opens up the possibility of new processing routes for film growth. It may be worth investigating whether similar control of nitride film polarity can be achieved on SiC substrates.

Appendices

5 Appendix A: Review of Recent Results of AlN Bulk Crystal Growth

Sublimation Growth of AlN Crystals

R. Dalmau and Z. Sitar

Department of Materials Science and Engineering, North Carolina State University, Raleigh,
North Carolina 27695

in *Encyclopedia of Materials: Science and Technology Updates*, edited by K. H. J. Buschow,
R. W. Cahn, M. C. Flemings, B. Ilshner, E. J. Kramer, S. Mahajan, and P. Veysière
(Elsevier, Oxford, 2005).

Sublimation Growth of AlN Crystals

Wide bandgap nitride semiconductors, AlN, GaN, InN, have been identified as promising materials for a broad range of applications in electronics and optoelectronics. Currently, epitaxial heterostructures involving these semiconductors are being grown by different techniques on a number of substrates (Ambacher 1998, Gaska *et al.* 2002, Liu and Edgar 2002 (a), Monemar 1999, Schowalter *et al.* 2000 (a)). Blue light emitting diodes (LEDs) grown on sapphire and silicon carbide (SiC) substrates are commercially available. Solid state lasers have been demonstrated (Nakamura *et al.* 1998). The two most commonly used substrates, sapphire and SiC, are not closely lattice-matched to the III-nitride overlayers, leading to a high defect density in overgrown active layers, limiting device performance and lifetime. Additional limitations of the currently available substrates include cracking of the device layers due to the large thermal mismatch, and poor thermal conductivity. Thus, the performance of III-nitride semiconductor devices will be greatly improved by the availability of native substrates. High-quality, single crystalline aluminum nitride (AlN) or gallium nitride (GaN) substrates with low dislocation densities are expected to decrease defect density in the overgrown device structures by several orders of magnitude and, thereby, greatly improve the performance and lifetime of III-nitride devices.

AlN has a number of excellent properties that make it a highly desirable candidate as a substrate for III-nitride epitaxy. Its crystalline structure, hexagonal wurtzite (2H), is the same as that of GaN, with a lattice mismatch in the c-plane of approximately 2.5%. Since AlN makes a continuous range of solid solutions with GaN, it plays an important role in GaN-based devices and is highly suited as a substrate for AlGaN devices with high Al

concentrations or structures with graded layers. Its high thermal conductivity, 3.2 W/cm K (Slack 1973), makes it desirable for high-temperature electronic and high power microwave devices where heat dissipation is critical. The direct, large optical bandgap (6.2 eV) makes it suitable for ultraviolet applications down to wavelengths as short as 200 nm and its high resistivity is beneficial for these applications. It is also distinguished by high hardness, chemical and thermal stability.

Past efforts to grow AlN bulk crystals have explored sublimation, vaporization, and solution routes, with sublimation yielding the most voluminous AlN crystals to date. Crystal growth by other methods, such as hydride vapor phase epitaxy (Albrecht *et al.* 1999, Nikolaev *et al.* 2000), ammonothermal growth (Dwilinski *et al.* 1998), or solution growth (Dugger 1974, Bockowski 2001), has been reported, but only crystals of either inferior quality or size have been produced thus far. In contrast, the efforts of several groups (e.g. Rojo *et al.* 2001 (b), Schlessler and Sitar 2002, Edgar *et al.* 2002, Bickermann *et al.* 2003) clearly demonstrate that bulk AlN crystals of very high quality and of sizes appropriate for use as III-nitride substrates can be produced by sublimation growth. This article reviews recent results of bulk AlN crystal growth.

5.1 Sublimation growth: technique and process parameters

Although the first AlN was synthesized in 1862 by Briegleb and Geuther by the reaction between molten aluminum and nitrogen, it took more than a century before any sizeable single-crystals of AlN were grown (Slack 1980). In recent years, several research groups independently developed processes and models for growth of AlN crystals which all converge to the same basic growth principle and process parameter space. As shown

schematically in Figure 5.1, the AlN crystal growth process is similar to the sandwich sublimation process for growth of SiC. An AlN powder source is placed at the bottom of a crucible and sublimed onto a colder seed in a nitrogen atmosphere. AlN growth can be achieved at temperatures as low as 1800°C; however, temperatures in excess of 2300°C are required to achieve commercially viable growth rates. This high growth temperature, in combination with highly reactive Al vapor, creates a challenging problem in selection of crucible materials and has been a major obstacle in growth of high-purity, large-size AlN crystals.

Early kinetic theory formulation for the sublimation growth of AlN indicated that the useful growth temperature range was 2000–2400°C, yielding growth rates ranging from 0.3–15 mm/hr (Dryburgh 1992). A two-dimensional model of mass transport in the gas phase was analyzed by Liu and Edgar (2000), who determined that the activation energy for AlN growth at pressures over 200 Torr was 681 kJ/mol, which is close to the heat of sublimation of AlN. To better describe growth at pressures below 100 Torr, a refined model (Liu and Edgar 2002 (b)) included the influence of surface kinetics (N_2 sticking coefficient), which is not a limiting factor at higher pressures. Karpov *et al.* (1999) and Segal *et al.* (2000) identified two mechanisms of vapor transport in AlN sublimation: at high pressure (760 Torr), vapor transport was controlled by diffusion in the gas phase, while at low pressure ($\sim 10^{-4}$ Torr), it was dominated by drift of the reactive species, Al and N_2 . Growth at low pressure required 350–400°C lower temperature to achieve the same growth rate. Good agreement of the theoretically predicted AlN growth rate with experimental results for both Al-rich and N-rich conditions as a function of seed temperature was obtained as shown in

Figure 5.2 (Segal *et al.* 2000). A one-dimensional model was developed for the high temperature growth by Noveski *et al.* (2004(a)). Sustained growth rates on the order of millimeters per hour were demonstrated, clearly showing that the growth rate is diffusion limited at total nitrogen pressures in the range of 400–800 Torr.

Two-dimensional simulations (Karpov *et al.* 2001) demonstrated that at a given temperature both the powder source and the seed sublime below a critical pressure when the sum of Al and N₂ partial pressures at the seed and source are greater than the ambient pressure. Under growth conditions below this critical pressure, the simulations showed that the gas phase is transported out of the growth cell and the sublimation growth fails.

5.2 Materials' requirements for crystal growth

By necessity, commercially viable growth rates are achieved at very high process temperatures (typically > 2200°C), making furnace design and materials selection critical to the success of the overall process, both for achieving durability of growth hardware and keeping crystal impurity levels low. In particular, crucible materials must withstand repeated temperature cycling and highly reactive Al vapor.

In his early work, Slack (1980) has shown successful growth using W crucibles; however, crucible lifetime was limited and ~50 ppm of W incorporation was reported. Some efforts have employed graphite or coated (SiC, NbC, TaC) graphite crucibles. Several independent studies show that pure graphite crucibles should be avoided due to incompatibility with Al, high levels of carbon in crystals, and detrimental influence of carbon on growth morphology. Coated graphite crucibles reduce these shortcomings for low

temperature growth, however, these coatings deteriorate quickly above 2000°C and do not offer a long-term stable growth environment.

Boron nitride has been used by both Schlessler *et al.* (2002 (a)) and Edgar *et al.* (2002). Sizeable transparent crystals with very low dislocation densities were grown; however, it seems that a BN growth environment produces highly anisotropic growth rates at high temperatures, where the growth rate in a-direction is almost completely inhibited. As a result, coalescence and crystal-size expansion are difficult to achieve.

Compatibility of reactor materials at the high temperatures needed for crystal growth was addressed by Epelbaum *et al.* (2002). Crystals were grown from AlN powder with approximately 1% aluminum oxide impurity in a resistively heated reactor at temperatures of 1800–2200°C using tungsten or graphite heating elements. Different combinations of crucible materials and heating elements yielded results similar to those reported previously (Balkas *et al.* 1997). Crucibles made of graphite were readily attacked by the aluminum vapor, while graphite crucibles coated with silicon carbide were unstable at temperatures above 1950°C, leading to the formation of mixed AlN-SiC crystals varying in color from dark blue to light green. Problems were also associated with the combination of W crucible and heating element, namely degradation of W by aluminum vapor or by oxygen from impurities in the source. The most flexible reactor design was deemed to be a combination of W crucible and graphite heating element.

More recently, efforts with sintered tantalum nitride and tantalum carbide crucibles confirmed that these materials are more stable than any of the aforementioned crucible materials, with crucible lifetimes exceeding 500 hours at growth temperature. Well-faceted

crystals with isotropic growth and very low dislocation densities were obtained (Dalmau *et al.* 2004). However, further evaluation of other inert, high-temperature materials may prove fruitful. Further research is also needed to improve the understanding of the effect of various impurities in AlN, so that technologically relevant properties of AlN may be optimized by reducing the most detrimental growth contaminants.

5.3 Self-seeded crystal growth

Spontaneously nucleated crystals observed by Tanaka *et al.* (1997) were transparent with a slight yellow tint. Growth was performed in graphite crucibles at source temperatures between 1900–2100°C. Depending on growth temperature, three crystal morphologies were observed and studied: needles with rectangular cross-section grew at 1900°C, hexagonal cross-section needles grown parallel to c-direction were observed at 2000°C, while growth at 2100°C yielded (0001) platelets. All crystals measured several mm in the largest dimension. Analysis indicated 1:1 Al to N ratios, and 800 ppm by mass oxygen content. The yellow color was attributed to blue light absorption by the oxygen impurity.

Edgar *et al.* (2000, 2002) reported on AlN crystal growth by sublimation in resistively heated furnaces with tungsten or graphite heating elements. AlN needles and platelets freely nucleated from AlN source material in the cold zone of boron nitride (BN) crucibles. Source temperatures were varied from 2000 to 2200°C and reactor nitrogen pressures ranged from 300 to 800 Torr. Crystals grown in a furnace with tungsten heating elements were either colorless or amber in color, while those grown in a furnace with a graphite heater were colorless. Observed morphologies included needles up to 4 mm in length and 0.5 mm in diameter, and thin plates. The plates were as large as 60 mm² and contained growth striations

running the length of the crystals along the c-direction. These striations appear to be characteristic of crystals grown in BN environments. They are not seen in AlN grown in other types of crucibles (Edgar *et al.* 2002).

AlN boules up to 10 mm in diameter were produced at Crystal IS (Schowalter *et al.* 2000 (b)) in conical crucibles. No seed crystals were used in the growth process and, typically, several nuclei formed on the crucible walls during the early stages of growth. As the crystal grew, growth competition between different nuclei resulted in single crystal regions of varying sizes and orientations. A driving rate for growth was set by translation of the crucible relative to the thermal gradient in the reactor. Under adequate growth conditions (e.g. thermal gradient, reactor pressure) the driving rate was equal to the crystal growth rate, which was varied between 0.65–0.9 mm/hr. Atomic force microscopy (AFM) imaging of the as-grown crystals revealed 0.25 nm-high monolayer steps with straight segments. Step flow resulted from screw dislocations intersecting the growing surface. Screw dislocation density was estimated at $5 \times 10^4 \text{ cm}^{-2}$.

Wafering of these boules revealed several large grains and polycrystalline regions, or single-crystalline regions exhibiting severe cracking around the periphery, as shown in Figure 5.3 (Rojo *et al.* 2001 (a), Rojo *et al.* 2001 (b), Rojo *et al.* 2001 (c)). Chemo-mechanical polishing (CMP) was used to obtain surfaces suitable for epitaxial growth. Final etching of vicinal surfaces in a mixture of phosphoric and sulfuric acids or potassium hydroxide solution revealed that the N-terminated face was etched much faster and rougher than the Al-terminated face.

The most recent characterization results reported for bulk single crystals grown at Crystal IS demonstrated that crystals were of high quality (Raghothamachar *et al.* 2003). Figure 5.4 shows the final wafer, which was unevenly shaped and approximately $7 \times 9 \text{ mm}^2$ in size. X-ray topographs indicated no significant strain in the wafer and showed an overall dislocation density of $800\text{--}1000 \text{ cm}^{-2}$. The density of detected inclusions (presumably oxygen) was on the order of 10^5 cm^{-3} . Full width at half-maximum (FWHM) of high-resolution rocking curves ranged from 9 to 12 arcsec, indicating very good crystalline quality. The edge of the wafer in contact with the crucible wall contained cracks and slip bands, probably due to the thermal expansion mismatch between the boule and crucible.

Bulk AlN with low oxygen content was reported by Bickermann *et al.* (2003). Polycrystals were grown in a vertical, cold-wall reactor equipped with W heating elements. Growth was performed in nitrogen atmosphere, at pressures below 1000 mbar, using almost-sealed crucibles. Source and crystal growth temperatures ranged from 2200 to 2350°C, and from 2100 to 2250°C, respectively. Dense, polycrystalline AlN boules up to 15 mm high and 2 inches in diameter were produced with growth rates between 0.2 and 2 mm/h. Boules were composed of c-textured crystalline grains, some as large as 5x5 mm. Although the AlN source material contained significant amounts of various impurities (6,000 ppm wt oxygen, 300 ppm wt carbon, and 500 ppm wt metals), impurity incorporation into grown material was significantly lower (86 ppm wt oxygen, 100 ppm wt carbon, ~22 ppm wt metals). Optical absorption measurements showed fundamental absorption above 6.0 eV, and two broad absorption bands at 2.8 and 4.2 eV, which were attributed to photoionization of deep donor electrons, but the exact nature of these defects is unclear. Slack *et al.* (2002) have reported an

oxygen-related absorption region between 3.5–5.2 eV, with peak positions varying from 4.3–4.8 eV depending on the amount of oxygen impurity.

Schlesser *et al.* (2002 (a)) and Schlesser and Sitar (2002) reported on growth of AlN by vaporization of metallic Al in a nitrogen atmosphere and by sublimation of an AlN source (Schlesser *et al.* 2002 (a), Schlesser *et al.* 2002 (b)). Growth temperatures ranged from 1800–2300°C at reactor pressures of 250–750 Torr. Temperature gradients of 10–100°C/cm between the source material and crystal growth region were employed. In Al vaporization experiments, the crystal shape and fastest growth direction was found to strongly depend on the growth temperature: at relatively low temperatures (1800–1900°C) long needles were grown, temperatures around 1900–2000°C yielded twinned platelets, while c-platelets were formed at temperatures above 2100°C. These c-plates grew at a rate of 5 mm/hr in the c-plane and 0.2 mm/hr along the c-axis. Vaporization experiments were performed for 2 hours each at a constant growth temperature. Longer growth times did not yield substantially larger crystals. The observed slowdown in growth rate with time was attributed to a decreasing Al flux from the Al source over time, which was due to the progressive formation of an Al-rich, polycrystalline AlN coating over the molten Al.

In order to overcome problems with the Al source instability in vaporization experiments, crystals were grown for longer periods of time by subliming AlN source material (Schlesser *et al.* 2002 (a)). Sublimation yielded a stable Al flux over several days of growth. Experiments were carried out at higher temperatures of 2200–2300°C in order to obtain vapor pressures of Al above AlN comparable with those above metallic Al in the vaporization experiments. Transparent AlN single crystals with dimensions as large as 13

mm were grown with growth rates exceeding 500 $\mu\text{m/hr}$ (Figure 5.5). These sublimation experiments were performed in BN crucibles and typically yielded fastest growth along the c-axis and crystals with surface striations along the c-direction, similar to those observed by Edgar *et al.* (2002).

X-ray topography studies of crystals grown by sublimation of AlN powder revealed crystals to be virtually dislocation-free, as shown in Figure 5.6 (Raghothamachar *et al.* 2002). Overall dislocation densities were estimated to be around 10^3 cm^{-2} . Defects such as inclusions, growth sector boundaries, and growth dislocations were detected. Presence of Pendellösung fringes in the topographs was indicative of the high crystalline perfection attained in several samples. Triple-crystal X-ray rocking curve FWHM of several large crystals ($\sim 10 \text{ mm}$) were as low as 7.2 arcsec, marginally larger than the theoretical limit of 6 arcsec.

5.4 Seeded growth of AlN crystals

5.4.1 Growth of AlN on SiC seeds

The growth of AlN crystals seeded on SiC substrates was first reported by Balkas *et al.* (1997). Single crystal platelets were grown in a resistively heated graphite furnace by the sublimation-recondensation method. Growth temperature was varied from 1900–2250°C. SiC-coated graphite crucibles were used in 10–15 hour experiments. The source material was 99% dense sintered AlN, chosen to allow controllable source-to-seed separation, which was crucial for good crystal growth. Optimal separation was found to be between 1 and 5 mm. Single-crystal 6H-SiC (0001) substrates $10 \times 10 \text{ mm}^2$ were used as seeds. Growth in a high-temperature range (2100–2250°C) and a low-temperature range (1950–2050°C) was

investigated. Single crystals of ~ 1 mm thickness that covered the entire SiC seed were grown at 2150°C and 4 mm separation distance. The growth rate was estimated at 0.5 mm/hr. Due to the degradation of the SiC substrates at higher temperatures, isolated nucleation sites were formed on the seeds at temperatures above 2150°C and $2 \times 2 \text{ mm}^2$ hexagonal AlN crystals were grown. The crystals were colored from green to blue, indicating the incorporation of impurities. Secondary ion mass spectrometry (SIMS) analysis confirmed the presence of Si and C in these crystals. Crystals grown in the low-temperature range were colorless and transparent, but growth rates were significantly lower, 30-50 $\mu\text{m/hr}$. Cracking was always observed in as-grown crystals, due to the thermal expansion coefficient mismatch between SiC and AlN. XRD patterns confirmed the single crystal nature of all crystals. Bright-field, plan view transmission electron microscopy (TEM) and associated selected area diffraction (SAD) also indicated the high quality of the single crystals.

The growth of AlN crystals by sublimation on 6H-SiC seeds was more extensively investigated by Edgar *et al.* 2000 and 2002, Shi *et al.* 2001 (a), 2001 (b), and 2001 (c), Liu *et al.* 2001 (a), 2001 (b), and 2001 (c). Experiments were carried out in tungsten crucibles placed within the axial temperature gradient of a resistively heated furnace. The growth temperature was typically 1800°C . SiC wafers (on-axis and 3.5° off-axis) with silicon and carbon terminations were used as substrates. Direct growth (Shi *et al.* 2001 (a)) on as-received Si-terminated SiC resulted in the formation of discontinuous hexagonal sub-grains of 1 mm^2 average size. No growth was observed on C-terminated as-received SiC. In order to promote two-dimensional growth on Si-terminated substrates, a 2 μm -thick AlN buffer layer was deposited by metal-organic chemical vapor deposition (MOCVD). Continuous growth

was achieved by the use of the buffer layer, although cracks formed during cool down due to stress resulting from the thermal expansion coefficient mismatch. AFM images indicated that AlN grew by the step-flow growth mode.

The initial stages of AlN growth on SiC were studied by Liu *et al.* (2001 (c)). Fifteen-minute growth runs were performed on as-received on-axis, Si-terminated 6H-SiC (0001) substrates under different temperature and pressure conditions. During the initial stages of growth, AlN nucleated as individual hexagonal hillocks and platelets in an island-like growth mode. Nuclei size and density increased at constant pressure with increased growth temperature in the range of 1800–1900°C. At constant temperature, growth under reduced pressures yielded coalesced, irregularly shaped platelet crystals. Scanning Auger microscopy (SAM) measurements indicated varying relative compositions of Al, N, Si, and C on different crystal facets of the AlN nuclei. The surface morphology and stress in AlN crystals grown on SiC substrates were also characterized (Liu *et al.* 2001 (b), Liu *et al.* 2001 (c)). AFM images revealed scratches and steps on as-received 6H-SiC substrates, which served as nucleation sites for individual AlN grains grown in a three-dimensional mode. On SiC substrates with an AlN MOCVD epilayer, however, AlN deposited in a two-dimensional growth mode without island formation. Surface morphology varied across the sample, from flat surfaces to regions with large steps (120 nm) separated by large terraces (up to 5 µm). RMS roughness for samples grown with an AlN epilayer was less than 5 nm, compared to 40 nm for crystals grown on as-received substrates. Stress-induced cracks were always observed in the AlN crystals. It was predicted (Liu *et al.* 2002) that AlN grown on 6H-SiC should be at least 2 mm thick in order to avoid cracking during cool down from a growth temperature of

2000°C. Raman spectroscopy revealed that crystals were under compressive stress at the surface and tensile stress (1 GPa) at the interface. Raman spectra indicated improved crystal quality with increasing AlN thickness.

The above method was modified in order to reduce cracking of AlN (Shi *et al.* 2001 (b) and 2001 (c)). After deposition of the MOCVD AlN epilayer, an AlN_{0.8}SiC_{0.2} alloy layer was deposited by sublimation from a source mixture of AlN-SiC powders. Pure AlN was then sublimed on the alloy seed as above. The intermediate properties of the alloy layer helped reduce cracking in the overgrown AlN. In addition, the SiC powder source decreased the degradation of the SiC substrates during sublimation growth, allowing for longer growth times. Single crystal AlN, 4 mm x 6 mm and 0.5 mm thick, was obtained after 100 hours of growth (Figure 5.7). Characterization by XRD and Raman spectroscopy confirmed the high quality of the grown material. Thus, three problems identified with growth of AlN on SiC seeds were addressed by this method: (1) the presence of Si and C in the vapor helped suppress the decomposition at high temperature of the SiC seed; (2) an AlN epilayer promoted two-dimensional growth; (3) cracking of the AlN bulk layer was greatly reduced by an AlN-SiC alloy interlayer.

In other efforts, Sarney *et al.* (1999) grew bulk AlN on 6H on-axis and 3.5° off-axis, c-oriented SiC seeds. Sublimation from an AlN powder source in nitrogen atmosphere was performed in the temperature range 2150–2200°C with 4 mm separation between the source and seed. The AlN grew well-aligned with the substrate. As in previous work (Balkas *et al.* 1997), cracks were observed in the AlN. Epelbaum *et al.* (2003) studied AlN crystal growth on SiC substrates of different orientations. Layers of 200–500 μm thickness were deposited

at seed temperatures around 2000°C in 350 mbar nitrogen pressure. Growth on Si-face, c-oriented substrates was characterized by many hexagonal hillocks on the surface. In contrast, 10° off-axis and on-axis a-plane substrates resulted in more stable growth. The smoothest morphology, typical of step-flow growth, was obtained with on-axis, a-plane substrates, however, cracks were also observed in the AlN layers.

5.4.2 Growth of AlN on AlN seeds

Reports on AlN growth on native seeds are very limited, as these seeds have only recently become available. Seeded growth of AlN on native seeds by the sublimation method was reported for the first time by Schlessler et al. (2002 (b)). Transparent, single-crystal c-platelets prepared by vaporization of Al were used as seeds. They were mounted into the top of a BN growth crucible filled with AlN source material. Growth was carried out at 2200°C with a temperature gradient between the source and seed of approximately 3°C/mm. Figure 5.8 shows a sequence of experiments in which a small seed, 4 mm tall and 0.5 mm thick, grew over a total of 34 hours into a 5 mm tall and 7 mm wide single crystal. Growth rates were highly anisotropic, with the fastest growth direction along the c-axis. Also, growth rates on the two c-faces of opposite polarity differed by a factor of 2–3, with the Al polarity showing slower and smoother growth. Crystal quality of the grown crystals was characterized by XRD. X-ray rocking curves around the (0002) reflection varied from 25 to 45 arcsec, indicating very high single crystal quality of the material grown by seeded growth.

Noveski et al. (2004(b)) recently demonstrated a process for continuous growth of AlN on previously deposited material, resulting in significant expansion of single crystal grains. Growth was performed in an RF heated reactor at temperatures between

2110–2140°C and pressures of 450–500 Torr, yielding growth rates in the range of 0.1–0.3 mm/hr. In this process, a starting layer of coalesced polycrystalline AlN was grown into boules up to 1.5” in length and 1.0” in diameter over the course of several growth runs. Sublimation growth from a pre-sintered AlN source was interrupted several times in order to replenish the source and keep the source-to-seed distance constant. Re-nucleation of AlN on the previous growth front after exposure of the boules to air was suppressed by using the inverted temperature gradient method. During the early stages of each run, the crystal growth region was maintained in an inverted temperature gradient, effectively desorbing surface contamination and part of the previously grown layer. In this manner, continuous expansion of previously formed single crystalline grains was achieved. Centimeter-sized, single-crystal grains were observed in polished cross sections of boules.

5.5 Summary

AlN crystal growth is a challenging task that has been attempted in the past via a variety of growth methods. Although several issues remain, sandwich sublimation of AlN powder at high temperatures shows the most promising results. This method has yielded AlN crystals of very high quality and of sufficient size for fabrication of the first devices. Recent demonstration of seeded growth is certainly an important milestone for future development of this technology that will lead to expansion of crystal size. Lifetime and stability of growth crucibles and reactor parts remain a challenge that will need to be addressed in the quest for high-purity crystals and lower production cost.

5.6 Acknowledgements

This work was supported by the DoD Multidisciplinary University Research Initiative (MURI) administered by the Office of Naval Research (ONR) under grant N00014-01-1-0716, monitored by Dr. Colin E. Wood.

5.7 Bibliography

- Albrecht M, Nikitina I P, Nikolaev A E, Melnik Y V, Dimitriev V A, Strunk H P 1999 Dislocation reduction in AlN and GaN bulk crystals by HVPE. *Phys. Stat. Sol. (a)* **176**, 453–58
- Ambacher O 1998 Growth and applications of group III-nitrides. *J. Phys. D* **31**, 2653–710
- Balkas C M, Sitar Z, Zheleva T, Bergman L, Nemanich R, Davis R F 1997 Sublimation growth and characterization of bulk aluminum nitride single crystals. *J. Cryst. Growth* **179**, 363–70
- Bickermann M, Epelbaum B M, Winnacker a 2003 PVT growth of bulk AlN crystals with low oxygen contamination. *Phys. Stat. Sol. (c)* **0**, 1993–96
- Bockowski M 2001 Growth and doping of GaN and AlN single crystals under high nitrogen pressure. *Cryst. Res. Technol.* **36**, 771–87
- Dalmau R, Raghathamachar B, Dudley M, Schlessner R, Sitar Z (2004) Crucible selection in AlN bulk crystal growth. *Mat. Res. Soc. Symp. Proc.* **798**, Y2.9.1-2.9.5
- Dryburgh P M 1992 The estimation of maximum growth rate for aluminum nitride crystals grown by direct sublimation. *J. Cryst. Growth* **125**, 65–8
- Dugger C O 1974 Synthesis of AlN single crystals. *Mater. Res. Bull.* **9**, 331-36
- Dwilinski R, Doradzinski R, Garczynski J, Sierzputowski L, Palczewska M, Wysmolek A, Kaminska M 1998 AMMONO method of BN, AlN and GaN synthesis and crystal growth. *MRS Internet J. Nitride Semicond. Res.* **3**, 25

- Edgar J H, Robins L H, Coatney S E, Liu L, Ignatiev K, Rek Z 2000 A comparison of aluminum nitride freely nucleated and seeded on 6H-silicon carbide. *Mater. Sci. Forum* **338-342**, 1599–1602
- Edgar J H, Liu L, Liu B, Zhuang D, Chaudhuri J, Kuball M, Rajasingam S 2002 Bulk AlN crystal growth: self-seeding and seeding on 6H-SiC substrates. *J. Cryst. Growth* **246**, 187–93
- Epelbaum B M, Bickermann M, Winnacker A 2003 Seeded PVT growth of aluminum nitride on silicon carbide. *Mater. Sci. Forum* **433-436**, 983-86
- Epelbaum B, Hoffman D, Bickermann M, Winnacker A 2002 Sublimation growth of bulk AlN crystals: materials compatibility and crystal quality. *Mater. Sci. Forum* **389-393**, 1445–48
- Gaska R, Chen C, Yang J, Kuokstis E, Khan A, Tamulaitis G, Yilmaz I, Shur M S, Rojo J C, Schowalter L J 2002 Deep-ultraviolet emission of AlGaN/AlN quantum wells on bulk AlN. *Appl. Phys. Lett.* **81**, 4658-60
- Karpov S Yu, Kulik A V, Ramm M S, Mokhov E N, Roenkov A D, Vodakov Yu A, Makarov Yu N 2001 AlN crystal growth by sublimation technique. *Mat. Sci. Forum* **353-356**, 779-82
- Karpov S Yu, Zimina D V, Makarov Yu N, Mokhov E N, Roenkov A D, Ramm M G, Vodakov Yu A 1999 Sublimation growth of AlN in vacuum and in a gas atmosphere. *Phys. Stat. Sol. (a)* **176**, 435-38
- Liu B, Shi Y, Liu L, Edgar J H, Braski D N 2001 (c) Surface morphology and composition characterization at the initial stages of AlN crystal growth. *Mat. Res. Soc. Symp. Proc.* **639**, G3.13.1-G3.13.6
- Liu L, Liu B, Edgar J H, Rajasingam S, Kuball M 2002 Raman characterization and stress analysis of AlN grown on SiC by sublimation. *J. Appl. Phys.* **92**, 5183-188
- Liu L, Liu B, Shi Y, Edgar J H 2001(a) Growth mode and defects in aluminum nitride sublimed on (0001) 6H-SiC substrates. *MRS Internet J. Nitride Semicond. Res.* **6**, 7

- Liu L, Zhuang D, Liu B, Shi Y, Edgar J H, Rajasingam S, Kuball M 2001(b) Characterization of aluminum nitride crystals grown by sublimation. *Phys. Stat. Sol. (a)* **188**, 769-73
- Liu L, Edgar J H 2000 Transport effects in the sublimation growth of aluminum nitride. *J. Cryst. Growth* **220**, 243-53
- Liu L, Edgar J H 2002(b) A global growth rate model for aluminum nitride sublimation. *J. Electrochem. Soc.* **149**, G12-G15
- Liu L, Edgar J H 2002(a) Substrates for gallium nitride epitaxy. *Mat. Sci. Eng. R* **37**, 61-127
- Monemar B 1999 III-V nitrides – important future electronic materials. *J. Mat. Sci.* **10**, 227-54.
- Nakamura S, Senoh M, Nagahama S, Iwasa N, Yamada T, Matsushita T, Kiyuku H, Sugimoto Y, Kuzaki T, Umemoto H, Chocho K 1998 Continuous-wave operation of InGaN/GaN/AlGaIn-based laser diodes grown on GaN substrates. *Appl. Phys. Lett.* **72**, 2014-16
- Nikolaev A, Nikitina I, Zubrilov A, Mynbaeva M, Melnik Y, Dimitriev V 2000 AlN wafers fabricated by hydride vapor phase epitaxy. *MRS Internet J. Nitride Semicond. Res.* **5S1**, W6.5
- Noveski V, Schlessner R, Freitas Jr. J, Mahajan S, Beaudoin S, Sitar Z 2004(b) Vapor phase transport of AlN in an RF heated reactor: low and high temperature studies. *Mat. Res. Soc. Symp. Proc.* **798**, Y2.8.1-Y2.8.6
- Noveski V, Schlessner R, Mahajan S, Beaudoin S, Sitar Z 2004(a) Mass transfer in AlN crystal growth at high temperatures. *J. Cryst. Growth* **264**, 369-78
- Raghothamachar B, Dudley M, Rojo J C, Morgan K, Schowalter L J 2003 X-ray characterization of bulk AlN single crystals grown by the sublimation technique. *J. Cryst. Growth* **250**, 244-50
- Raghothamachar B, Vetter W M, Dudley M, Dalmau R, Schlessner R, Sitar Z, Michaels E, Kolis J W 2002 Synchrotron white beam topography characterization of physical vapor transport grown AlN and ammonothermal GaN. *J. Cryst. Growth* **246**, 271-80

- Rojo J C, Slack G A, Morgan K, Raghothamachar B, Dudley M, Schowalter L J 2001(b) Report on the growth of bulk aluminum nitride and subsequent substrate preparation. *J. Cryst. Growth* **231**, 317-21
- Rojo J C, Slack G A, Morgan K, Schowalter L J, Dudley M 2001(a) Growth of self-seeded aluminum nitride by sublimation-recondensation and substrate preparation. *Mat. Res. Soc. Symp. Proc.* **639**, G1.10.1-G1.10.6
- Rojo J C, Schowalter L J, Morgan K, Florescu D I, Pollack F H, Raghothamachar B, Dudley M 2001(c) Single-crystal aluminum nitride substrate preparation from bulk crystals. *Mat. Res. Soc. Symp. Proc.* **680E**, E.2.1.1-E.2.1.7
- Sarney W L, Salamanca-Riba L, Hossain T, Zhou P, Jayatirtha H N, Kang H H, Vispute R D, Spencer M, Jones K A 1999 TEM study of bulk AlN grown by physical vapor transport. *MRS Internet J. Nitride Semicond. Res.* **5S1**, W5.5
- Schlesser R, Dalmau R, Yakimova R, Sitar Z 2002(a) Growth of AlN bulk crystals from the vapor phase. *Mat. Res. Soc. Symp. Proc.* **693**, I.9.4.1-I.9.4.6
- Schlesser R, Dalmau R, Sitar Z 2002(b) Seeded growth of AlN bulk single crystals by sublimation. *J. Cryst. Growth* **241**, 416-20
- Schlesser R, Sitar Z 2002 Growth of bulk AlN crystals by vaporization of aluminum in a nitrogen atmosphere. *J. Cryst. Growth* **234**, 349-53
- Schowalter L J, Shusterman Y, Wang R, Bhat I, Arunmodhi G, Slack G A 2000(a) Epitaxial growth of AlN and Al_{0.5}Ga_{0.5}N layers on aluminum nitride substrates. *Appl. Phys. Lett.* **76**, 985-87
- Schowalter L J, Rojo J C, Yakolev N, Shusterman Y, Dovidenko K, Wang R, Bhat I, Slack G A 2000(b) Preparation and characterization of single-crystal aluminum nitride substrates. *MRS Internet J. Nitride Semicond. Res.* **5S1**, W6.7
- Segal A S, Karpov S Yu, Makarov Yu N, Mokhov E N, Roenkov A D, Ramm M G, Vodakov Yu A 2000 On mechanisms of sublimation growth of AlN bulk crystals. *J. Cryst. Growth* **211**, 68-72

- Shi Y, Liu B, Liu L, Edgar J H, Payzant E A, Hayes J M, Kuball M 2001(b) New technique for sublimation growth of AlN single crystals. *MRS Internet J. Nitride Semicond. Res.* **6**, 5
- Shi Y, Liu B, Liu L, Edgar J H, Meyer H M III, Payzant E A, Walker L R, Evans N D, Swadener J G, Chaudhuri J, Chaudhuri Joy 2001(c) Initial nucleation study and new technique for sublimation growth of AlN on SiC substrate. *Phys. Stat. Sol. (a)* **188**, 757-62
- Shi Y, Xie Z Y, Liu L H, Liu B, Edgar J H, Kuball M 2001(a) Influence of buffer layer and 6H-SiC substrate polarity on the nucleation of AlN grown by the sublimation sandwich technique. *J. Cryst. Growth* **233**, 177-86
- Slack G A 1980 Aluminum nitride crystal growth. Final Report, Contract No. F49620-78-C-0021
- Slack G A 1973 Nonmetallic crystals with high thermal conductivity. *J. Phys. Chem. Solids* **34**, 321-35
- Slack G A, Schowalter L J, Morelli D, Freitas Jr J A 2002 Some effects of oxygen impurities on AlN and GaN. *J. Cryst. Growth* **246**, 287-298
- Tanaka M, Nakahata S, Sogabe K, Nakata H, Tobioka M 1997 Morphology and x-ray diffraction peak widths of aluminum nitride single crystals prepared by the sublimation method. *Jap. J. Appl. Phys.* **36**, L1062-64

5.8 Figures

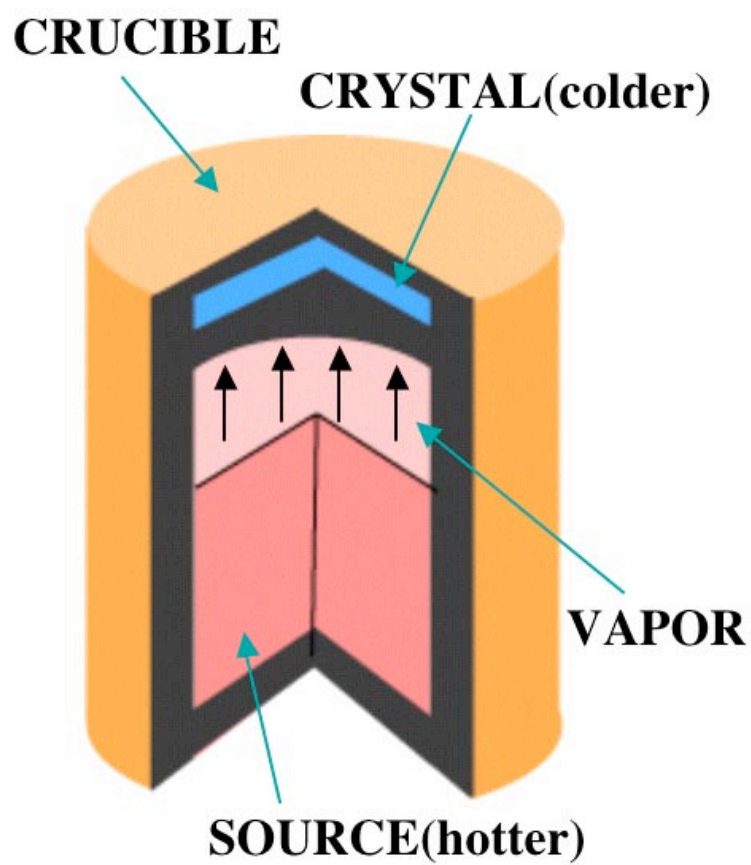


Figure 5.1. Schematic of the AlN crystal growth process; AlN powder source sublimates and recondenses on a colder seed crystal.

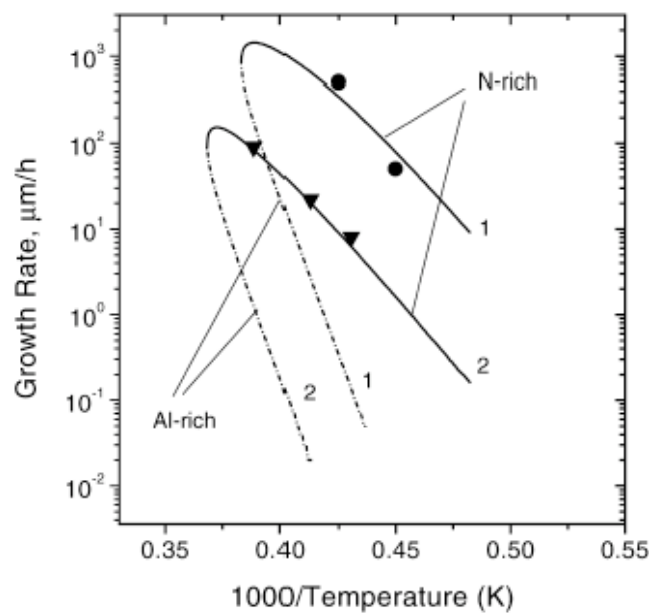


Figure 5.2. Growth rate as a function of the substrate temperature – comparison of computational results with the published data: ● $P=500$ Torr, $\delta=4$ mm, $\Delta T=70^\circ\text{C}$, (Balkas *et al.* 1997); ▼ $P=1$ atm, $\delta=4$ mm, $\Delta T=3.5^\circ\text{C}$ (after Segal *et al.* 2000).

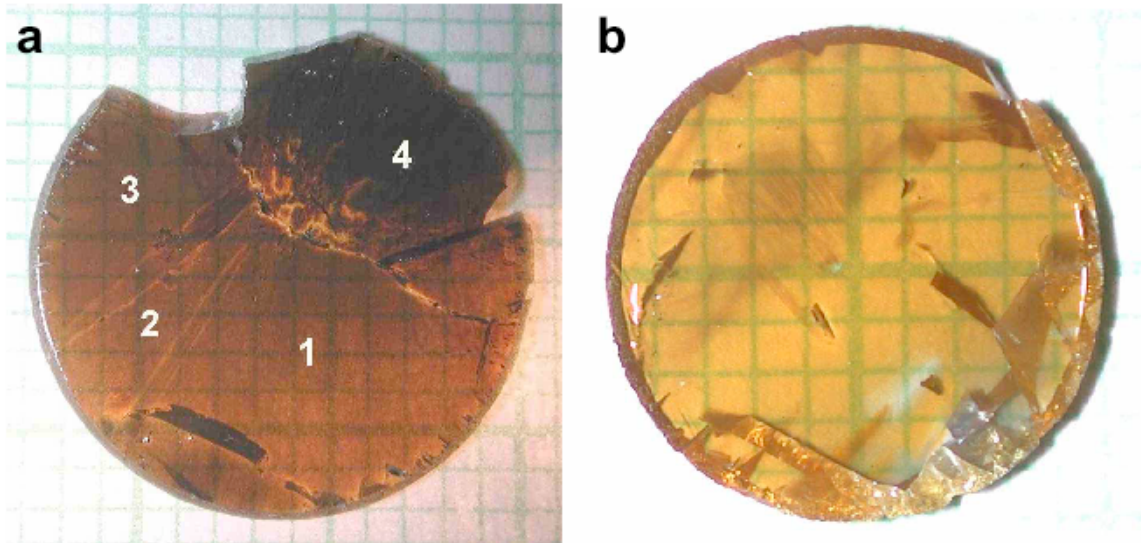


Figure 5.3. a) Picture of a 13.5 mm diameter wafer showing three main single crystal grains (1,2, and 3) and a polycrystalline region (4). b) 10 mm single crystal substrate containing cracked and deformed material around the periphery (after Rojo *et al.* 2001 (c)).

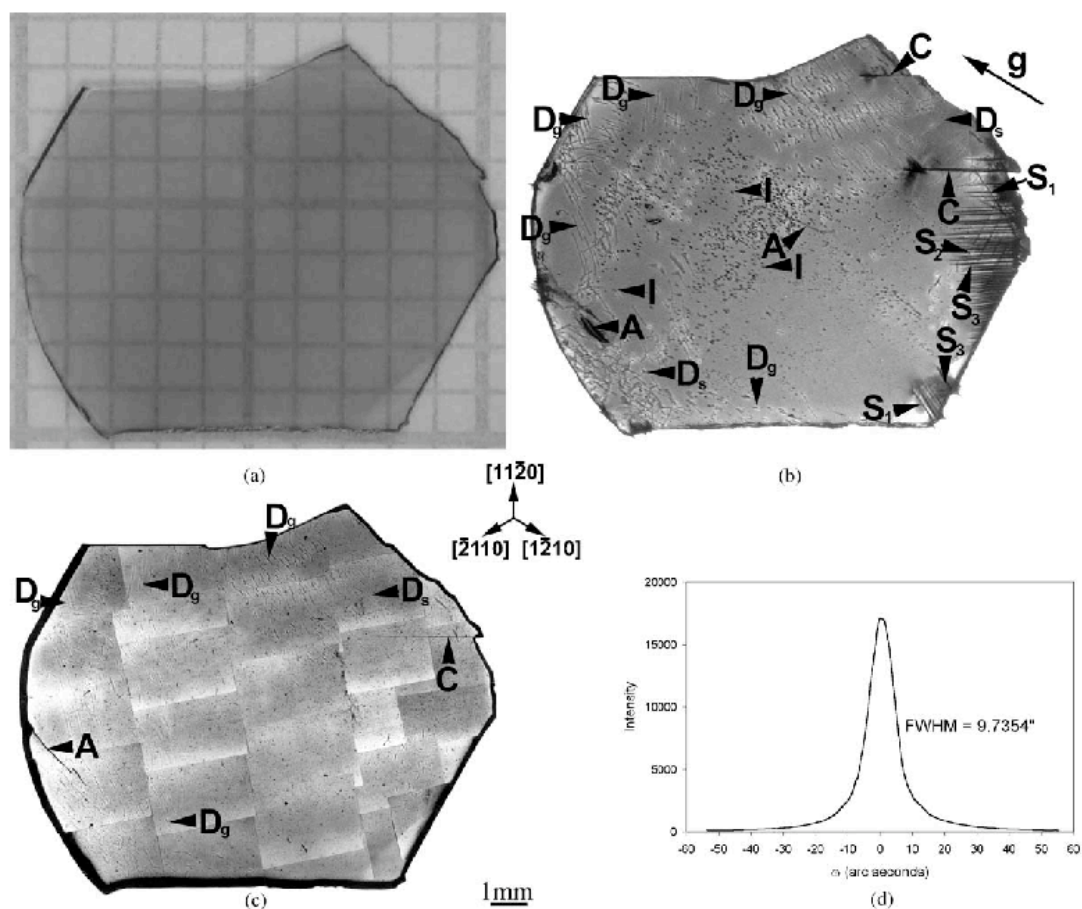


Figure 5.4. (a) Optical photograph of a polished AlN wafer; (b) transmission topograph ($g = -1010$, $\lambda = 0.78 \text{ \AA}$) showing the different defects observed (D_g –growth dislocation, D_s –slip dislocation, S–slip band, C–crack, A–surface artifact/scratch, I–inclusion); (c) optical micrograph showing the same type of defects as topograph; (d) high-resolution triple crystal x-ray diffraction rocking curve, FWHM = 9.7 arcsec (after Raghothamachar *et al.* 2003).

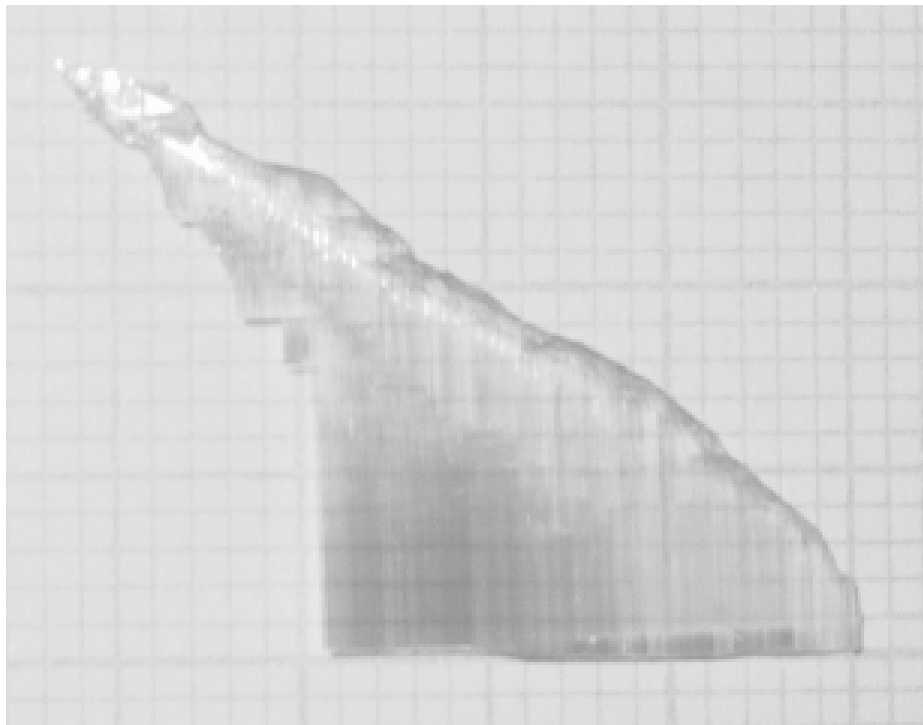


Figure 5.5. AlN single crystal grown by sublimation: grid spacing = 1mm, $T=2260^{\circ}\text{C}$, $p=400$ Torr, growth duration = 24 hrs, average growth rate in c-direction >500 $\mu\text{m/hr}$ (after Schlessner *et al.* 2002 (b)).

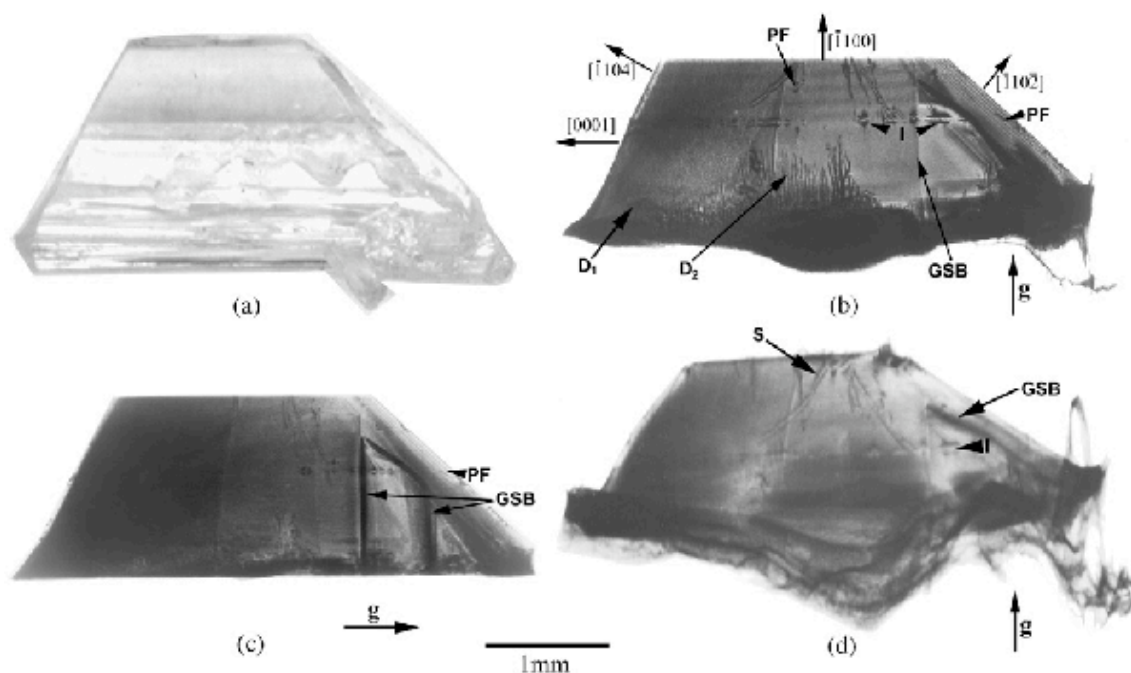


Figure 5.6. (a) Optical photograph of an AlN crystal showing well-defined growth faces. Transmission x-ray topographs: (b) $g = -1100$, $\lambda = 0.75 \text{ \AA}$, showing inclusions (I), growth sector boundaries (GSB), growth dislocations (D_1), and dislocation loops (D_2). Pendellösung fringes (PF) are observed on the upper and right wedged edges; (c) $g = 000-2$, $\lambda = 0.43 \text{ \AA}$; and (d) $g = -12-10$, $\lambda = 0.81 \text{ \AA}$, in which the growth dislocations are extinguished (after Raghothamachar et al. 2002).

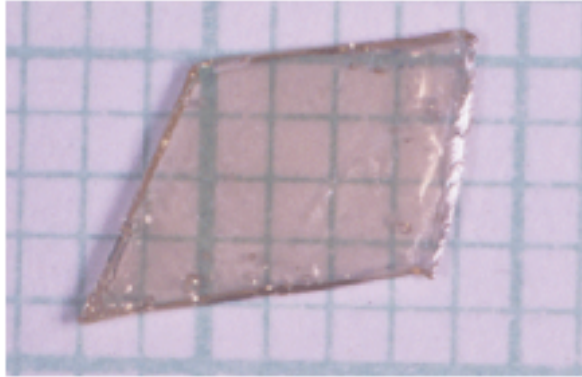


Figure 5.7. Photograph of pure AlN grown for 100 hours. One grid represents 1 mm (after Shi *et al.* 2001 (b)).

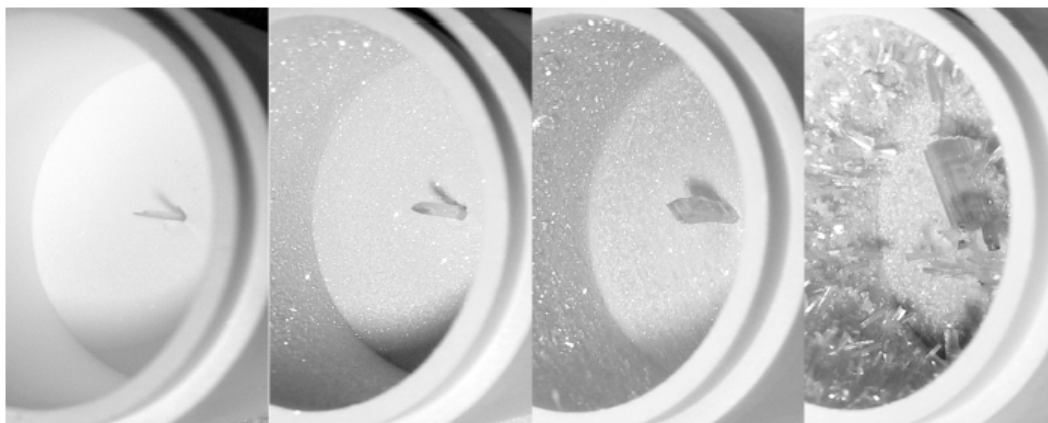


Figure 5.8. Seeded growth by sublimation of AlN. Sequence shows seed (left), and intermediate growth steps after 3, 7, and 34 hrs (after Schlessler *et al.* 2002 (a)).

6 Appendix B: Overview of Selected Characterization Techniques

6.1 Glow discharge mass spectrometry (GDMS)

Impurities in semiconductors, even at very low concentration levels, can have a drastic effect on semiconductor properties. Thus measurement and quantification of impurity concentrations down to ultra-trace levels remains a priority in the development of semiconductor material systems. Several techniques with the necessary detection limits are employed for determination of trace elements, including spark source mass spectrometry (SSMS), inductively coupled plasma optical emission spectroscopy (ICP-OES), SIMS, and GDMS. Of these, GDMS is particularly well suited for the analysis of bulk solid samples and offers several advantages such as high sensitivity, spectral simplicity, applicability to a wide range of material systems, and relative matrix insensitivity.

Dating to 1974,¹⁴⁴ GDMS represents a relatively recent addition to the field of mass spectrometry-based analytical techniques. The high sensitivity of mass spectroscopy techniques and their relative simplicity as compared to corresponding optical spectroscopies, make mass spectrometry an excellent technique for trace element analysis. In order to obtain accurate mass spectra, a large ion population representative of the sample under study must be generated. The techniques for trace element analysis of solid samples all differ in the manner this ion population is generated.

Atomization and ionization of the sample is achieved in SSMS through the use of an energetic spark. The ion beam generated is characterized by instabilities and a broad kinetic energy distribution, leading to decreased analytical performance. In SIMS, a primary beam of ions bombarding the sample surface sputters neutral and ionized sample atoms. The latter,

termed secondary ions, form the analytical signal for determination of sample composition. Since the sample matrix influences the rate at which atoms are sputtered and the degree to which they are ejected as ions, SIMS is limited by the large variations in elemental sensitivity and the matrix effects encountered. Accurate quantification requires calibration of individual elements' signals with respect to a particular reference matrix; calibrated references are not always available for many elements in a matrix of interest. These limitations are largely avoided in GDMS due to the separation of the sample atomization and ionization events in the glow discharge, leading to a decreased dependence of the ion signal on the sample matrix.

In general, there exist two approaches to obtain quantitative results in GDMS.¹⁴⁴ Semi-quantitative analysis based on the ion beam ratio method is accurate to within a factor of 2–3. It is assumed that the ratio of the ion current of a given isotope with respect to the total ion current is a measure of the relative abundance of that isotope. Since trace analysis is typically performed, it is a good approximation to take the matrix ion current as equal to the total ion current, in which case the concentration of an isotope is given by the ratio of its ion current to the matrix ion current. For more accurate quantitative analysis, relative sensitivity factors (RSFs) are employed to correct the measured ion beam ratios based on differences in elemental sensitivity, as in SIMS. However, due to the decreased matrix sensitivity in GDMS, RSFs calculated for elements in matrices of similar composition to that of interest can be employed and yield accuracies of 15–20%, eliminating the need in many cases for matrix matching standards. While RSFs in SIMS can range over three orders of magnitude, RSFs in GDMS are typically limited to one order of magnitude over the entire periodic table.

As the name implies, the ion source in GDMS is supplied by a glow discharge plasma. The discharge is generated by a potential difference of approximately 1 kV applied across electrodes immersed in a low-pressure gas (~1 Torr). The sample material acts as the cathode, and is negatively biased with respect to the anode (the sample cell walls), which is typically kept at system ground potential. The electrical breakdown of the originally insulating, neutral gas due to this potential difference results in the formation of positive gas ions and free electrons in the bulk plasma. The potential difference accelerates positive ions to the cathode (i.e. the sample) where they collide, emitting electrons (secondary electrons) and ionized cathode atoms or neutral cathode atoms (sputtering).

The emitted electrons are accelerated away from the cathode and can participate in two important inelastic collisional processes in the plasma.¹⁴⁵ Ionizing collisions with neutral gas atoms generate additional gas ions and electrons to support the plasma. Excitational collisions produce excited electronic states in the target atom. The excited atom can relax by emission of a photon of wavelength corresponding to an electronic transition. These emissions are characteristic of the target atom and can serve as the basis for qualitative analysis of plasma composition by optical emission spectroscopy (OES). They are also responsible for the plasma glow. Sometimes, electronic relaxation is forbidden by quantum-mechanical selection rules and the atom can remain in a metastable excited state for several seconds. Argon is typically used as a discharge gas and the metastables of argon are energetic enough to contribute to ionization of other species. This Penning ionization is the primary means of forming ions, which can contribute to the analytical signal, from sputtered neutral sample atoms.¹⁴⁶

The ionized atoms that are emitted from the cathode do not contribute to the analytical signal, as they are returned to the cathode surface by the applied negative bias. Thus the source of the analytical signal in GDMS is vastly different to that in SIMS, where these ionized cathode atoms (secondary ions) are used to generate the mass spectra. In GDMS, only neutral sputtered atoms reach the glow discharge, where they are converted to ions through Penning ionization. These ions are then detected by mass spectrometry. Because of the nature of the sputtering process, the cathode surface reaches a steady state surface composition that yields a flux of sputtered atoms that is characteristic of the cathode composition.¹⁴⁷ In this way, the characteristic ion population necessary for accurate mass spectrometry is generated. Analytical signal generation in GDMS thus consists of two steps, sputter atomization and gas-phase ionization, and it is the separation of these two events that leads to the improved analytical capabilities of this technique over SIMS, especially when matrix matching standards are unavailable.

The glow discharge in commercially available GDMS systems is operated with d.c. power. This implies that cathodes must be made of conducting materials, which requires special sample preparation techniques for the analysis of non-conducting samples. The two most common cathode geometries employed in GDMS are the pin cathode and the planar cathode. The pin cathode geometry is used with samples that are easily formed into cylindrical pins 1–2 mm in diameter and 7–10 mm in length; these can include powder samples compacted in a die press and bulk samples processed into the appropriate shape. If the sample is non-conducting, it is compacted with a conducting host material, such as tantalum, in order to avoid electrode charging in the d.c. plasma. The planar cathode

geometry is typically used for analysis of refractory materials and flat, non-conducting bulk samples. In the latter case, use is made of a metallic secondary cathode¹⁴⁸ in order to sustain the plasma discharge. Sputtering of the secondary cathode results in deposition of a conducting layer of material on the adjacent surface of the non-conducting sample, which is then, in turn, also sputtered. Introduction of samples in both pin and planar cathode geometries to the glow discharge chamber is achieved by means of a direct insertion probe.

GDMS is a well-developed mass-spectrometric technique for the analysis of trace elements in bulk solid samples. It offers several advantages over other trace analysis techniques (e.g. SSMS and SIMS), including detection limits down to the sub-ppb range, wide dynamic range ($\sim 10^{11}$ range between minor and major components), relative matrix insensitivity, and applicability to a wide variety of materials systems. Given these advantages, it was selected for elemental characterization of AlN solid (powder and bulk) samples in this study.

6.2 Synchrotron white beam x-ray topography (SWBXT) and high resolution x-ray diffraction (HRXRD)

X-ray diffraction is among the most common characterization methods for non-destructive evaluation of epitaxial thin films and bulk single crystals. A number of x-ray scattering techniques have been developed that yield information on chemical composition, lattice perfection, layer thickness and roughness, orientation, strain state, and grain size. A brief overview of SWBXT and HRXRD is provided.

6.2.1 SWBXT

X-ray diffraction topography is used to study the topography of a crystal's internal diffracting planes in order to discern local changes in the spacing and relative rotation of the planes,¹⁴⁹ X-ray topographs, two-dimensional projections of the distribution of diffracted intensity as a function of position in the sample, can be used to map defect structures in large, nearly perfect single crystals and to identify the crystallographic orientations of the diffracting planes. Images are produced by scattering a low divergence area-filling beam from a set of Bragg planes onto a two-dimensional detector, typically high-resolution x-ray film.

Several different mechanisms, which can be used to obtain information about the character of specific defects, contribute to contrast formation in topographs. Orientation contrast refers to differences in intensity arising from x-rays scattered along different directions, which correspond to scattering from regions of differing orientation within the crystal. In this way distortions due to adjacent mosaic blocks are imaged. Extinction contrast, on the other hand, is sensitive to local variations in crystal perfection. Primary extinction is

an effect encountered in highly perfect crystals which is due to interference between the incident and diffracted waves within the crystal. It leads to a decrease in the diffracted intensity from a perfect crystal versus a mosaic crystal. The diffracted intensity increases with the degree of imperfection up to the limit of the “ideally imperfect” crystal,¹⁵⁰ where no primary extinction is observed. In a crystal containing highly perfect regions interspersed with distorted regions surrounding defects (e.g. the strain field surrounding a dislocation), the distorted regions diffract more strongly and show up as dark regions in the topographic image (negative film). Intensity variations in the topographic image due to local variations in scattering direction (orientation contrast) or diffracted intensity (extinction contrast) appear as a function of position in the crystal; a one-to-one correspondence exists between defects in a topographic image and their location inside the crystal.¹⁵¹ By varying the diffraction conditions under which topographs are imaged, information about the character of these defects can be obtained. Typically, individual dislocations are observed in topographs once the crystal dislocation density drops below 10^6 cm^{-2} .

The earliest x-ray topography techniques made use of the $K_{\alpha 1}$ characteristic line from conventional x-ray sources. These sources typically require long exposure times for analysis of macroscopic crystals, partly due to the collimation of the incident beam required to separate the $K_{\alpha 1}$ - $K_{\alpha 2}$ doublet, and partly due to the need to translate larger crystals before the beam. More recently, synchrotron sources of radiation have offered several advantages over conventional x-ray sources, including high intensity, tunability, and inherent low divergence. One of the most important synchrotron topography techniques is SWBXT, which makes use of a polychromatic, or white, beam of synchrotron radiation. The range of wavelengths

present in the white beam allows multiple reflections to be recorded simultaneously, aiding in the identification of defect character from a smaller number of exposures than with conventional sources. Exposure time is reduced due to the high intensity of the synchrotron source. The large beam size allows imaging of large single crystals and the inherent collimation yields excellent geometrical resolution. Another advantage of the white beam lies in the ability to image crystals containing a range of orientations (e.g. bent crystals and mosaic crystals), or a range of lattice parameters (e.g. multiple phases or polytypes).¹⁵² The variations in lattice plane rotation and spacing are quantified through analysis of the topographic images.

6.2.2 HRXRD

Measurement of the diffraction peak widths of nearly perfect crystals or epitaxial films requires an instrumental setup where contributions to the peak widths from sources other than the sample itself are minimized. In the conventional single-axis θ - 2θ diffractometer, the x-ray beam emitted from the target contains two sources of broadening that contribute to the overall peak widths recorded with this instrument: (i) the beam contains a range of wavelengths, including the characteristic wavelengths of the target material and the continuous background radiation; and (ii) the beam itself is divergent, even when collimators are used.¹⁵³ This broadening, on the order of 0.1° , obscures much of the structural information from the sample, which in the case of high-quality single crystals implies widths of only a few arc seconds. Thus, in order to resolve these features the incident beam must be monochromated and collimated, which is achieved through multiple-crystal diffraction.

There are a number of multiple-crystal geometries used for conditioning of the incident beam which all rely on the same principle, namely diffraction of the incident beam from multiple high-quality reference crystals in order to monochromate and collimate the beam. A typical four-bounce multiple-crystal beam conditioner is able to provide arcsec resolution. In double axis diffractometry, the conditioned beam is directed at a sample crystal at an angle θ_B where Bragg diffraction occurs. The crystal is then rotated, or rocked, about θ_B and the diffracted beam is measured at a fixed detector with a large aperture. The measured distribution of intensity as a function of rocking angle $\Delta\theta$ constitutes a rocking curve, in this case a double crystal rocking curve; it represents the convolution of the monochromator and sample distributions.¹⁵⁴ The width of the rocking curve is a measure of two distinct kinds of information about the crystal's sampled volume: (i) the degree of misorientation or mosaicity of the crystal planes (i.e. lattice tilts); and (ii) the strain state or distribution of lattice d -spacings about the principal lattice parameter (i.e. lattice dilations). Due to the wide acceptance angle of the detector, however, the DCRC does not distinguish between these two contributions.

In order to separate these two contributions, the acceptance angle of the detector must be limited. This can be accomplished by placing a slit in front of the detector such that x-rays from only a single direction are measured. Thus, a coupled θ - 2θ scan collects information only from x-rays that have equal angles of incidence and reflection with respect to the Bragg planes, which correspond to lattice planes with the same orientation but slightly different d -spacings. In practice this restriction of the detector acceptance angle is accomplished by placing between the sample and the detector another reference crystal, whose action is

analogous to that of the incident beam conditioner described above. This geometry is termed triple axis diffractometry and the resulting rocking curves are triple crystal rocking curves (TCRCs).

The sample tilt distribution can be analyzed by recording a series of coupled θ - 2θ scans, each offset from the preceding scan by a small sample rotation α . For each subsequent sample rotation, if any diffracted intensity is detected it must come from misoriented planes. Thus a two-dimensional intensity distribution $I = I(\alpha, \Delta\theta)$ is generated from the entire scan process, where α is the sample offset angle and $\Delta\theta$ is the rocking angle of the individual TCRCs. It is customary to transform this intensity distribution to one describing the broadening of the associated reciprocal lattice points such that $I = I(\Delta q_x, \Delta q_z)$.¹⁵⁵ The intensity contours are then displayed in two-dimensional plots, or reciprocal space maps. These maps provide much more information than DCRCs, since the range of lattice tilts (Δq_x) and lattice dilations (Δq_z) can be read independently.¹⁵⁶ Reciprocal space mapping is thus a powerful technique for obtaining a large amount of information about the degree of perfection of single crystals.

6.3 Piezoresponse force microscopy (PFM)

PFM is a scanning probe microscopy (SPM)-based technique in which a modulating voltage is applied to a conducting tip in mechanical contact with a piezoelectric sample.¹²⁵ It has been used to image domain structure in ferroelectric thin films¹⁵⁷ and lateral polarity heterostructures in GaN films¹⁵⁸ with nanometer scale spatial resolution. The magnitude and phase of the bias-induced tip deflection, which follows the piezoelectric motion of the sample surface, are used to determine the piezoelectric coefficient d_{33} of c-oriented samples, and to distinguish between regions of different polarity on the sample surface. The tip can be rastered over the surface to create two-dimensional images of the piezoresponse signal. Since the piezoresponse depends on the polarization direction, the sample will oscillate either in-phase or out-of-phase with the modulating voltage; regions of different polarity exhibit opposite contrast in a PFM phase image. In the wurtzite III-nitrides the spontaneous polarization points from the III-metal atom face to the N-face. Following the conventions of Rodriguez *et al.*,¹⁵⁹ we define a positive voltage when the tip is biased positively with respect to the sample back contact, and a positive sample displacement when the piezoelectric motion of the sample consists of an extension. It has been found in studies of patterned GaN lateral polarity heterostructures that the oscillation of the N-face polarity is out of phase with the modulating voltage. Also, associating brightness in the gray scale data display with the out of phase oscillation, N-face GaN appears brighter in the PFM phase image.¹⁵⁹ The conventions just described were used in the PFM data displayed in section 3.6.4 of this dissertation. Due to the capability to image regions of different polarity, PFM is well suited

to study IDs in the III-nitrides and can be used to confirm the trends observed in etching studies.

7 References

- ¹ R. Dalmau and Z. Sitar, in *Encyclopedia of Materials: Science and Technology Updates*, edited by K. H. J. Buschow, R. W. Cahn, M. C. Flemings, B. Ilschner, E. J. Kramer, S. Mahajan, and P. Veyssi re (Elsevier, Oxford, 2005).
- ² O. Ambacher, *J. Phys. D* **31**, 2653 (1998).
- ³ R. Gaska, C. Chen, J. Yang, E. Kuokstis, A. Khan, G. Tamulaitis, I. Yilmaz, M. S. Shur, J. C. Rojo, and L. J. Schowalter, *Appl. Phys. Lett.* **81**, 4658 (2002).
- ⁴ B. Monemar, *J. Mat. Sci.* **10**, 227 (1999).
- ⁵ S. Nakamura, M. Senoh, S. Nagahama, N. Iwasa, T. Yamada, T. Matsushita, H. Kiyuku, Y. Sugimoto, T. Kuzaki, H. Umemoto, and K. Chocho, *Appl. Phys. Lett.* **72**, 2014 (1998).
- ⁶ J. C. Rojo, G. A. Slack, K. Morgan B. Raghothamachar, M. Dudley, and L. J. Schowalter, *J. Cryst. Growth* **231**, 317 (2001).
- ⁷ J. H. Edgar, L. Liu, B. Liu, D. Zhuang, J. Chaudhuri, M. Kuball, and S. Rajasingam, *J. Cryst. Growth* **246**, 187 (2002).
- ⁸ M. Bickermann, B. Epelbaum, and A. Winnacker, *Phys. Stat. Sol. (c)* **0**, 1993 (2003).
- ⁹ K. M. Taylor and C. Lenie, *J. Electrochem. Soc.* **107**, 308 (1960).
- ¹⁰ R. Schlessler and Z. Sitar, *J. Cryst. Growth* **234**, 349 (2002).
- ¹¹ C. O. Dugger, *Mater. Res. Bull.* **9**, 331 (1974).
- ¹² M. Bockowski, *Cryst. Res. Technol.* **36**, 771 (2001).
- ¹³ M Albrecht, I. P. Nikitina, A. E. Nikolaev, Y. V. Melnik, V. A. Dimitriev, and H. P. Strunk, *Phys. Stat. Sol. (a)* **176**, 453 (1999).

- ¹⁴ A. Nikolaev, I. Nikitina, A. Zubrilov, M. Mynbaeva, Y. Melnik, and V. Dimitriev, *MRS Internet J. Nitride Semicond Res.* **5S1**, W6.5 (2000).
- ¹⁵ R. Dwilinski, R. Doradzinski, J. Garczynski, L. Sierputowski, M. Palczewska, A. Wysmolek, and M. Kaminska, *MRS Internet J. Nitride Semicond. Res.* **3**, 25 (1998).
- ¹⁶ G. A. Slack and T. F. McNelly, *J. Cryst. Growth* **34**, 263 (1976).
- ¹⁷ M. Bickermann, B. M. Epelbaum, and A. Winnacker, *J. Cryst. Growth* **269**, 432 (2004).
- ¹⁸ F. Briegleb and A. Geuther, *Ann. Chem.* **123**, 228 (1862).
- ¹⁹ L. Ahrons, *Naturwiss. Rundschau* **14**, 453 (1899).
- ²⁰ A. Rabenau, in *Compound Semiconductors*, edited by R. K. Willardson and H. L. Goering (Reinhold, New York, 1962), Vol. **1**, p.174.
- ²¹ H. Funk and H. Boehland, *Z. Anorg. Allgem. Chem.* **334**, 155 (1964).
- ²² F. Fichter and G. Oesterheld, *Z. Electrochem.* **21**, 50 (1915).
- ²³ P. E. Evans and T. J. Davies, *Nature* **197**, 587 (1963).
- ²⁴ C. M. Drum and J. W. Mitchell, *Appl. Phys. Lett.* **4**, 164 (1964).
- ²⁵ T. J. Davies and P. E. Evans, *Nature* **207**, 254 (1965).
- ²⁶ G. A. Cox, D. O. Cummins, K. Kawabe, and R. H. Tredgold, *J. Phys. Chem. Solids* **28**, 543 (1967).
- ²⁷ S. Horiuchi, T. Ishii, and K. Asakurs, *J. Cryst. Growth* **21**, 17 (1974).
- ²⁸ H. D. Witzke, *Phys. Stat. Sol.* **2**, 1109 (1962).
- ²⁹ J. Pastrnak and L. Roskovcova, *Phys. Stat. Sol.* **7**, 331 (1964).
- ³⁰ C. M. Drum, *J. Appl. Phys.* **36**, 816 (1965).

- ³¹ A. T. Collins, E. C. Lightowers, and P. J. Dean, *Phys. Rev.* **158**, 833 (1967).
- ³² M. M. Faktor, R. Heckingbottom, and I. Garrett, *J. Chem. Soc. A* **1**, 2657 (1970).
- ³³ *CRC Handbook of Chemistry and Physics*, 74th edition, edited by D. R. Lide (CRC Press, Boca Raton, 1993), Chap. 5, p.5.
- ³⁴ S. Strite and H. Morkoç, *J. Vac. Sci. Technol. B* **10**, 1237 (1992).
- ³⁵ L. Liu and J. H. Edgar, *Mat. Sci. Eng. R* **37**, 61 (2002).
- ³⁶ P. Pirouz, *Mat. Sci. Forum* **264**, 399 (1998).
- ³⁷ A. D. Westwood and M. R. Notis, *J. Am. Ceram. Soc.* **74**, 1226 (1991).
- ³⁸ A. D. Westwood, R. A. Youngman, M. R. McCartney, A. N. Cormack, and M. R. Notis, *J. Mater. Res.* **10**, 1270 (1995).
- ³⁹ J. Jasinski, T. Tomaszewicz, Z. Liliental-Weber, Q. S. Paduano, and D. W. Weyburne, *Mater. Res. Soc. Symp. Proc.* **798**, Y5.29 (2004).
- ⁴⁰ J. Jasinski, Z. Liliental-Weber, Q. S. Paduano, and D. W. Weyburne, *Appl. Phys. Lett.* **83**, 2811 (2003).
- ⁴¹ J. L. Rouviere, J. L. Weyher, M. Seelmann-Eggebert, and S. Porowski, *Appl. Phys. Lett.* **73**, 668 (1998).
- ⁴² J. L. Weyher, P. D. Brown, J. L. Rouviere, T. Wosinski, A. R. A. Zaurer, and I. Grzegory, *J. Cryst. Growth* **210**, 151 (2000).
- ⁴³ D. Zhuang, J. H. Edgar, L. Liu, B. Liu, and L. Walker, *MRS Int. J. Nitride Semicond. Res.* **7**, 4 (2002).

- ⁴⁴ D. Zhuang, J. H. Edgar, B. Strojek, J. Chaudhuri, and Z. Rek, *J. Cryst. Growth* **262**, 89 (2004).
- ⁴⁵ R. Dalmau, R. Schlessler, and Z. Sitar, *Phys Stat. Sol. (c)* **2**, 2036 (2005).
- ⁴⁶ D. Gerlich, S. L. Dole, and G. A. Slack, *J. Phys. Chem. Sol.* **47**, 437 (1986).
- ⁴⁷ C. Deger, E. Born, H. Angerer, O. Ambacher, M. Stutzmann, J. Hornsteiner, E. Riha, and G. Fischerauer, *Appl. Phys. Lett.* **72**, 2400 (1998).
- ⁴⁸ A. F. Wright, *J. Appl. Phys.* **82**, 2833 (1997).
- ⁴⁹ J. M. Wagner and F. Bechstedt, *Appl. Phys. Lett.* **77**, 346 (2000).
- ⁵⁰ R. R. Reeber and K. Wang, *MRS Internet J. Nitride Semicond. Res.* **6**, 3 (2001).
- ⁵¹ K. Wang and R. R. Reeber, *MRS Internet J. Nitride Semicond. Res.* **4S1**, G3.18 (1999).
- ⁵² J. Pastnak and L. Roskovcova, *Phys. Stat. Sol.* **26**, 591 (1968).
- ⁵³ W. M. Yim, E. J. Stofko, P. J. Zanzucchi, J. I. Pankove, M. Ettenberg, and S. L. Gilbert, *J. Appl. Phys.* **44**, 292 (1973).
- ⁵⁴ G. A. Slack and T. F. McNelly, *J. Cryst. Growth* **42**, 560 (1977).
- ⁵⁵ T. Wethkamp, K. Wilmers, C. Cobet, N. Esser, W. Richter, O. Ambacher, M. Stutzmann, and M. Cardona, *Phys. Rev. B* **59**, 1845 (1999).
- ⁵⁶ E. Silveira, J. A. Freitas, Jr., M. Kneissel, D. W. Treat, N. M. Johnson, G. A. Slack, and L. J. Schowalter, *Appl. Phys. Lett.* **84**, 3501 (2004).
- ⁵⁷ E. Kuokstis, J. Zhang, Q. Fareed, J. W. Yang, G. Simin, M. A. Khan, R. Gaska, M. Shur, C. Rojo, and L. Schowalter, *Appl. Phys. Lett.* **81**, 2755 (2002).

- ⁵⁸ G. A. Slack, L. J. Schowalter, D. Morelli, and J. A. Freitas, Jr., *J. Cryst. Growth* **246**, 287 (2002).
- ⁵⁹ M. Strassburg, J. Senawiratne, N. Dietz, U. Habo Beck, A. Hoffmann, V. Noveski, R. Dalmau, R. Schlessner, and Z. Sitar, *J. Appl. Phys.* **96**, 5870 (2004).
- ⁶⁰ J. Senawiratne, M. Strassburg, N. Dietz, U. Habo Beck, A. Hoffmann, V. Noveski, R. Dalmau, R. Schlessner, and Z. Sitar, *Phys. Stat. Sol. (c)* **7**, 2774 (2005).
- ⁶¹ I. Vurgaftman and J. R. Meyer, *J. Appl. Phys.* **94**, 3675 (2003).
- ⁶² M. Suzuki, T. Uenoyama, and A. Yanase, *Phys. Rev. B* **52**, 8132 (1995).
- ⁶³ J. M. Wagner and F. Bechstedt, *Phys. Rev. B* **66**, 115202 (2002).
- ⁶⁴ J. Li, K. B. Nam, L. Nakarmi, J. Y. Lin, H. X. Jiang, P. Carrier, and S. H. Wei, *Appl. Phys. Lett.* **83**, 5163 (2003).
- ⁶⁵ L. Chen, B. J. Skromme, R. F. Dalmau, R. Schlessner, Z. Sitar, C. Chen, W. Sun, J. Yang, M. A. Khan, M. L. Nakarmi, J. Y. Lin, and H. X. Jiang, *Appl. Phys. Lett.* **85**, 4334 (2004).
- ⁶⁶ E. Silveira, J. A. Freitas, Jr., O. J. Glembocki, G. A. Slack, and L. J. Schowalter, *Phys. Rev. B* **71**, 41201 (2005).
- ⁶⁷ W. M. Yim and R. J. Paff, *J. Appl. Phys.* **45**, 1456 (1974).
- ⁶⁸ G. A. Slack, *J. Appl. Phys.* **46**, 89 (1975).
- ⁶⁹ R. R. Reeber and K. Wang, *Mat. Res. Soc. Symp. Proc.* **622**, T6.35 (2000).
- ⁷⁰ G. A. Slack, *J. Phys. Chem. Sol.* **34**, 321 (1973).
- ⁷¹ G. A. Slack, Air Force Office of Scientific Research, Final Report, Contract No. F49620-78-C-0021 (1980).

- ⁷² G. A. Slack, R. A. Tanzilli, R. O. Pohl, and J. W. Vandersande, *J. Phys. Chem. Sol.* **48**, 641 (1987).
- ⁷³ G. A. Slack, L. J. Schowalter, D. Morelli, and J. A. Freitas, Jr., *J. Cryst. Growth* **246**, 287 (2002).
- ⁷⁴ J. C. Rojo, L. J. Schowalter, K. Morgan, D. I. Florescu, F. H. Pollack, B. Raghoeamachar, and M. Dudley, *Mat. Res. Soc. Symp. Proc.* **680**, E2.1 (2001).
- ⁷⁵ G. A. Slack and S. F. Bartram, *J. Appl. Phys* **46**, 89 (1975).
- ⁷⁶ I. Grzegory, J. Jun, M. Bockowski, S. Krukowski, M. Wroblewski, B. Lucznik, and S. Porowski, *J. Phys. Chem. Solids* **56**, 639 (1995).
- ⁷⁷ L. Liu and J. H. Edgar, *J. Cryst. Growth* **220**, 243 (2000).
- ⁷⁸ V. Noveski, R. Schlessler, S. Mahajan, S. Beaudoin, and Z. Sitar, *J. Cryst. Growth* **264**, 369 (2004).
- ⁷⁹ W. K. Burton and N. Cabrera, *Discuss. Faraday Soc.* **5**, 33, 40 (1949).
- ⁸⁰ F. C. Frank, *Discuss. Faraday Soc.* **5**, 48 (1949).
- ⁸¹ W. K. Burton, N. Cabrera, and F. C. Frank, *Phil. Trans. Roy. Soc. Ser. A* **243**, 299 (1951).
- ⁸² R. Ghez and S. S. Iyer, *IBM J. Res. Develop.* **32**, 804 (1988).
- ⁸³ J. A. Lely, *Berichte der Deutschen Keramischen Gesellschaft* **32**, 229 (1955).
- ⁸⁴ Yu. M. Tairov and V. F. Tsvetkov, *J. Cryst. Growth* **43**, 209 (1978).
- ⁸⁵ X. Hu, J. Deng, N. Pala, R. Gaska, M. S. Shur, C. Q. Chen, J. Yang, G. Simin, M. A. Khan, J. C. Rojo, and L. J. Schowalter, *Appl. Phys. Lett.* **82**, 1299 (2003).
- ⁸⁶ T. Nishida, T. Makimoto, H. Saito, and T. Ban, *Appl. Phys. Lett.* **84**, 1002 (2004).

- ⁸⁷ M. V. Bogdanov, S. Yu. Karpov, A. V. Kulick, M. S. Ramm, Yu. N. Makarov, R. Schlessler, R. F. Dalmau, and Z. Sitar, *Mater. Res. Soc. Symp. Proc.* **743**, L.3.33 (2003).
- ⁸⁸ L. H. Dreger, V. V. Dadape, and J. L. Margrave, *J. Phys. Chem.* **66**, 1556 (1962).
- ⁸⁹ M. W. Chase, *NIST-JANAF Thermochemical Tables*, *J. Phys. Chem. Ref. Data*, Monograph No. 9 (American Institute of Physics, 1998).
- ⁹⁰ P. M. Dryburgh, *J. Cryst. Growth* **125**, 65 (1992).
- ⁹¹ M. Hoch and D. Ramakrishnan, *J. Electrochem. Soc.* **118**, 1204 (1971).
- ⁹² L. Liu and J. H. Edgar, *J. Cryst. Growth* **220**, 243 (2000).
- ⁹³ A. S. Segal, S. Yu. Karpov, Yu. N. Makarov, E. N. Mokhov, A. D. Roenkov, M. G. Ramm, and Yu. A. Vodakov, *J. Cryst. Growth* **211**, 68 (2000).
- ⁹⁴ S. Yu. Karpov, D. V. Zimina, Yu. N. Makarov, E. N. Mokhov, A. D. Roenkov, M. G. Ramm, and Yu. A. Vodakov, *Phys. Stat. Sol. (a)* **176**, 435 (1999).
- ⁹⁵ M. V. Averyanova, S. Yu. Karpov, Yu. N. Makarov, I. N. Przhevalskii, M. S. Ramm, and R. A. Talalev, *MRS Internet J. Nitride Semicond. Res.* **1**, 31 (1996).
- ⁹⁶ A. G. Gaydon, *Dissociation Energies and Spectra of Diatomic Molecules* (Chapman and Hall, London, 1968), p.194.
- ⁹⁷ J. E. Mahan, *Physical Vapor Deposition of Thin Films* (John Wiley & Sons, New York, 2000), Chap. 3, p.64.
- ⁹⁸ P. O. Schissel and W. S. Williams, *Bull. Am. Phys. Soc.* **4**, 139 (1959).
- ⁹⁹ G. Meloni and K. A. Gingerich, *J. Chem. Phys.* **113**, 10978 (2000).
- ¹⁰⁰ B. D. Leskiw and J. A. W. Castleman, *J. Chem. Phys.* **114**, 1165 (2001).

- ¹⁰¹ Y. Li and D. W. Brenner, Phys. Rev. Lett. **92**, 75503 (2004).
- ¹⁰² R. Schlessler, R. Dalmau, D. Zhuang, R. Collazo, and Z. Sitar, J. Cryst. Growth **281**, 75 (2005).
- ¹⁰³ Y. Shi, Z. Y. Xie, L. H. Liu, B. Liu, J. H. Edgar, and M. Kuball, J. Cryst. Growth **233**, 177 (2001).
- ¹⁰⁴ B. M. Epelbaum, D. Hoffman, M. Bickermann, and A. Winnacker, Mater. Sci. Forum **389-393**, 1445 (2002).
- ¹⁰⁵ M. Tanaka, S. Nakahata, K. Sogabe, H. Nakata, and M. Tobioka, Jap. J. Appl. Phys. **36**, L1062 (1997).
- ¹⁰⁶ C. M. Balkas, Z. Sitar, T. Zheleva, L. Bergman, R. Nemanich, and R. F. Davis, J. Cryst. Growth **179**, 363 (1991).
- ¹⁰⁷ R. Dalmau, B. Raghothamachar, M. Dudley, R. Schlessler, and Z. Sitar, Mater. Res. Soc. Symp. Proc. **798**, Y2.9 (2004).
- ¹⁰⁸ G. A. Slack, J. Whitlock, K. Morgan, and L. J. Schowalter, Mater. Res. Soc. Symp. Proc. **798**, 10.74 (2004).
- ¹⁰⁹ H. O. Pierson, *Handbook of Refractory Carbides and Nitrides* (Noyes Publications, Park Ridge, NJ, 1996), Chap. 2, p.14.
- ¹¹⁰ Y. Baik and R. A. L. Drew, Key Engr. Mat. **122-124**, 553 (1996).
- ¹¹¹ M. Medraj, Y. Baik, W. T. Thompson, and R. A. L. Drew, J. Mat. Processing Technol. **161**, 415 (2004).
- ¹¹² C. E. Draper, M.S. thesis, Dept. Mat. Sci. Eng., North Carolina State Univ. (2000).

- ¹¹³ B. Raghothamachar, W. M. Vetter, M. Dudley, R. Dalmau, R. Schlessner, Z. Sitar, E. Michaels, and J. W. Kolis, *J. Cryst. Growth* **246**, 271 (2002).
- ¹¹⁴ B. Liu, J. H. Edgar, Z. Gu, D. Zhuang, B. Raghothamachar, M. Dudley, A. Sarua, M. Kuball, and H. M. Meyer III, *MRS Internet J. Nitride Semicond. Res.* **9**, 6 (2004).
- ¹¹⁵ D. W. Brenner, R. Schlessner, Z. Sitar, R. Dalmau, R. Collazo, and Y. Li, *Surface Science* **560**, L202 (2004).
- ¹¹⁶ K. Kim and W. R. L. Lambrecht, *Phys. Rev. B* **56**, 7363 (1997).
- ¹¹⁷ B. Raghothamachar, M. Dudley, K. Morgan, and L. J. Schowalter, *J. Cryst. Growth* **250**, 244 (2003).
- ¹¹⁸ R. Schlessner, R. Dalmau, and Z. Sitar, *J. Cryst. Growth* **241**, 416 (2002).
- ¹¹⁹ Y. Shi, B. Liu, J. H. Edgar, E. A. Payzant, J. M. Hayes, and M. Kuball, *MRS Internet J. Nitride Semicond. Res.* **6**, 5 (2001).
- ¹²⁰ B. M. Epelbaum, M. Bickermann, and A. Winnacker, *Mater. Sci. Forum* **433-436**, 983 (2003).
- ¹²¹ L. Liu, Y. Shi, and J. H. Edgar, *MRS Internet J. Nitride Semicond. Res.* **6**, 7 (2001).
- ¹²² L. Liu, D. Zhuang, B. Liu, Y. Shi, J. H. Edgar, S. Rajasingam, and M. Kuball, *Phys. Stat. Sol. (a)* **188**, 769 (2001).
- ¹²³ S. Tanaka, R. S. Kern, and R. F. Davis, *Appl. Phys. Lett.* **66**, 37 (1994).
- ¹²⁴ X. R. Huang, M. Dudley, W. M. Vetter, W. Huang, S. Wang, and C. H. Carter, Jr., *Appl. Phys. Lett.* **74**, 353 (1999).

- ¹²⁵ R. Dalmau, R. Schlessner, B. J. Rodriguez, R. J. Nemanich, and Z. Sitar, *J. Cryst. Growth* **281**, 68 (2005).
- ¹²⁶ J. Brault, E. Bellet-Amalric, S. Tanaka, F. Enjalbert, D. Le Si Dang, E. Sarigiannidou, J. L. Rouviere, G. Feuillet, and B. Daudin, *Physica Status Solidi (b)* **240**, 314 (2003).
- ¹²⁷ B. Raghothamachar, M. Dudley, R. Dalmau, R. Schlessner, and Z. Sitar, *Mater. Res. Soc. Symp. Proc.* **831**, E8.24 (2005).
- ¹²⁸ X. R. Huang, J. Bai, M. Dudley, R. D. Dupuis, and U. Chowdhury, *Appl. Phys. Lett.* **86**, 211916 (2005).
- ¹²⁹ H. Nagai, *J. Appl. Phys.* **45**, 3789 (1974).
- ¹³⁰ G. H. Olsen and M. Ettenberg, *J. Appl. Phys.* **48**, 2543 (1977).
- ¹³¹ P. H. Townsend, D. M. Barnett, and T. A. Brunner, *J. Appl. Phys.* **62**, 4438 (1987).
- ¹³² G. G. Stoney, *Proc. Roy. Soc. Ser. A* **82**, 172 (1909).
- ¹³³ S. Timoshenko, *J. Opt. Soc. Am.* **11**, 23 (1925).
- ¹³⁴ R. W. Hoffman, *Phys. Thin Films* **3**, 211 (1966).
- ¹³⁵ R. H. Saul, *J. Appl. Phys.* **40**, 3273 (1969).
- ¹³⁶ L. Liu, B. Liu, J. H. Edgar, S. Rajasingam, and M. Kuball, *J. Appl. Phys.* **92**, 5183 (2002).
- ¹³⁷ K. Hiramatsu, T. Detchprohm, and I. Akasaki, *Jpn. J. Appl. Phys.* **32**, 1528 (1993).
- ¹³⁸ R. R. Reeber and K. Wang, *MRS Internet J. Nitride Semicond. Res.* **6**, 3 (2001).
- ¹³⁹ A. A. Griffiths, *Phil. Trans. Roy. Soc. Ser. A* **221**, 163 (1920).
- ¹⁴⁰ M. D. Thouless, *Ann. Rev. Mater. Sci.* **25**, 69 (1995).

- ¹⁴¹ P. D. Brown, J. L. Weyher, C. B. Boothroyd, D. T. Foord, A. R. A. Zauner, P. R. Hageman, P. K. Larsen, M. Bockowski, and C. J. Humphreys, *Inst. Phys. Conf. Ser.* **164**, 381 (1999).
- ¹⁴² R. Collazo, S. Mita, R. Schlessler, and Z. Sitar, *Phys. Stat. Sol. (c)* **2**, 2117 (2005).
- ¹⁴³ M. Sumiya and S. Fuke, *MRS Internet J. Nitride Semicond. Res.* **9**, 1 (2004).
- ¹⁴⁴ F. L. King, J. Teng, and R. E. Steiner, *J. Mass Spectrometry* **30**, 1061 (1995).
- ¹⁴⁵ D. L. Smith, *Thin Film Deposition: Principles and Practice* (McGraw-Hill, Boston, 1995), Chap. 9, p.454.
- ¹⁴⁶ R. K. Marcus and J. A. C. Broekaert, in *Glow Discharge Plasmas in Analytical Spectroscopy*, edited by R. K. Marcus and J. A. C. Broekaert (John Wiley & Sons, New York, 2003), Chap. 1, p.6.
- ¹⁴⁷ M. Ohring, *Materials Science of Thin Films: Deposition and Structure*, 2nd edition (Academic Press, San Diego, 2002), Chap. 4, p.181.
- ¹⁴⁸ A. Bogaerts and R. Gijbels, *Fresenius J. Anal. Chem.* **364**, 367 (1999).
- ¹⁴⁹ M. Dudley and X. Huang, in *Encyclopedia of Materials: Science and Technology*, edited by K. H. J. Buschow, R. W. Cahn, M. C. Flemings, B. Ilschner, E. J. Kramer, and S. Mahajan (Pergamon Press, Oxford, 2001), p.9813.
- ¹⁵⁰ J. E. White, *J. Appl. Phys.* **21**, 855 (1950).
- ¹⁵¹ B. D. Cullity and S. R. Stock, *Elements of X-Ray Diffraction*, 3rd edition (Prentice Hall, New Jersey, 2001), Chap. 17, p.511.

- ¹⁵² M. Dudley and X. Huang, in *Encyclopedia of Materials: Science and Technology*, edited by K. H. J. Buschow, R. W. Cahn, M. C. Flemings, B. Ilschner, E. J. Kramer, and S. Mahajan (Pergamon Press, Oxford, 2001), p.9816.
- ¹⁵³ M. Dudley and X. R. Huang, in *Encyclopedia of Materials: Science and Technology*, edited by K. H. J. Buschow, R. W. Cahn, M. C. Flemings, B. Ilschner, E. J. Kramer, and S. Mahajan (Pergamon Press, Oxford, 2001), p.2777.
- ¹⁵⁴ B. D. Cullity and S. R. Stock, *Elements of X-Ray Diffraction*, 3rd edition (Prentice Hall, New Jersey, 2001), Chap. 17, p.527.
- ¹⁵⁵ M. Dudley and X. R. Huang, in *Encyclopedia of Materials: Science and Technology*, edited by K. H. J. Buschow, R. W. Cahn, M. C. Flemings, B. Ilschner, E. J. Kramer, and S. Mahajan (Pergamon Press, Oxford, 2001), p.2783.
- ¹⁵⁶ M. S. Goorsky, K. M. Matney, M. Meshkinpour, D. C. Streit, and T. R. Block, *Il Nuovo Cimento* **19**, 257 (1997).
- ¹⁵⁷ S. V. Kalinin and D. A. Bonnell, *Phys. Rev. B* **65**, 125408 (2002).
- ¹⁵⁸ B. J. Rodriguez, A. Gruverman, A. I. Kingon, and R. J. Nemanich, *Appl. Phys. Lett.* **80**, 4166 (2002).
- ¹⁵⁹ B. J. Rodriguez, A. Gruverman, A. I. Kingon, and R. J. Nemanich, *J. Cryst. Growth* **246**, 252 (2002).